NUREG/CR-4667, Vol. 25
ANL-98/18

Environmentally Assisted Cracking in Light-Water Reactors

Semiannual Report
July 1997 - December 1997

Prepared by
O. K. Chopra, H. M. Chung, E. E. Gruber,
T. F. Kassner, W. E. Ruther, W. J. Shack,
J. L. Smith, W. K. Soppet, R.V. Strain

Argonne National Laboratory

Prepared for
U.S. Nuclear Regulatory Commission

AVAILABILITY NOTICE

Availability of Reference Materials Cited in NRC Publications

NRC publications in the NUREG series, NRC regulations, and *Title 10, Energy,* of the *Code of Federal Regulations,* may be purchased from one of the following sources:

1. The Superintendent of Documents
   U.S. Government Printing Office
   P.O. Box 37082
   Washington, DC 20402–9328
   <http://www.access.gpo.gov/su_docs>
   202–512–1800

2. The National Technical Information Service
   Springfield, VA 22161–0002
   <http://www.ntis.gov/ordernow>
   703–487–4650

The NUREG series comprises (1) technical and administrative reports, including those prepared for international agreements, (2) brochures, (3) proceedings of conferences and workshops, (4) adjudications and other issuances of the Commission and Atomic Safety and Licensing Boards, and (5) books.

A single copy of each NRC draft report is available free, to the extent of supply, upon written request as follows:

Address: Office of the Chief Information Officer
Reproduction and Distribution
Services Section
U.S. Nuclear Regulatory Commission
Washington, DC 20555–0001
E–mail: <GRW1@NRC.GOV>
Facsimile: 301–415–2289

A portion of NRC regulatory and technical information is available at NRC's World Wide Web site:

<http://www.nrc.gov>

All NRC documents released to the public are available for inspection or copying for a fee, in paper, microfiche, or, in some cases, diskette, from the Public Document Room (PDR):

NRC Public Document Room
2121 L Street, N.W., Lower Level
Washington, DC 20555–0001
<http://www.nrc.gov/NRC/PDR/pdr1.htm>
1–800–397–4209 or locally 202–634–3273

Microfiche of most NRC documents made publicly available since January 1981 may be found in the Local Public Document Rooms (LPDRs) located in the vicinity of nuclear power plants. The locations of the LPDRs may be obtained from the PDR (see previous paragraph) or through:

<http://www.nrc.gov/NRC/NUREGS/SR1350/V9/lpdr/html>

Publicly released documents include, to name a few, NUREG-series reports; *Federal Register* notices; applicant, licensee, and vendor documents and correspondence; NRC correspondence and internal memoranda; bulletins and information notices; inspection and investigation reports; licensee event reports; and Commission papers and their attachments.

Documents available from public and special technical libraries include all open literature items, such as books, journal articles, and transactions, *Federal Register* notices, Federal and State legislation, and congressional reports. Such documents as theses, dissertations, foreign reports and translations, and non-NRC conference proceedings may be purchased from their sponsoring organization.

Copies of industry codes and standards used in a substantive manner in the NRC regulatory process are maintained at the NRC Library, Two White Flint North, 11545 Rockville Pike, Rockville, MD 20852–2738. These standards are available in the library for reference use by the public. Codes and standards are usually copyrighted and may be purchased from the originating organization or, if they are American National Standards, from—

American National Standards Institute
11 West 42nd Street
New York, NY 10036–8002
<http://www.ansi.org>
212–642–4900

NUREG/CR-4667, Vol. 25
ANL-98/18

Environmentally Assisted Cracking in Light-Water Reactors

Semiannual Report
July 1997 - December 1997

Manuscript Completed: August 1998
Date Published: September 1998

Prepared by
O. K. Chopra, H. M. Chung, E. E. Gruber,
T. F. Kassner, W. E. Ruther, W. J. Shack,
J. L. Smith, W. K. Soppet, R.V. Strain

Argonne National Laboratory
9700 South Cass Avenue
Argonne, IL 60439

M. B. McNeil, NRC Project Manager

Prepared for
Division of Engineering Technology
Office of Nuclear Regulatory Research
U.S. Nuclear Regulatory Commission
Washington, DC 20555-0001
NRC Job Code W6610

Previous Documents in Series

Environmentally Assisted Cracking in Light Water Reactors Semiannual Report April—September 1985, NUREG/CR-4667 Vol. I, ANL-86-31 (June 1986).

Environmentally Assisted Cracking in Light Water Reactors Semiannual Report October 1985—March 1986, NUREG/CR-4667 Vol. II, ANL-86-37 (September 1987).

Environmentally Assisted Cracking in Light Water Reactors Semiannual Report April—September 1986, NUREG/CR-4667 Vol. III, ANL-87-37 (September 1987).

Environmentally Assisted Cracking in Light Water Reactors Semiannual Report October 1986—March 1987, NUREG/CR-4667 Vol. IV, ANL-87-41 (December 1987).

Environmentally Assisted Cracking in Light Water Reactors Semiannual Report April—September 1987, NUREG/CR-4667 Vol. V, ANL-88-32 (June 1988).

Environmentally Assisted Cracking in Light Water Reactors Semiannual Report October 1987—March 1988, NUREG/CR-4667 Vol. 6, ANL-89/10 (August 1989).

Environmentally Assisted Cracking in Light Water Reactors Semiannual Report April—September 1988, NUREG/CR-4667 Vol. 7, ANL-89/40 (March 1990).

Environmentally Assisted Cracking in Light Water Reactors Semiannual Report October 1988—March 1989, NUREG/CR-4667 Vol. 8, ANL-90/4 (June 1990).

Environmentally Assisted Cracking in Light Water Reactors Semiannual Report April—September 1989, NUREG/CR-4667 Vol. 9, ANL-90/48 (March 1991).

Environmentally Assisted Cracking in Light Water Reactors Semiannual Report October 1989—March 1990, NUREG/CR-4667 Vol. 10, ANL-91/5 (March 1991).

Environmentally Assisted Cracking in Light Water Reactors Semiannual Report April—September 1990, NUREG/CR-4667 Vol. 11, ANL-91/9 (May 1991).

Environmentally Assisted Cracking in Light Water Reactors Semiannual Report October 1990—March 1991, NUREG/CR-4667 Vol. 12, ANL-91/24 (August 1991).

Environmentally Assisted Cracking in Light Water Reactors Semiannual Report April—September 1991, NUREG/CR-4667 Vol. 13, ANL-92/6 (March 1992).

Environmentally Assisted Cracking in Light Water Reactors Semiannual Report October 1991—March 1992, NUREG/CR-4667 Vol. 14, ANL-92/30 (August 1992).

Environmentally Assisted Cracking in Light Water Reactors Semiannual Report April—September 1992, NUREG/CR-4667 Vol. 15, ANL-93/2 (June 1993).

Environmentally Assisted Cracking in Light Water Reactors Semiannual Report October 1992—March 1993, NUREG/CR-4667 Vol. 16, ANL-93/27 (September 1993).

Environmentally Assisted Cracking in Light Water Reactors Semiannual Report April—September 1993, NUREG/CR-4667 Vol. 17, ANL-94/26 (June 1994).

Environmentally Assisted Cracking in Light Water Reactors Semiannual Report October 1993—March 1994, NUREG/CR-4667 Vol. 18, ANL-95/2 (March 1995).

Environmentally Assisted Cracking in Light Water Reactors Semiannual Report April—September 1994, NUREG/CR-4667 Vol. 19, ANL-95/25 (September 1995).

Environmentally Assisted Cracking in Light Water Reactors Semiannual Report October 1994—March 1995, NUREG/CR-4667 Vol. 20, ANL-95/41 (January 1996).

Environmentally Assisted Cracking in Light Water Reactors Semiannual Report April—December 1995, NUREG/CR-4667 Vol. 21, ANL-96/1 (July 1996).

Environmentally Assisted Cracking in Light Water Reactors Semiannual Report January 1996—June 1996, NUREG/CR-4667 Vol. 22, ANL-97/9 (June 1997).

Environmentally Assisted Cracking in Light Water Reactors Semiannual Report July 1996—December 1996, NUREG/CR-4667 Vol. 23, ANL-97/10 (October 1997).

Environmentally Assisted Cracking in Light Water Reactors Semiannual Report January 1997—June 1997, NUREG/CR-4667 Vol. 24, ANL-98/6 (April 1998).

Environmentally Assisted Cracking in Light Water Reactors Semiannual Report July 1997–December 1997

by

O. K. Chopra, H. M. Chung, E. E. Gruber, T. F. Kassner,
W. E. Ruther, W. J. Shack, J. L. Smith, W. K. Soppet, and R. V. Strain

Abstract

This report summarizes work performed by Argonne National Laboratory on fatigue and environmentally assisted cracking (EAC) in light water reactors from July 1997 to December 1997. Topics that have been investigated include (a) fatigue of austenitic stainless steels (SSs), (b) irradiation-assisted stress corrosion cracking of austenitic SSs, and (c) EAC of Alloys 600 and 690. Fatigue tests were conducted on austenitic SSs in water that contained various concentrations of dissolved oxygen to determine whether a slow strain rate applied during various portions of a tensile-loading cycle is equally effective in decreasing fatigue life. Slow-strain-rate-tensile tests were conducted in simulated boiling water reactor (BWR) water at 288°C on SS specimens irradiated to a low and medium fluence in the Halden reactor, and the results were compared with similar data from a control-blade sheath and neutron-absorber tubes irradiated in BWRs to the same fluence levels. Crack-growth-rate (CGR) tests were completed on compact-tension specimens from several heats of Alloys 600 and 690 in air, high-purity water, and simulated pressurized water reactor environments. CGR correlations were developed as a functon of loading and environmental parameters.

Contents

Figures

Tables

Executive Summary

Environmental Effects on Fatigue Strain-versus-Life (S–N) Behavior of Primary Pressure Boundary Materials

Cyclic loadings on a structural component occur because of changes in the mechanical and thermal loadings as the system goes from one load set (e.g., pressure, temperature, moment, and force loading) to any other load set. For each pair of load sets, an individual fatigue usage factor is determined by the ratio of the number of cycles anticipated during the lifetime of the component to the allowable cycles. Figures I-9.1 through I-9.6 of Appendix I to Section III of the ASME Boiler and Pressure Vessel Code specify fatigue design curves that define the allowable number of cycles as a function of applied stress amplitude. The cumulative usage factor (CUF) is the sum of the individual usage factors, and the ASME Code Section III requires that the CUF at each location must not exceed 1.

Subsection NB-3121 of Section III of the Code states that the data on which the fatigue design curves are based did not include tests in the presence of corrosive environments that might accelerate fatigue failure. Article B-2131 in Appendix B to Section III states that the owner's design specifications should provide information on any reduction to fatigue design curves necessitated by environmental conditions. Recent fatigue strain-versus-life (S–N) data illustrate potentially significant effects of light water reactor (LWR) coolant environments on the fatigue resistance of pressure vessel and piping steels. Under certain conditions of loading and environment, fatigue lives of carbon steels can be a factor of 70 lower in the environment than those in air. These results raise the issue of whether the fatigue design curves in Section III are appropriate for the purposes intended and whether they adequately account for environmental effects on fatigue behavior.

This report summarizes available data on the effects of various material and loading variables, on the fatigue lives of wrought and cast austenitic SSs. The existing fatigue S–N data for austenitic stainless steels in air and water environments have been evaluated to establish the effects of steel type, strain range, strain rate, temperature, and DO level in water, on the fatigue life of these steels. In air, the fatigue lives of austenitic SSs are independent of temperature in the range from room temperature to 450°C. The fatigue lives of Types 304 and 316 SS are comparable and those of Type 316NG SS are longer. The current ASME mean curve for life in air is not consistent with the existing fatigue S–N data. There is a significant decrease in fatigue life in water relative to that in air; the decrease in life depends on strain rate, DO level in water and temperature. Environmental effects on fatigue life are comparable for all of the alloys investigated. However, unlike carbon and low-alloy steels, environmental effects are more pronounced in low-DO than in high-DO water for austenitic SSs. The influence of reactor environments on fatigue crack initiation is discussed.

Statistical models that were developed earlier for estimating the fatigue lives of austenitic SSs in LWR environments have been updated with a larger data base. Design fatigue curves that can be used to perform ASME Code fatigue evaluations for components for service in LWR environments have been developed. The effects of LWR coolant environments on fatigue life have also been expressed in terms of a fatigue life correction factor defined as the ratio of the life in air to that in water.

Irradiation-Assisted Stress Corrosion Cracking

Slow-strain-rate-tensile (SSRT) tests were conducted on model stainless steel (SS) alloys that were irradiated at 288°C in helium in the Halden reactor. Tests in simulated BWR water at 288°C were completed for all 16 alloys that were irradiated to a fluence of ≈0.3 x 10^{21} n·cm^{-2} (E > 1 MeV) and 4 alloys irradiated to a fluence of ≈0.9 x 10^{21} n·cm^{-2} (E > 1 MeV). Fractographic analysis by scanning electron microscopy (SEM) also has been completed to determine susceptibilities to transgranular and intergranular stress corrosion cracking (TGSCC and IGSCC).

Heat-to-heat variations in susceptibilities to IGSCC and TGSCC were very significant, which suggests that heat-to-heat variations in crack growth rate could be also strong. High-purity (HP) heats of Type 316L SSs exhibited least ductility and highest susceptibility to IGSCC (i.e., highest percent of IGSCC on the fracture surface of the SSRT specimens), followed by HP Type 304L SS heat. This behavior is similar to that observed for BWR neutron-absorber tubes fabricated from HP heats of Type 304 SS. Type 304 SS containing a relatively high level of oxygen exhibited poor work-hardening capability and low ductility in water, even in the nonirradiated condition.

Susceptibility to IASCC of the 16 specimens irradiated to ≈0.3 x 10^{21} n·cm^{-2} (E > 1 MeV) was determined by SSRT tests in simulated BWR water containing ≈8 ppm DO at 288°C. Following the tests, fractographic analysis was conducted by SEM to determine the failure mode. Total elongation and susceptibility to TGSCC and IGSCC of the alloys could be correlated surprisingly well with nitrogen and silicon concentrations of the alloys. Irrespective of the carbon concentration and minor impurity contents, all 6 alloys that contain low levels of nitrogen (<50 wppm) and silicon (<1.0 wt.%) exhibit low ductility and high susceptibility to TGSCC, and in some heats, high susceptibility to IGSCC. All 10 alloys that contain either high silicon (>1.0 wt.%) or nitrogen (>50 wppm) exhibit high ductility and low percent TGSCC and negligible percent IGSCC. This observation suggests that >100 wppm nitrogen and >1.0 wt.% silicon could be effective in delaying the onset of IASCC to a higher threshold fluence.

Previous experience suggests that IASCC is characterized by high susceptibility to TGSCC at low fluence, followed by a transition from TGSCC to IGSCC as fluence increases. However, whether the same 10 alloys that contain >50 wppm nitrogen or >1.0 wt.% silicon will remain resistant to IASCC at higher fluences will be confirmed by further tests on our medium- and high-fluence specimens, i.e., specimens irradiated to ≈0.9 x 10^{21} and ≈2.8 x 10^{21} n·cm^{-2} (E > 1 MeV), respectively. Initial tests were conducted on 4 medium-fluence specimens and preliminary results, as expected, indicate that as fluence increases from ≈0.3 x 10^{21} to ≈0.9 x 10^{21} n cm^{-2} in the low-nitrogen and low-silicon alloys, susceptibility to TGSCC decreases, and at the same time, susceptibility to IGSCC increases at the expense of TGSCC. The preliminary results also indicate that alloys that contain <50 wppm nitrogen and <1.0 wt.% silicon are susceptible to IGSCC at ≈0.9 x 10^{21} n·cm^{-2} (E > 1 MeV). Tests on the remaining medium-fluence specimens are in progress.

Environmentally Assisted Cracking of Alloys 600 and 690 in Simulated LWR Water

Fracture-mechanics CGR tests were completed on compact-tension specimens of several heats of Alloys 600 and 690 in annealed and annealed and thermally treated conditions in high-purity water with DO levels between 1 and 7500 ppb and in low-DO water that contained

boron acid, lithium hydroxide, and low concentrations of dissolved hydrogen at 240, 289, and 320°C. Fracture-mechanics CGR tests were also conducted on compact-tension specimens of several specimens of these alloys in air at temperatures between 35 and 320°C. A data base of the CGR results has been compiled and CGR correlations were developed in terms of relevant loading and environmental parameters in the experiments. The statistical analysis of the results provides a means of predicting CGRs of the materials under cyclic loading conditions in simulated reactor coolant environments at specified confidence levels.

The degree of enhancement of the CGRs in aqueous environments relative to that in air is a function of both loading and environmental conditions (DO level). Crack growth rates for these alloys in high-purity water and simulated PWR water that contained low levels of DO (<5 ppb) were similar; i.e., the presence of boric acid, lithium hydroxide, and dissolved hydrogen in low-DO water have no discernible effect on the rates. Temperature and different heats and heat-treatment conditions have a relatively minor influence on the rates in air and aqueous environments for the materials and conditions in our investigation.

For a rise time of 12 s, crack growth rates of Alloys 600 and 690 are higher in water relative to those in air at ΔK values <6 MPa·m$^{1/2}$. At higher ΔK values, the CGRs in water are higher by a factor of ≈2 than in air. Dissolved oxygen concentration in water (≈1 and 300 ppb) has virtually no effect on the CGRs of a low-carbon heat of Alloy 600 although the rates in water are higher than in air by a factor of 6-8 at a low ΔK of ≈4 MPa·m$^{1/2}$. Crack growth rates of annealed Alloy 600 with ≈0.06% carbon are also higher in water than in air, but mainly in water with ≈300 ppb DO. In water that contains ≈1 ppb DO, the predicted CGRs at the 50 and 95% confidence levels for Alloy 600 with ≈0.02% carbon are higher than for material with a normal carbon content of ≈0.06% for ΔK values of <16 MPa·m$^{1/2}$. Crack growth rates for Alloy 690 in water are higher than in air by only a factor of ≈2 for both DO levels over the range of ΔK from ≈4 to 28 MPa·m$^{1/2}$. At the 95% confidence level, the rates for Alloy 690 are only somewhat lower than for Alloy 600 in low-DO water at ΔK values of <16 MPa·m$^{1/2}$.

The Alloy 600 and 690 specimens exhibited a predominantly transgranular mode of crack propagation because of the strong contribution of mechanical cyclic loading in tests at load ratios of <0.8 and the relatively small amount of crack propagation in tests for up to ≈1000 h at higher load ratios.

Acknowledgments

The authors thank W. F. Burke, T. M. Galvin, J. Tezak, and D. R. Perkins for their contributions to the experimental effort. This work is sponsored by the Office of Nuclear Regulatory Research, U.S. Nuclear Regulatory Commission, under Job Code W6610; Program Manager: Dr. M. B. McNeil.

1 Introduction

The U.S. Nuclear Regulatory Commission (NRC) and its predecessor, the U.S. Atomic Energy Commission, have conducted research programs that address aging of reactor components. The results of the research have been used to evaluate and establish regulatory guidelines to ensure acceptable levels of reliability for light water reactor (LWR) components. The products of this program have been technical reports, methodologies for evaluating licensee submittals, and other inputs to the regulatory process. The results have led to the resolution of regulatory issues, as well as the development, validation, and improvement of regulations and regulatory guides. The present research on the effects of simulated reactor coolant environments on cracking of reactor components was initiated to resolve remaining critical technical issues related to cracking phenomena in LWR components. Initially, this project addressed cracking of boiling water reactor (BWR) pipes. Subsequently, in response to the NRC Division of Nuclear Reactor Regulation (NRR) requests for assistance in dealing with developing cracking problems in aging reactors, the focus shifted to other problems in environmentally assisted cracking (EAC) of LWR components.

The overall objective of this program is to provide data and physical models to be used by the NRC staff in assessing environmentally assisted degradation of primary pressure boundary components in LWRs. The research is divided into five tasks:

(a) *Environmental effects on fatigue, crack growth, and stress corrosion cracking*
Fatigue and EAC of piping, pressure vessels, and core components in LWRs are important concerns in plant operation and for extended reactor lifetimes. The degradation processes in U.S. reactors include fatigue, intergranular stress corrosion cracking (IGSCC), and propagation of fatigue or stress corrosion cracks that initiate in the weld-sensitized heat-affected zone (HAZ) of stainless steel (SS) components. Occurrences of mechanical-vibration- and thermal-fluctuation-induced fatigue failures in LWR plants have also been documented. The objective of this task is to improve fatigue design curves and assess the additivity of fatigue damage in piping and vessel steels under load histories typical of LWR components. The results of this work will be used to assess industry fatigue evaluations related to license renewal.

(b) *Component vulnerability to irradiation-assisted stress corrosion cracking*
Irradiation-assisted stress corrosion cracking (IASCC) of in-core components of both BWRs and pressurized-water reactors (PWRs) is becoming a more common problem as reactors age. The general pattern of the observed failures indicates that as nuclear plants age and neutron fluence increases, many apparently nonsensitized austenitic materials become susceptible to intergranular failure by IASCC. Some of these failures have been reported for components subjected to relatively low or negligible stress levels, e.g., control-blade sheaths and handles and instrument dry tubes of BWRs. Although most failed components can be replaced, some safety-significant structural components, such as the BWR top guide, core plate, and shroud, would be very difficult or impractical to replace. The objective of this task is to provide data and models that are needed to assess industry analyses of the likelihood of degradation and failure of core internal components due to IASCC, and to evaluate licensee submissions concerning inspection and remediation.

(c) *Cracking of nickel alloy components of LWR primary systems*
Internal components of reactor vessels are made of nickel-base alloys, e.g., Alloys 600, X750, and 182, which are susceptible to IGSCC. The causes and mechanisms of this cracking are not adequately understood and increase the uncertainty when licensee submissions are evaluated for factors such as damage accumulation and inspection intervals. The objective of this task is to provide technical data on the effects of cracks in nickel-alloy components on residual life, inspection, and repair. The results will be used to support NRR staff assessments of industry crack growth models, and potential detection and mitigation measures.

(d) *Analyses of postwelding heat treatment processes and validation of flaw acceptance criteria*

The objective of this task is to evaluate the effect of postwelding heat treatment on long-term resistance to environmental cracking by assessing sensitization and other microstructural changes. This evaluation will provide NRC with insights for use in reviewing licensee submittals.

(e) *Assess industry crack-growth models*
This task has two objectives. The first is to perform an independent evaluation of industry models that are used to establish inspection intervals and repair criteria. The second objective is to perform more detailed analyses of flaw acceptance criteria.

Research during this six-month reporting period has focused on fatigue of carbon steels (CSs) and low-alloy ferritic steels (LASs) and SSs used in piping and pressure vessels, IASCC during slow-strain-rate tensile (SSRT) tests in simulated BWR water of SS specimens that were irradiated to a low fluence in the Halden reactor, and EAC of Alloys 600 in high-purity (HP) oxygenated water.

2 Environmental Effects on Fatigue Strain-versus-Life (S–N) Behavior of Austenitic Stainless Steels (O. K. Chopra, J. L. Smith, and W. J. Shack)

2.1 Introduction

Experience with operating nuclear plants worldwide reveals that many failures may be attributed to fatigue. Examples of such failures include emergency core cooling or residual heat removal systems (USNRC Bulletin No. 88-08), pressurizer surge lines (USNRC Bulletin No. 88-11), PWR feedwater lines (USNRC Information Notice No. 79-13), BWR pressure vessels (USNRC Information Notice No. 90-29), PWR steam generator vessels (USNRC Information Notice No. 90-04), steam generator feedwater distribution piping (USNRC Information Notice No. 91-19 and No. 93-20), and reactor coolant thermal barrier housing (USNRC Information Notice No. 97-31). These failures may be classified into three categories: thermal fatigue caused by thermal stratification, cycling, and striping loadings; mechanical fatigue due to vibratory loading; and corrosion fatigue resulting from the exposure to aqueous environments. Significant thermal loadings due to stratification were not included in the original design basis analysis. Some of these fatigue-sensitive locations in nuclear power plants are routinely monitored worldwide to better define the transients and for more accurate assessment of cumulative usage factors (CUF). Occurrences of mechanical-vibration- and thermal-fluctuation-induced fatigue failures in LWR plants in Japan have also been documented.[1]

Cyclic loadings on a structural component occur because of changes in the mechanical and thermal loadings as the system goes from one set of pressure, temperature, moment, and force loading to any other load set. For each pair of load sets, an individual fatigue usage factor is determined by the ratio of the number of cycles anticipated during the lifetime of the component to the allowable cycles. Figures I-9.1 to I-9.6 of Appendix I to Section III of the ASME Boiler and Pressure Vessel Code specifies fatigue design curves that define the allowable number of cycles as a function of applied stress amplitude. The CUF is the sum of the individual usage factors, and the ASME Code Section III requires that the CUF at each location must not exceed 1.

The Code design fatigue curves were based on strain-controlled tests of small polished specimens at room temperature in air. The design fatigue curves were obtained by first adjusting the best-fit curves for the effects of mean stress and then the curves are decreased by a factor of 2 on stress or 20 on cycles, whichever was more conservative, at each point on the best-fit curve. As described in the Section III criteria document, these factors were intended to account for the differences and uncertainties in relating the fatigue lives of laboratory test specimens to those of actual reactor components. Although the factors of 2 and 20 were intended to be somewhat conservative, they should not be considered as safety margins but rather conversion factors that must be applied to the experimental data to obtain reasonable estimates of the lives of actual reactor components. These results raise the issue whether the design fatigue curves in Section III are appropriate for the purposes intended and whether they adequately account for environmental effects on fatigue behavior.

Subsection NB-3121 of Section III of the Code states that the data on which the fatigue design curves (Figs. I-9.1 to I-9.6) are based did not include tests in the presence of corrosive environments that might accelerate fatigue failure. Article B-2131 in Appendix B to Section III states that the owner's design specifications should provide information about any reductions to fatigue design curves that are necessitated by environmental conditions. Recent fatigue strain-vs.-life (S-N) data demonstrate potentially significant effects of LWR coolant environments on the fatigue resistance of carbon and low-alloy steels,[2-14] and austenitic SSs,[2,15-19] Fig. 1. Under certain conditions of loading and environment, fatigue lives of carbon steels can be a factor of 70 lower in the environment than those in air.[6,12-14] Therefore, the margins in the ASME Code may be less conservative than originally intended.

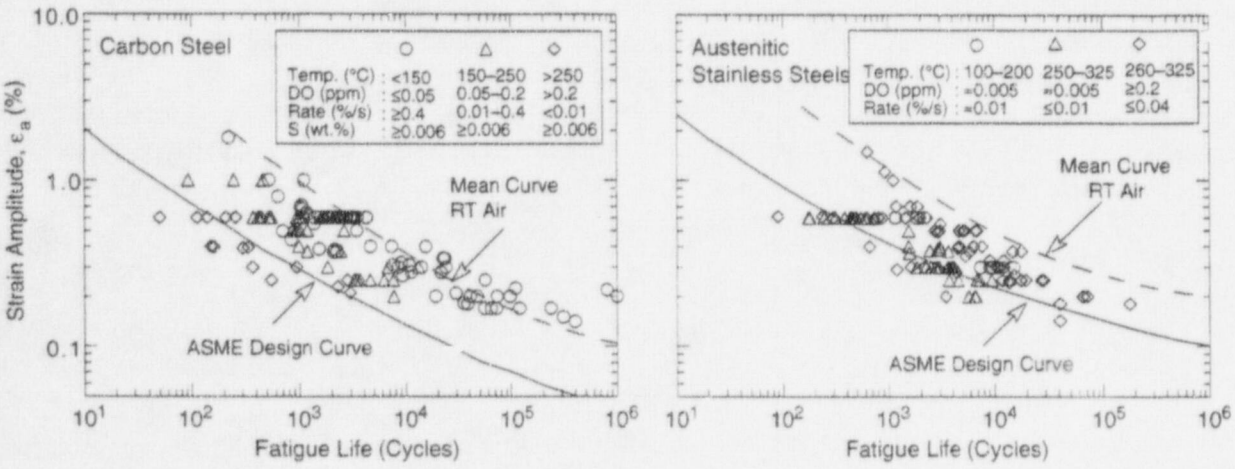

Figure 1. Fatigue S-N data for carbon steels and austenitic SSs in water

A program was initiated at Argonne National Laboratory (ANL) to provide data and models for predicting the effects of environment on fatigue design curves and to assess the additivity of fatigue damage in piping and vessel steels under load histories typical of LWR components. The data will be used by the NRC staff to assess industry fatigue evaluations related to license renewal. The information, which will be helpful in assessing applicant submissions with regard to residual lifetimes of components subjected to fatigue in reactor coolant environments, will be provided to the ASME to help improve the design curves. Fatigue tests are being conducted to establish the effects of various loading and environmental variables on the fatigue S–N behavior of pressure boundary steels.

Based on the existing fatigue S-N data, interim design fatigue curves that address environmental effects on fatigue lives of carbon and low-alloy steels and austenitic SSs have been proposed.[20] Statistical models have also been developed at ANL for estimating the effects of various material and loading conditions on fatigue lives of these materials.[21,22] Results of the statistical analysis have been used to estimate the probability of fatigue cracking in reactor components. The statistical models for carbon and low-alloy steels have recently been updated with a larger fatigue S–N data base.[14] The experimental effort is currently focused on the effects of LWR environments on the fatigue lives of wrought and cast austenitic SSs.

The interim design curve and statistical model for austenitic SSs were based on limited data. For example, nearly all of the data in water were obtained at high temperatures (280–320°C) and high levels of dissolved oxygen (DO) (0.2–8 ppm). The data were inadequate to define the loading and environmental conditions that can decrease the fatigue lives of austenitic SSs. The threshold for strain amplitude above which environment can decrease fatigue life, and the value of strain rate below which environmental effects saturate, were based on the data for carbon and low-alloy steels. Fatigue life in LWR environments was assumed to be independent of temperature. Furthermore, although the proposed interim fatigue design curve[21] for austenitic SSs was based on data obtained in high-DO water, the curve was recommended for use at all oxygen levels until additional data became available, on the assumption that this was a conservative estimate of the likely effect of DO. Recent experimental results indicate that the above assumption is not true.[18,19] Also, effects of LWR environments on the fatigue lives of cast SSs have not been addressed.

This report summarizes available data on the effects of various material and loading variables such as steel type, DO level, strain range, and strain rate, on the fatigue lives of wrought and cast austenitic SSs. The data have been analyzed to identify key parameters that influence fatigue life and define the threshold and saturation values of these parameters. Statistical models that were developed earlier for estimating the fatigue lives of austenitic SSs in LWR environments have been updated with a larger data base. The significance of the effect of environment on the current Code design curve is evaluated.

2.2 Experimental

Fatigue tests have been conducted on Types 316NG and 304 SS to establish the effects of LWR coolant environments on fatigue lives of these steels. The chemical composition of the two steels is given in Table 1. Smooth cylindrical specimens with 9.5-mm diameter and 19-mm gage length were used for the fatigue tests (Fig. 2). The specimen gage length was given a 1-μm surface finish in the axial direction to prevent circumferential scratches that might act as sites for crack initiation.

Table 1. Composition (in wt.%) of wrought and cast SSs used for fatigue tests

Material	Heat	Source	C	P	S	Si	Cr	Ni	Mn	Mo	Cu	N
Type 316NG[a]	D432804	Vendor	0.011	0.020	0.001	0.52	17.55	13.00	1.76	2.49	0.10	0.108
		ANL	0.013	0.020	0.002	0.49	17.54	13.69	1.69	2.45	0.10	0.105
Type 304[b]	30956	Vendor	0.060	0.019	0.00?	0.48	18.99	8.00	1.54	0.44	-	0.100
CF-8M	74	ANL	0.064	-	-	0.73	19.11	9.03	0.54	2.51	-	0.048
CF-8M	75	ANL	0.065	-	-	0.67	20.86	9.12	0.53	2.58	-	0.052

[a]ASME SA312 seamless stainless steel pipe (hot finished), 610 mm O.D. and 30.9 mm wall, fabricated by Sumitomo Metal Industries, Ltd. Solution-annealed at 1038–1093°C for 0.5 h and water-quenched.
[b]Solution-annealed at 1050°C for 0.5 h.
[c]Solution-annealed at 1065–1120°C and water quenched, measured ferrite content 18%.
[d]Solution-annealed at 1065–1120°C and water quenched, measured ferrite content 28%.

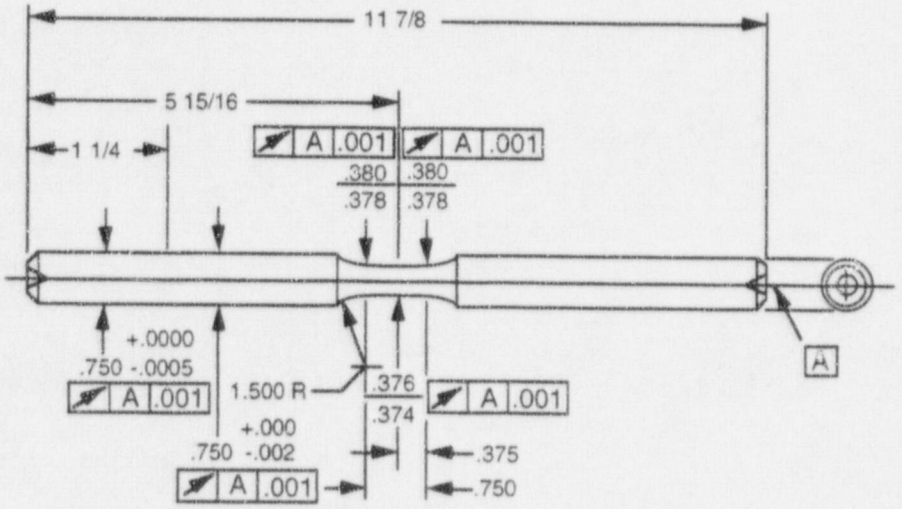

Figure 2. Configuration of fatigue test specimen (all dimensions in inches)

Tests in water were conducted initially in a once-through system consisting of a 132-L supply tank, Pulsafeeder™ pump, heat exchanger, preheater, and an autoclave with an annular volume of 12 mL. Water was circulated at a rate of ≈10 mL/min and a system pressure of 9 MPa. A detailed description of the system has been presented elsewhere.[10,14] An Orbisphere meter and CHEMetrics™ ampules were used to measure the DO concentrations in the supply and effluent water. The redox and open-circuit corrosion potentials were monitored at the autoclave outlet by measuring electrochemical potentials (ECPs) of platinum and an electrode of the test material, respectively, against a 0.1 M KCl/AgCl/Ag external (cold) reference electrode. The measured ECPs, $E_{(meas)}$ (mV), were converted to the standard hydrogen electrode (SHE) scale, $E_{(SHE)}$ (mV), by the polynomial expression[23]

$$E_{(SHE)} = E_{(meas)} + 286.637 - 1.0032(\Delta T) + 1.7447\times10^{-4}(\Delta T)^2 - 3.03004\times10^{-6}(\Delta T)^3, \quad (1)$$

where ΔT(°C) is the temperature difference of the salt bridge in a 0.1 M KCl/AgCl/Ag external reference electrode (i.e., the test temperature minus ambient temperature).

The test facility has now been modified from a once-through system to a recirculating system. For fatigue tests in high-DO environments, an ion-exchange filter was placed in the

return line to maintain high resistivity of the water. Also, a filter was installed in the cover gas line to eliminate possible contamination. A schematic diagram of the recirculating system is shown in Fig. 3. Several scoping tests have been conducted to determine possible changes in water chemistry during extended periods. The DO level in the feedwater was maintained either at 0.45 or 1.0 ppm during these tests. The results indicate that after an initial transition period during which an oxide film develops on the fatigue sample, both the DO level and ECP remain constant during the test. Although the difference in the DO levels between the feedwater and effluent water is >0.1 ppm, the difference between the inlet and outlet of the autoclave is ≈0.02 ppm. A similar recirculating system is used for fatigue tests in low-DO simulated PWR environments, except that the ECP cell is bypassed during recirculation and the ion-exchange filter in the return line from the autoclave to the water supply tank is also excluded.

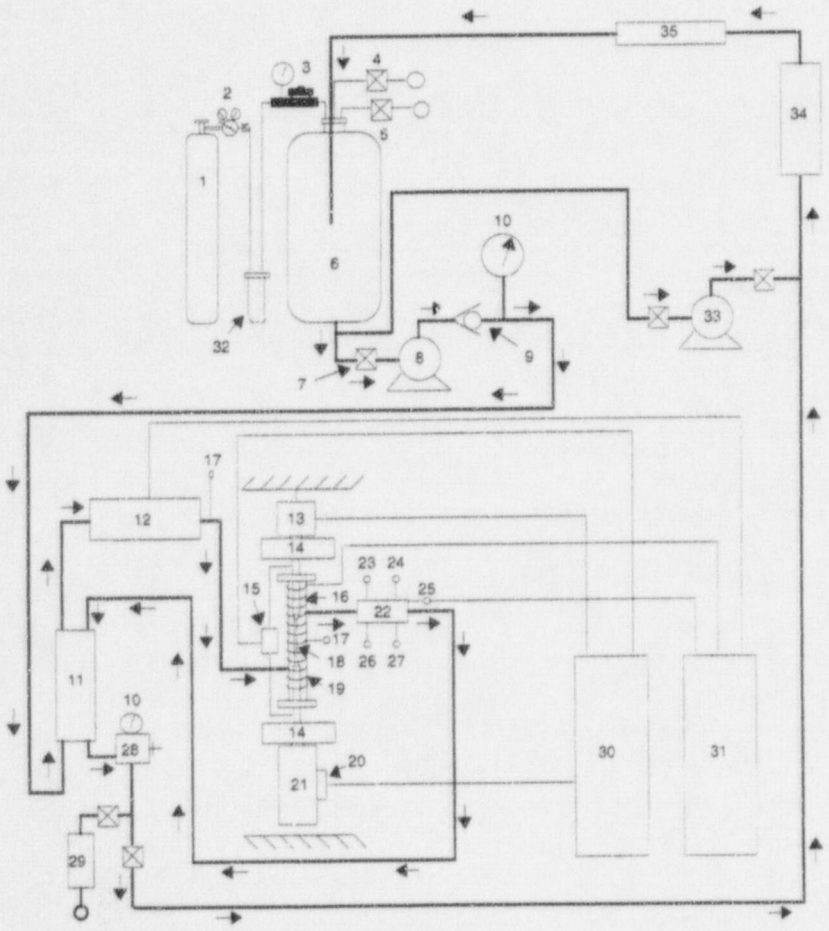

1. Cover-gas supply tank
2. High-pressure regulator
3. Low-pressure regulator
4. Vent to air valve
5. Pressure relief valve
6. Water supply tank
7. Main water shutoff valve
8. Pulsafeeder high-pressure pump
9. Check valve
10. High-pressure gauge
11. Heat exchanger
12. Preheat exchanger
13. MTS load cell
14. MTS hydraulic collet grips
15. Displacement LVDT
16. Pipe autoclave
17. Control and measuring thermocouples
18. Fatigue test specimen
19. Resistance heaters
20. MTS servovalve
21. MTS hydraulic actuator
22. ECP cell
23. Platinum electrode
24. ECP thermocouple
25. ECP heater
26. Specimen electrode
27. Reference electrode
28. Mity Mite™ back-pressure regulator
29. Orbisphere dissolved-oxygen meter
30. MTS electrohydraulic controls
31. Resistance heater controls
32. Cover gas purifier
33. Recirculation pump
34. Demineralizer
35. 0.2 μm filter

Figure 3. Schematic diagram of recirculating autoclave system for fatigue tests in water

The DO level in water was established by bubbling nitrogen that contains 1-2% oxygen through deionized water in the supply tank. The deionized water was prepared by passing purified water through a set of filters that comprise a carbon filter, an Organex-Q filter, two ion exchangers, and a 0.2-mm capsule filter. Water samples were taken periodically to measure pH, resistivity, and DO concentration. After the desired concentration of DO was achieved, the nitrogen/oxygen gas mixture in the supply tank was maintained at a 20-kPa

overpressure. After an initial transition period during which an oxide film develops on the fatigue specimen, both the DO level and the ECP in the effluent water remained constant during the test. Test conditions are described in terms of the DO in effluent water.

Simulated PWR water was obtained by dissolving boric acid and lithium hydroxide in 20 L of deionized water before adding the solution to the supply tank. The DO in the deionized water was reduced to <10 ppb by bubbling nitrogen through the water. A vacuum was drawn on the tank cover gas to speed deoxygenation. After the DO was reduced to the desired level, a 34–kPa overpressure of hydrogen was maintained to provide ≈2 ppm dissolved hydrogen (or ≈23 $cm^3 \cdot kg^{-1}$) in the feedwater.

All tests were conducted at 288°C with fully reversed axial loading (i.e., R = –1) and a triangular or sawtooth waveform. The strain rate for the triangular wave and fast–loading half of the sawtooth wave was 0.4%/s. The tests in water were performed under stroke control, where the specimen strain was controlled between two locations outside the autoclave. Tests in air were performed under strain control with an axial extensometer; the stroke at the location used for control in the water tests was also recorded. Information from the air tests was used to determine the stroke required to maintain constant strain in the specimen gauge length. To account for cyclic hardening of the material, the stroke needed to maintain constant strain was gradually increased during the test. The actual strain in the specimen gauge section during a stroke–controlled tests with a sawtooth waveform is shown in Fig. 4. The fraction of applied displacement that goes to the specimen gauge section is not constant but varies with the loading strain. Consequently, the loading rate also varies during the fatigue cycle; it is lower than the applied strain rate at strain levels below the elastic limit and higher at larger strains.

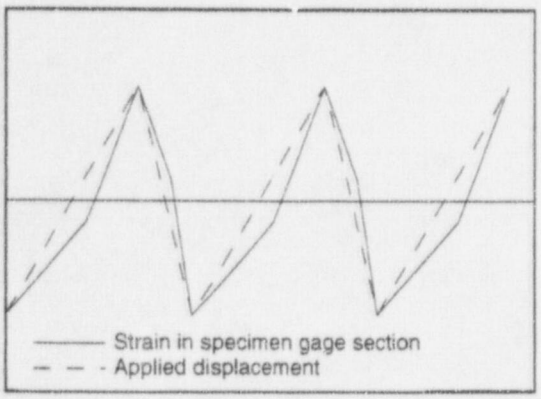

Figure 4.
Loading strain applied to specimen gauge section (solid line) during stroke–controlled tests with sawtooth waveform (dashed line)

The fatigue test data obtained to date on Types 316NG and 304 SS in air and LWR environments are listed in Tables 2 and 3. During the present reporting period, fatigue tests have been conducted on two heats of CF–8M cast SSs to establish environmental effects on the fatigue life of these steels. The chemical composition of the CF–8M steels is given in Table 1; the fatigue test results are listed in Table 4. Tests were conducted on both unaged material and material that was aged for 10,000 h at 400°C. However, during strain control tests in air, both steels showed strain ratcheting in compression. Although strain in the gage section of the specimens remained constant, overall length of the specimens decreased during the test. The results indicated that strain ratcheting was caused by differences in the strain hardening behavior of these steels in tension and compression. For both steels, strain

Table 2. Fatigue test results for Type 316NG SS

Test No.	Environ.	Diss. Oxygen [a] (ppb)	pH at RT	Conduc-tivity (μS/cm)	Ten. Rate (%/s)	Comp. Rate (%/s)	Stress Range (MPa)	Strain Range (%)	Life N_{25} (Cycles)
Room Temp.									
1394	Air	–	–	–	5.0E-1	5.0E-1	694.7	1.51	4,649
1391	Air	–	–	–	5.0E-1	5.0E-1	554.8	1.00	13,561
1390	Air	–	–	–	5.0E-1	5.0E-1	518.1	0.75	25,736
1396	Air	–	–	–	5.0E-1	5.0E-1	506.7	0.76	30,000
1420	Air	–	–	–	4.9E-1	4.9E-1	495.3	0.49	54,249
1392	Air	–	–	–	5.0E-1	5.0E-1	475.9	0.51	60,741
1393	Air	–	–	–	5.0E-1	5.0E-1	464.7	0.41	127,386
1395	Air	–	–	–	5.0E-1	5.0E-1	456.7	0.35	183,979
1397	Air	–	–	–	5.0E-1	5.0E-1	446.0	0.30	347,991
1398	Air	–	–	–	5.0E-1	5.0E-1	436.7	0.27	666,000
1399	Air	–	–	–	5.0E-1	5.0E-1	431.8	0.25	>1,900,000
1400	Air	–	–	–	5.0E-1	5.0E-1	427.4	0.25	1,775,000
288°C									
1408	Air	–	–	–	5.0E-1	5.0E-1	416.6	0.76	21,548
1790	Air	–	–	–	5.0E-3	5.0E-1	452.8	0.75	16,765
1409	Air	–	–	–	5.0E-1	5.0E-1	377.2	0.50	53,144
1410	Air	–	–	–	5.0E-1	5.0E-1	377.6	0.50	51,194
1792	Air				5.0E-3	5.0E-1	413.4	0.51	35,710
1407	Air	–	–	–	5.0E-1	5.0E-1	364.4	0.40	82,691
1430	Air	–	–	–	5.0E-1	5.0E-1	348.3	0.30	168,852
1435	Air	–	–	–	5.0E-1	5.0E-1	342.0	0.25	314,352
1480	Air	–	–	–	4.9E-1	4.9E-1	340.1	0.25	319,308
1485	Air	–	–	–	5.1E-1	5.1E-1	340.4	0.25	369,206
320°C									
1405	Air	–	–	–	5.0E-1	5.0E-1	426.0	0.75	20,425
1404	Air	–	–	–	5.0E-1	5.0E-1	387.4	0.50	47,011
1406	Air	–	–	–	5.0E-1	5.0E-1	371.6	0.40	82,691
288°C									
1426	Hi DO	>200	–	–	8.0E-1	8.0E-1	405.1	0.80	12,069
1427	Hi DO	>200	–	–	8.2E-2	8.2E-2	421.7	0.82	6,679
1428	Hi DO	>200	–	–	7.4E-3	7.4E-3	441.4	0.74	5,897
1797	Hi DO	750	5.9	0.076	5.0E-3	5.0E-1	437.3	0.78	4,520
1414	Hi DO	>200	–	–	5.0E-1	5.0E-1	375.3	0.50	26,230
1418	Hi DO	>200	–	–	5.0E-1	5.0E-1	375.5	0.50	25,714
1423	Hi DO	>200	–	–	5.0E-2	5.0E-2	378.8	0.50	17,812
1425	Hi DO	>200	–	–	4.9E-3	4.9E-3	393.2	0.49	13,684
1431	Hi DO	>200	–	–	2.9E-1	2.9E-1	356.5	0.29	116,754
1434	Hi DO	>200	–	–	2.9E-2	2.9E-2	350.0	0.29	40,643
1436	Hi DO	>200	–	–	2.5E-2	2.5E-2	354.0	0.25	>1,719,851
1512	Hi DO	>200	–	–	2.4E-1	2.4E-1	361.2	0.24	2,633,954
1796	PWR	5	6.4	20.20	5.0E-1	5.0E-1	403.6	0.80	12,500
1812	PWR	2	6.5	20.00	5.0E-2	5.0E-1	413.9	0.80	6,375
1791	PWR	4	6.5	19.23	5.0E-3	5.0E-1	441.9	0.77	3,040
1793	PWR	4	6.4	19.23	5.0E-3	5.0E-1	434.3	0.80	3,020
1794	PWR	4	6.4	20.00	5.0E-3	5.0E-1	390.9	0.50	7,370
1814	PWR	1	6.5	20.00	5.0E-2	5.0E-1	348.7	0.29	33,200

[a] PWR = simulated PWR water containing 2 ppm lithium and 1000 ppm boron.

hardening is greater in compression than in tension. This difference results in a mean compressive stress, which causes strain ratcheting of the shoulder region of the specimens. To prevent strain racheting, tests in water were conducted under stroke control with a low tensile strain.

Table 3. Fatigue test results for Type 304 SS at 288°C

Test No.	Environ.	Diss. Oxygen [a] (ppb)	pH at RT	Conductivity (μS/cm)	Ten. Rate (%/s)	Comp. Rate (%/s)	Stress Range (MPa)	Strain Range (%)	Life N_{25} (Cycles)
1801	Air	–	–	–	4.0E-1	4.0E-1	419.2	0.76	24,500
1805	Air	–	–	–	4.0E-3	4.0E-1	467.9	0.76	14,410
1804	Air	–	–	–	4.0E-1	4.0E-1	382.8	0.51	61,680
1817	Air	–	–	–	4.0E-3	4.0E-1	421.7	0.51	42,180
1825	Air	–	–	–	4.0E-2	4.0E-1	394.4	0.30	625,860
1806	PWR	4	6.0	18.87	4.0E-1	4.0E-1	428.9	0.73	11,500
1810	PWR	5	6.4	18.89	4.0E-2	4.0E-1	447.6	0.77	5,800
1808	PWR	4	6.4	18.87	4.0E-3	4.0E-1	468.3	0.77	2,850
1821	PWR	2	6.5	22.22	4.0E-3	4.0E-1	474.3	0.76	2,420
1829	PWR	2	6.5	18.18	4.0E-4	4.0E-1	493.6	0.73	1,560
1834	PWR	2	6.5	18.18	9.0E-5	4.0E-1	535.9	0.69	1,415
1807	PWR	4	6.5	18.87	4.0E-1	4.0E-1	374.6	0.51	25,900
1823	PWR	3	6.6	23.06	4.0E-3	4.0E-1	408.2	0.51	6,900
1826	PWR	2	6.5	18.76	1.0E-2	4.0E-1	375.8	0.29	>89,860
1827	Hi DO	850	6.0	0.086	4.0E-3	4.0E-1	475.8	0.75	3,650

[a] PWR = simulated PWR water containing 2 ppm lithium and 1000 ppm boron.

Table 4. Fatigue test results for CF-8M cast SSs at 288°C

Test No.	Environ.	Diss. Oxygen [a] (ppb)	pH at RT	Conductivity (μS/cm)	Ten. Rate (%/s)	Comp. Rate (%/s)	Stress Range (MPa)	Strain Range (%)	Life N_{25} (Cycles)
Unaged Heat 74									
1831	Air	–	–	–	4.0E-1	4.0E-1	429.7	0.76	26,500
1832	Air	–	–	–	4.0E-3	4.0E-1	534.0	0.76	9,050
Aged Heat 74									
1839	Air	–	–	–	4.0E-1	4.0E-1	474.2	0.76	15,293
1840	Air	–	–	–	4.0E-3	4.0E-1	534.8	0.75	19,800
1844	PWR	–	–	–	4.0E-3	4.0E-1	527.7	0.72	2,180
1842	Hi DO	–	–	–	4.0E-3	4.0E-1	508.5	0.75	1,375
Aged Heat 75									
1835	Air	–	–	–	4.0E-3	4.0E-1	631.2	0.76	7,200
1843	PWR	–	–	–	4.0E-3	4.0E-1	625.3	0.80	1,464
1838	Hi DO	–	–	–	4.0E-3	4.0E-1	636.1	0.78	1,320

[a] PWR = simulated PWR water containing 2 ppm lithium and 1000 ppm boron.

2.3 Overview of Fatigue S–N Data

The relevant fatigue S–N data for austenitic SSs in air include the data compiled by Jaske and O'Donnell[24] for developing fatigue design criteria for pressure vessel alloys, the JNUFAD* data base from Japan, and the results of Conway et al.[25] and Keller.[26] In water, the existing fatigue S–N data include the tests performed by General Electric Co. (GE) in a test loop at the Dresden 1 reactor,[2] the JNUFAD data base, the present work at ANL on fatigue of pressure vessel and piping steels,[16,19] studies at Ishikawajima-Harima Heavy Industries Co., (IHI),[18]

* M. Higuchi, Ishikawajima-Harima Heavy Industries Co., Japan, private communication to M. Prager of the Pressure Vessel Research Council, 1992.

and a joint study at Mitshubishi Heavy Industries, Ltd., (MHI) with five Japanese utilities.* The data base for austenitic SSs is composed of 500 tests in air (240 tests on 26 heats of Type 304 SS, 170 tests on 15 heats of Type 316 SS, and 90 tests on 4 heats of Type 316 NG) and 290 tests in water (135 tests for 9 heats of Type 304, 55 tests on 3 heats of Type 316 SS, and 100 for 4 heats of Type 316 NG). Nearly 60% of the tests in air were conducted at room temperature, 20% at 250–325°C, and 20% at 350–450°C. Nearly 90% of the tests in water were conducted between 260–325°C; the remainder were at lower temperatures. The data in water on Type 316NG have been obtained primarily at high DO levels (≥ 0.2 ppm) and those on Type 316 SS at low-DO levels (≤0.005 ppm); half the tests on Type 304 SS are at low-DO and the remaining at high-DO levels.

2.3.1 Air Environment

The existing fatigue S–N data, both domestic and from abroad, indicate that the fatigue lives of Types 304 and 316 SS are comparable and those of Type 316NG are superior. Fatigue life in air is independent of temperature in the range from room temperature to 427°C (Fig. 5). The three curves in Fig. 5 are based on the current ASME mean curve, the best-fit curve

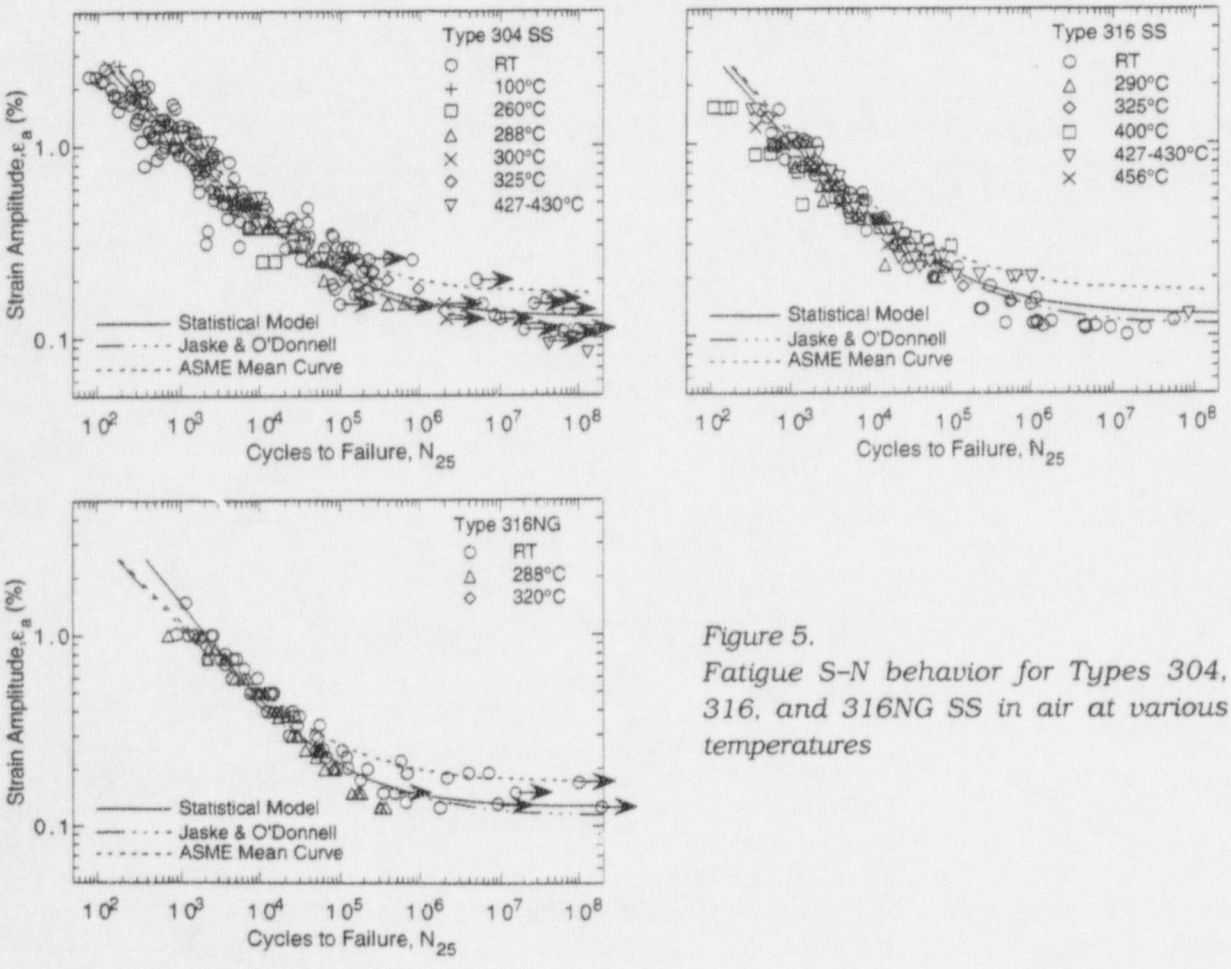

Figure 5.
Fatigue S–N behavior for Types 304, 316, and 316NG SS in air at various temperatures

* H. Kanasaki, "Fatigue Life of Stainless Steels and Alloy 600 in PWR Primary Water," presented at the Pressure Vessel Research Council Meeting, October 7–9, 1996, Columbus, OH.

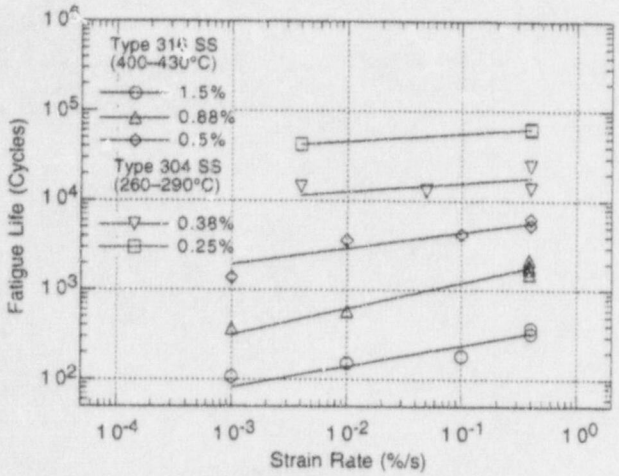

Figure 6.
Effect of strain rate on fatigue lives of austenitic SSs in air

developed by Jaske and O'Donnell,[24] and an updated statistical model discussed later in the paper. The data for temperatures of 260–400°C indicate that the fatigue lives of these steels decreases with decreasing strain rate (Fig. 6). Strain rate effects are not observed at room temperature. Above 260°C, the effect of strain rate on life seems to increase with increasing temperature.

During cyclic loading, austenitic SSs exhibit rapid hardening during the first 50–100 cycles. Extent of hardening increases with increasing strain amplitude and decreasing temperature and strain rate.[19] The initial hardening is followed by softening and a saturation stage at 288°C and by continuously softening at room temperature. For the various steels, cyclic stresses increase in magnitude in the following order: Types 316NG, 304, and 316. The correlations for cyclic stress vs. strain curves have been presented elsewhere.[19]

2.3.2 LWR Environments

The fatigue S–N data indicate a significant decrease in fatigue life in LWR environments (Fig. 7). The reduction in life depends on strain rate, DO level in water, and temperature.[15–19] Also, environmental effects on fatigue life are comparable for all steels. A slow strain rate applied during the tensile-loading cycle (i.e., up-ramp with increasing strain) is primarily responsible for environmentally assisted reduction in fatigue life. A slow rate applied during both tensile- and compressive-loading cycles (i.e., up- and down-ramps) does not cause further decrease in fatigue life.[19]

The fatigue lives of austenitic SSs in low- and high-DO water are plotted as a function of tensile strain rate in Fig. 8. In both low- and high-DO levels, fatigue lives decrease with decreasing strain rate. The effect of strain rate is greater in a low-DO PWR environment than in high-DO water. In a simulated PWR environment, a decrease in strain rate from 0.4 to 0.0004%/s decreases fatigue life by a factor of ≈10. The results indicate that the strain rate below which effects of strain rate on fatigue life saturate may depend both on steel type and DO level. In low-DO PWR environments, saturation strain rate appears to be at ≈0.0004%/s for Type 304 SS and somewhat higher for Type 316 SS (best estimate of ≈0.004%/s). The existing data are inadequate to establish saturation rate in high-DO water.

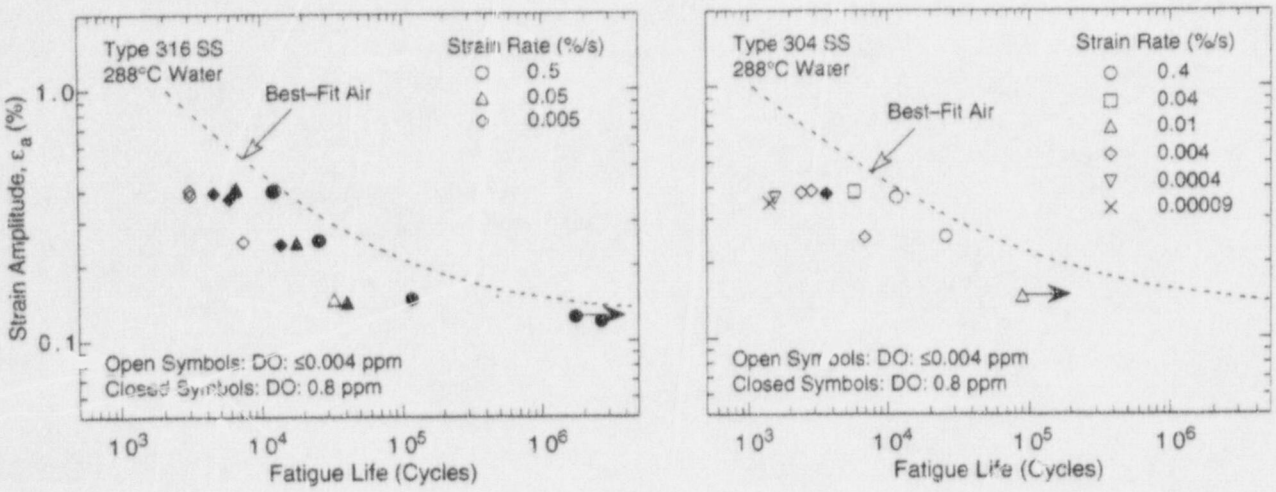

Figure 7. Fatigue strain amplitude versus life data for Types 316NG and 304 SS in water

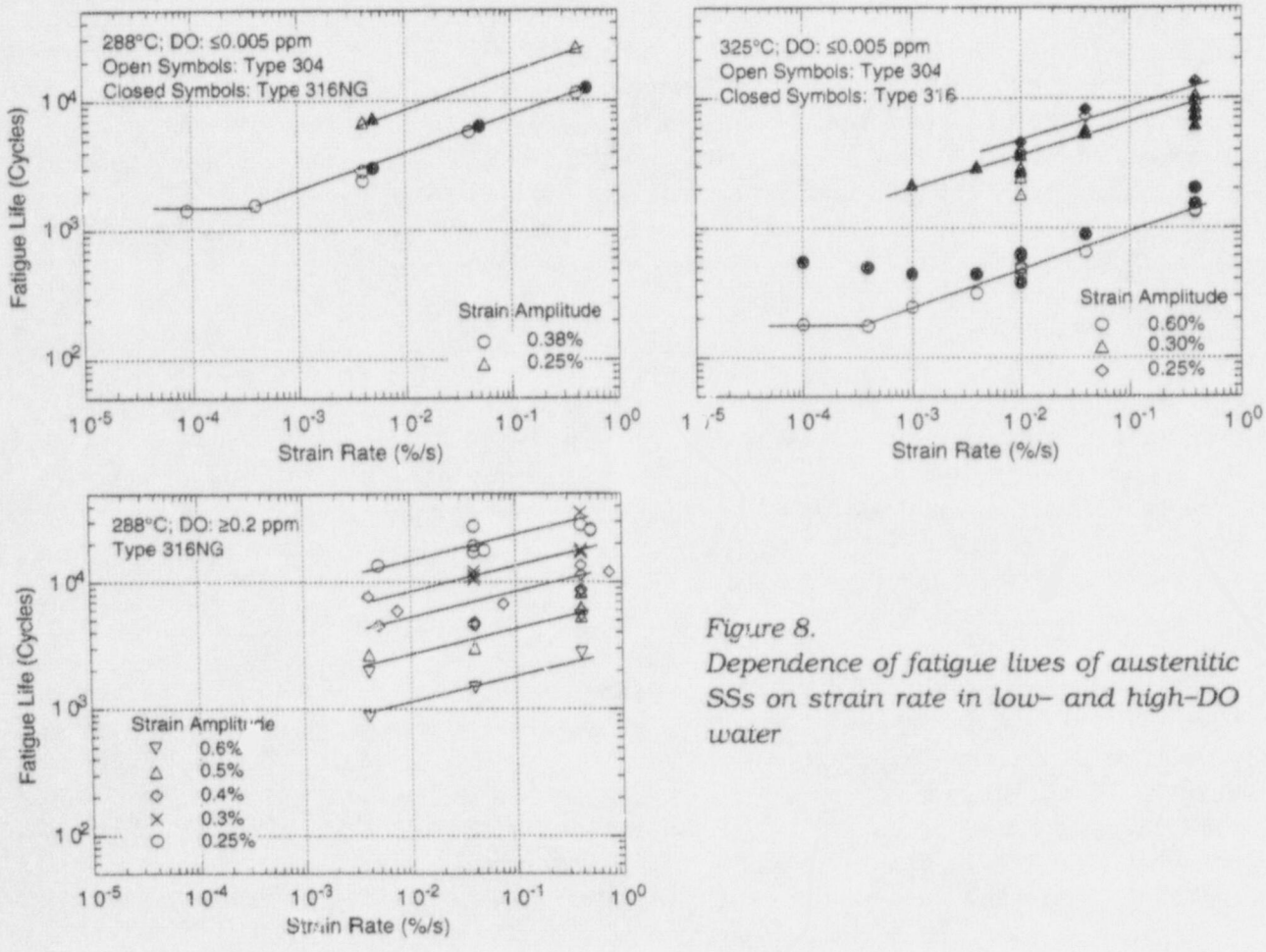

Figure 8.
Dependence of fatigue lives of austenitic SSs on strain rate in low- and high-DO water

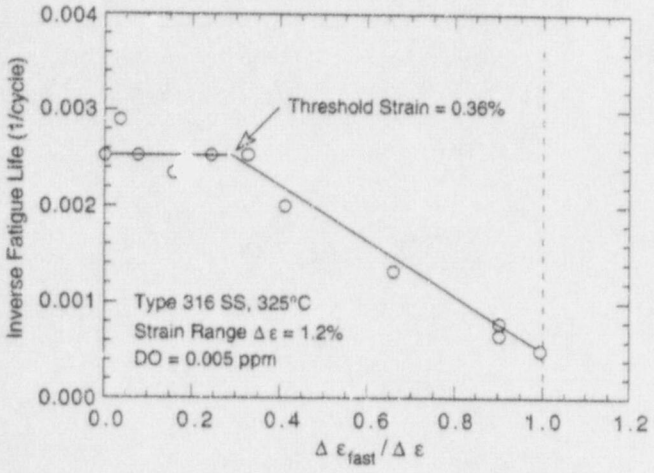

Figure 9.
Results of strain rate change tests on Type 316 SS in low-DO water at 325°C

Results from exploratory tests,* where a slow strain rate is applied during only a fraction of the tensile loading cycle, indicate that a minimum threshold strain is required for environmentally assisted decrease in fatigue lives of these steels. For a heat of Type 316 SS, the threshold strain in low-DO water at 325°C is ≈0.36% (Fig. 9). During each cycle, relative damage due to slow strain rate is the same once the strain amplitude exceeds the threshold value. Fatigue data from the present study indicate a threshold strain range of ≈0.32% for the ANL heat of Type 304 SS. For example, the test at 0.15% strain amplitude and 0.01%/s strain rate (as shown by a runoff triangle symbol in Fig. 7), failed after an additional 41,240 cycles when the strain amplitude was increased to 0.16%. Fatigue tests are in progress to validate these results and to evaluate possible differences in threshold strain in low- and high-DO environments. The threshold strain most likely corresponds to rupture strain of the passive oxide film. These results are similar to those observed in carbon and low-alloy steels.[12-14]

The results also indicate that unlike carbon and low-alloy steels, environmental effects on the fatigue lives of austenitic SSs are more pronounced in low-DO than in high-DO water.[18,19] At a strain rate of 0.004%/s, the reduction in fatigue life of Type 316NG (Fig. 8) in a simulated PWR environment (<0.01 ppm DO) is greater by a factor of ≈2 than in high-DO water (≥0.2 ppm DO). The existing data are inadequate to establish the functional form for the dependence of fatigue lives of austenitic SSs on DO level. For carbon and low-alloy steels, environmental effects on fatigue life increase with increasing DO content above a minimum threshold value of 0.05 ppm; only a modest decrease in life is observed at DO levels < 0.05 ppm.[6,10-14]

The existing fatigue S-N data are inadequate to establish the functional form for the dependence of life on temperature. Limited data indicate that environmental effects on fatigue lives of austenitic SSs are significant at temperatures above 250°C and are minimal at temperatures ≤ 200°C (Fig. 10). At 250-330°C, fatigue life appears to be relatively insensitive to changes in temperature.

---

* H. Kanasaki, "Effects of Strain Rate and Temperature Change on the Fatigue Life of Stainless Steel in PWR Primary Water," presented at the Pressure Vessel Research Council Meeting, February 3-5, 1997, Las Vegas, NV.

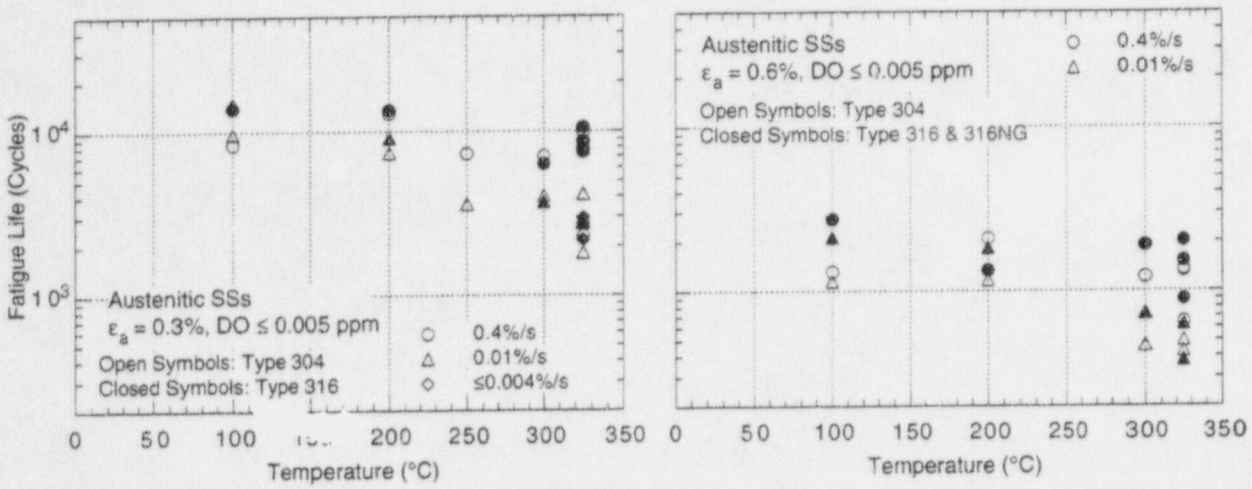

Figure 10. Change in fatigue life of austenitic SSs in low-DO water with temperature

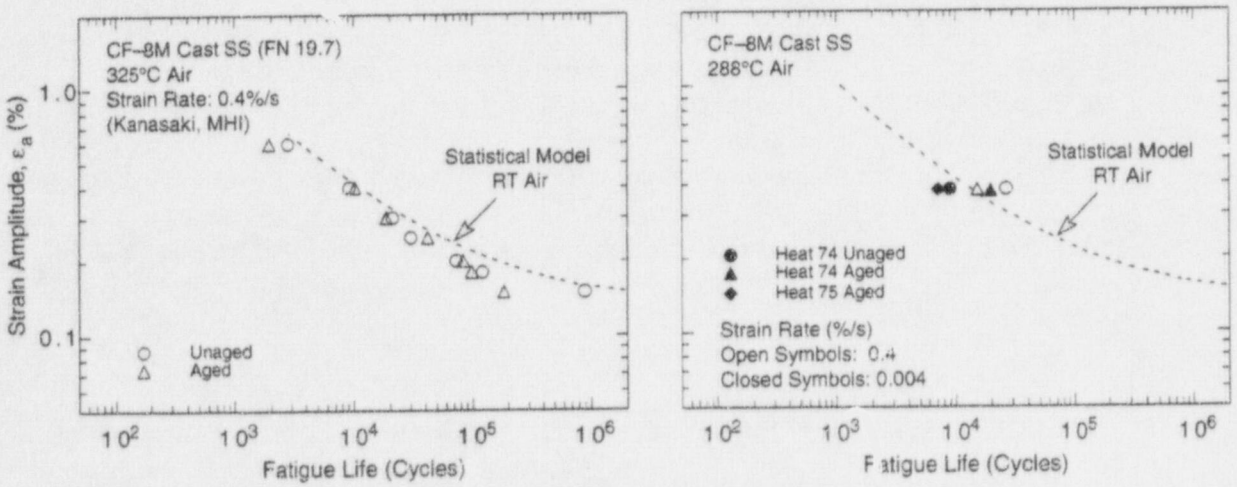

Figure 11. Fatigue strain amplitude versus life data for CF-8M cast SSs in air

2.3.3 Cast Stainless Steels

The available fatigue S–N data indicate that in air, the fatigue lives of cast CF-8 and CF-8M SSs are similar to that of wrought austenitic SSs (Fig. 11). The results also indicate that thermal aging at 400°C has no effect on the fatigue lives of these steels, although it is well known that the Charpy impact and fracture toughness properties of cast SSs are decreased significantly after thermal aging at temperatures between 300–450°C.[27,28] However, cyclic-hardening behavior of cast SSs appears to be influenced by thermal aging (Fig. 12). At 288°C, cyclic stresses of thermally aged cast SSs are higher than those for unaged material or wrought SSs. Also, strain rate effects on cyclic stress are greater for aged than for unaged steel, i.e., cyclic stresses increase significantly with decreasing strain rate.

The existing fatigue S–N data for cast SSs in LWR environments indicate that the fatigue lives of cast SSs are approximately the same in both high- or low-DO water and are comparable to those observed for wrought SSs in low-DO water (Fig. 13). Also, the reduction in life depends on strain rate (Fig. 14). The existing data are inadequate to establish the saturation strain rate for cast SSs. For unaged material, environmental effects on life do not

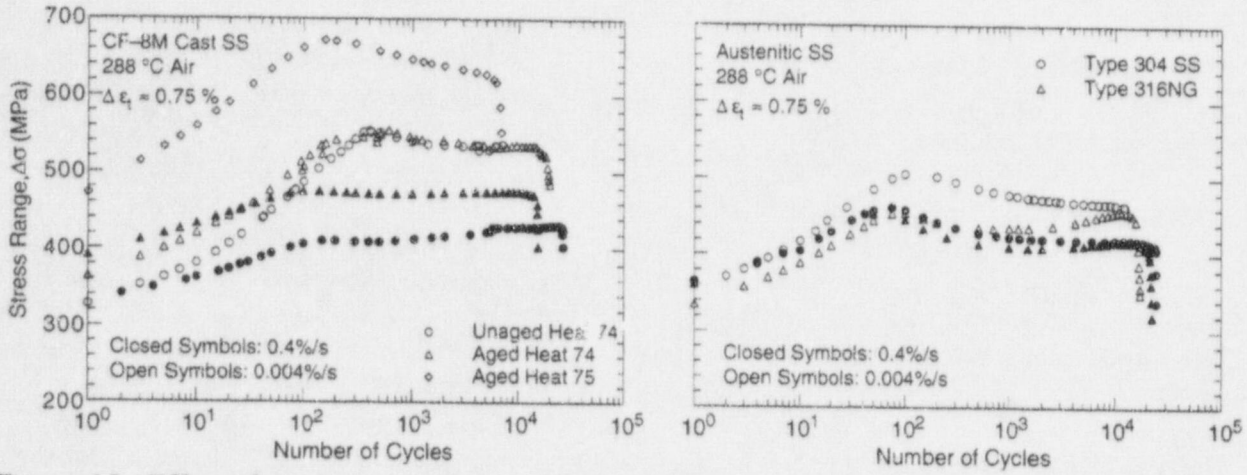

Figure 12. Effect of strain rate on cyclic–hardening behavior of wrought and cast SSs in air at 288°C

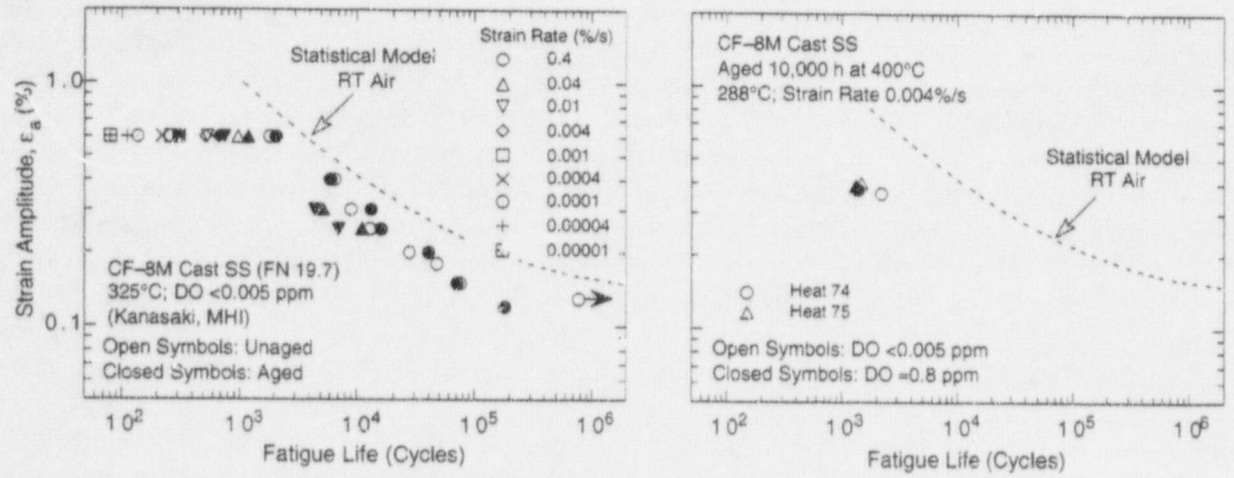

Figure 13. Fatigue strain amplitude versus life data for CF–8M cast SSs in water

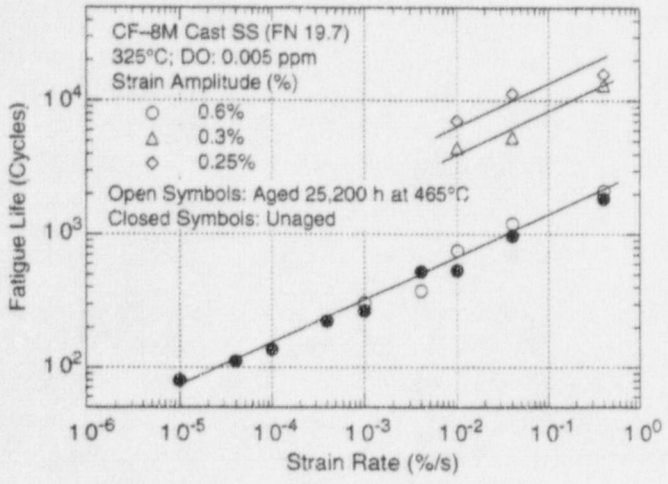

Figure 14. Dependence of fatigue lives of CF–8M cast SSs on strain rate in low–DO water at various strain amplitudes

appear to saturate at strain rates as low as 0.00001%/s. Fatigue tests are in progress to determine the saturation strain rate for these steels in LWR environments. The results also indicate that the fatigue lives of these steels is relatively insensitive to changes in ferrite content in the range of 12–28%.

2.4 Mechanism of Fatigue Crack Initiation

The formation of surface cracks and their growth to an "engineering" size (3 mm deep) constitute the fatigue life of a material, which is represented by the fatigue S–N curves. Fatigue life has conventionally been divided into two stages: (a) initiation, expressed as the cycles to form microcracks on the surface; and (b) propagation, expressed as cycles to propagate the surface cracks to an engineering size. An alternative approach considers fatigue life to be entirely composed of the growth of short surface cracks.[29] In polycrystalline materials, the period for the formation of surface cracks is negligible; surface cracks, 10 μm or longer, form quite early in life.[14,30,31]

The enhanced growth rates of long cracks in pressure vessel and piping steels in LWR environments have been attributed to either slip oxidation/dissolution[32] or hydrogen-induced cracking[33] mechanisms. Both mechanisms are dependent on the rates of oxide rupture, passivation, and liquid diffusion. Therefore, it is often difficult to differentiate between the two processes or to establish their relative contribution to crack growth in LWR environments. Studies on crack initiation in smooth fatigue specimens indicate that the decrease in fatigue lives of carbon and low-alloy steels in LWR environments is caused primarily by the effects of environment on the growth of cracks < 100 μm deep.[14,31] Relative to air, crack growth rates in high-DO water are nearly two orders of magnitude higher for crack sizes < 100 μm and one order of magnitude higher for crack sizes > 100 μm. In LWR environments, crack initiation in carbon and low-alloy steels may be explained as follows: (a) surface microcracks form quite early in fatigue life; (b) during cyclic loading, the protective oxide film is ruptured at strains greater than the fracture strain of surface oxides, and the microcracks grow by anodic dissolution of the freshly exposed surface; and (c) growth of large cracks is characterized by accelerating growth rates.

For austenitic SSs, lower fatigue lives in low-DO water than in high-DO water are difficult to reconcile in terms of the slip oxidation/dissolution mechanism. In general, crack growth rates increase with increasing DO in water. It may be argued that the lower lives in low-DO water are due to a lower rupture strain for surface oxides in low-DO than in high-DO water. As discussed above, oxide rupture strain in low-DO water may be in the range of 0.32–0.36%. The rupture strain in high-DO water must be significantly higher than this value to result in the observed factor of ≈2 difference in fatigue life.

Metallographic examination of the test specimens indicate that environmentally assisted reduction in fatigue lives of austenitic SSs is most likely caused by hydrogen-induced cracking.[31] Figure 15 shows photomicrographs of the fracture surface, after chemical cleaning, at approximately the same crack length for Types 304 and 316NG SS specimens tested at 288°C and ≈0.75% strain range in air, high-DO water, and low-DO simulated PWR environment. All specimens show fatigue striations; the spacing between striations indicate that crack growth increases in the following sequence: air, high-DO water, and low-DO PWR water. The presence of well-defined striations suggests that the enhanced crack growth rates

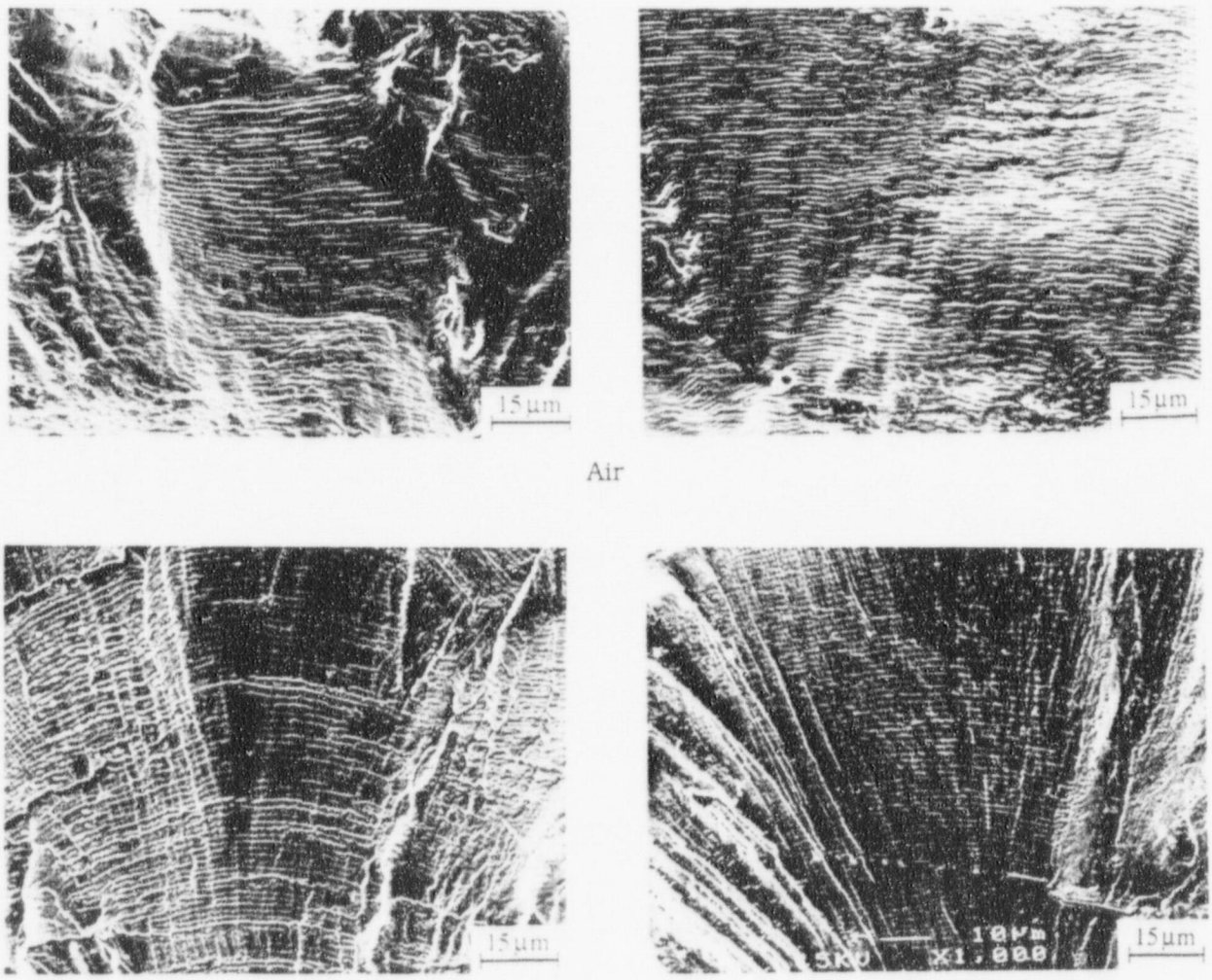

Figure 15. Photomicrographs of fracture surface of Types 304 and 316NG SS specimens tested in air, high-DO water, and low-DO simulated PWR environment

in austenitic SSs are most likely due to hydrogen-induced cracking. Fatigue striations should not be observed if enhancement of crack growth was caused by the slip oxidation/dissolution process.

2.5 Statistical Model

The fatigue S-N curves are generally expressed in terms of the Langer equation,[34] which may be used to represent either strain amplitude in terms of life or life, in terms of strain amplitude. The parameters of the equation are commonly established through least-squares curve-fitting of the data to minimize the sum of the square of the residual errors for either fatigue life or strain amplitude. A predictive model based on least-squares fit on life is biased for low strain amplitude. The model leads to probability curves that converge to a single value of strain, and it fails to address the fact that at low strain values, most of the error in life is due to uncertainty associated with either measurement of strain or variation in fatigue limit caused by material variability. On the other hand, a least-squares fit on strain does not work well for higher strain amplitudes. Statistical models have been developed at ANL[21,22] by combining the two approaches and minimizing the sum of the squared Cartesian distances from the data point to the predicted curve. The functional forms and transformation for the different variables were based on experimental observations and data trends. In the present study, the statistical models developed earlier[21,22] have been modified and updated with a larger fatigue S-N data base.

In air, the model assumes that fatigue life is independent of temperature and that strain rate effects occur at temperatures > 250°C. The effect of strain rate on life is considered to depend on temperature. One data set, obtained on Type 316 SS in room-temperature air, was excluded from the analysis. The tests in this data set were conducted in load-control mode at stress levels in the range of 190–230 MPa. The strain amplitudes were calculated only as elastic strains, i.e., strain amplitudes of 0.1–0.12% (the data are shown as circles in Fig. 5 with fatigue lives of 4×10^5 to 3×10^7). Based on cyclic stress vs. strain correlations for Type 316 SS,[19] actual strain amplitudes for these tests should be 0.23–0.32%. In air, the fatigue life N of Types 304 and 316 SS is expressed as

$$\ln(N) = 6.703 - 2.030 \ln(\varepsilon_a - 0.126) + T^* \dot{\varepsilon}^* \qquad (2a)$$

and that of Type 316NG as

$$\ln(N) = 7.422 - 1.671 \ln(\varepsilon_a - 0.126) + T^* \dot{\varepsilon}^*, \qquad (2b)$$

where ε_a is the strain amplitude (%) and T^* and $\dot{\varepsilon}^*$ are transformed temperature and strain rate, respectively, defined as follows:

$$\begin{aligned} T^* &= 0 && (T < 250°C) \\ T^* &= [(T - 250)/525]^{0.84} && (250 \le T < 400°C) \end{aligned} \qquad (3a)$$

$$\begin{aligned} \dot{\varepsilon}^* &= 0 && (\dot{\varepsilon} > 0.4\%/s) \\ \dot{\varepsilon}^* &= \ln(\dot{\varepsilon}/0.4) && (0.0004 \le \dot{\varepsilon} \le 0.4\%/s) \\ \dot{\varepsilon}^* &= \ln(0.0004/0.4) && (\dot{\varepsilon} < 0.0004\%/s) \end{aligned} \qquad (3b)$$

In LWR environments, the fatigue lives of austenitic SSs depends on strain rate, DO level, and temperature. The decrease in life is greater at low-DO levels and high temperatures.

However, the existing data are inadequate to establish the functional form for the dependence of fatigue life on DO level or temperature. Separate correlations have been developed for low- and high-DO levels (< or ≥ 0.05 ppm), and low and high temperatures (< or ≥ 200°C). Also, a threshold strain rate of 0.4%/s and saturation rate of 0.0004%/s is assumed in the model. Furthermore, for convenience in incorporating environmental effects into fatigue evaluations, the slope of the S–N curve in LWR environments was assumed to be the same as that in air although the best-fit of the experimental data yielded a different slope for the S–N curve than that obtained in air. In LWR environments, the fatigue lives N of Types 304 and 316 SS is expressed as

$$\ln(N) = 5.768 - 2.030 \ln(\varepsilon_a - 0.126) + T^* \dot{\varepsilon}^* O^* \quad (4a)$$

and that of Type 316NG as

$$\ln(N) = 6.913 - 1.671 \ln(\varepsilon_a - 0.126) + T^* \dot{\varepsilon}^* O^*, \quad (4b)$$

where the constants for transformed temperature, strain rate, and DO are defined as follows:

$$\begin{aligned} T^* &= 0 && (T < 200°C) \\ T^* &= 1 && (T \geq 200°C) \end{aligned} \quad (5a)$$

$$\begin{aligned} \dot{\varepsilon}^* &= 0 && (\dot{\varepsilon} > 0.4\%/s) \\ \dot{\varepsilon}^* &= \ln(\dot{\varepsilon}/0.4) && (0.0004 \leq \dot{\varepsilon} \leq 0.4\%/s) \\ \dot{\varepsilon}^* &= \ln(0.0004/0.4) && (\dot{\varepsilon} < 0.0004\%/s) \end{aligned} \quad (5b)$$

$$\begin{aligned} O^* &= 0.260 && (DO < 0.05 \text{ ppm}) \\ O^* &= 0.172 && (DO \geq 0.05 \text{ ppm}) \end{aligned} \quad (5c)$$

The model is recommended for predicted fatigue lives ≤ 10^6 cycles. The experimental values of fatigue life in air and water and those predicted from Eqs. 2–5 are plotted in Fig. 16. The estimated fatigue S–N curves for Types 304, 316, and 316NG SSs in air and LWR environments are shown in Figs. 5 and 17, respectively. The predicted fatigue lives show good agreement with the experimental data. Note that the ASME mean curve is not consistent with

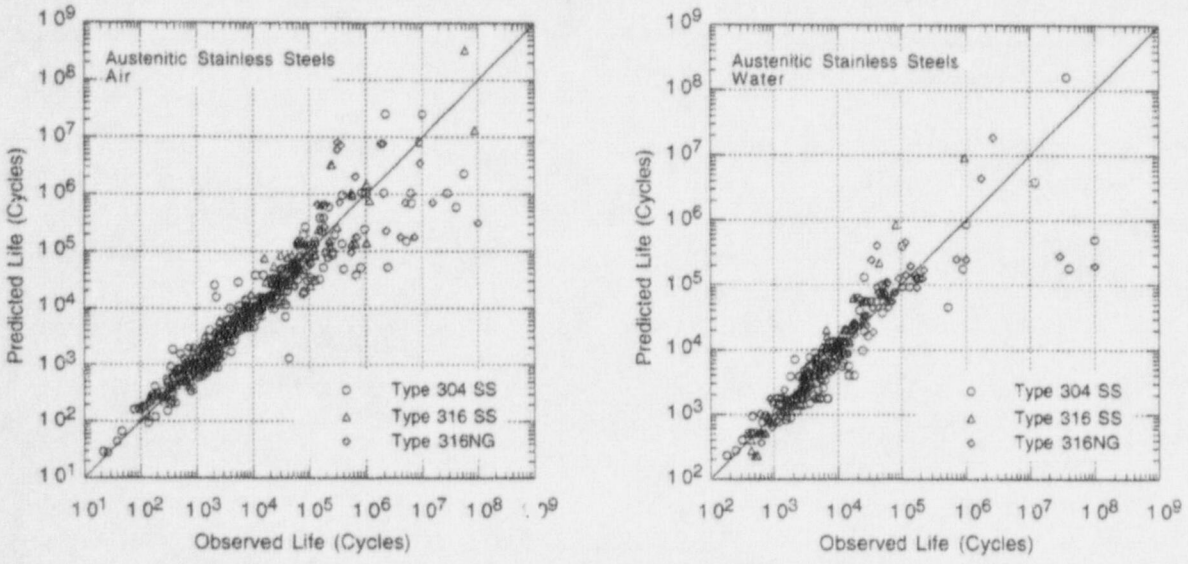

Figure 16. Experimental and predicted values of fatigue lives of austenitic SSs in air and water environments

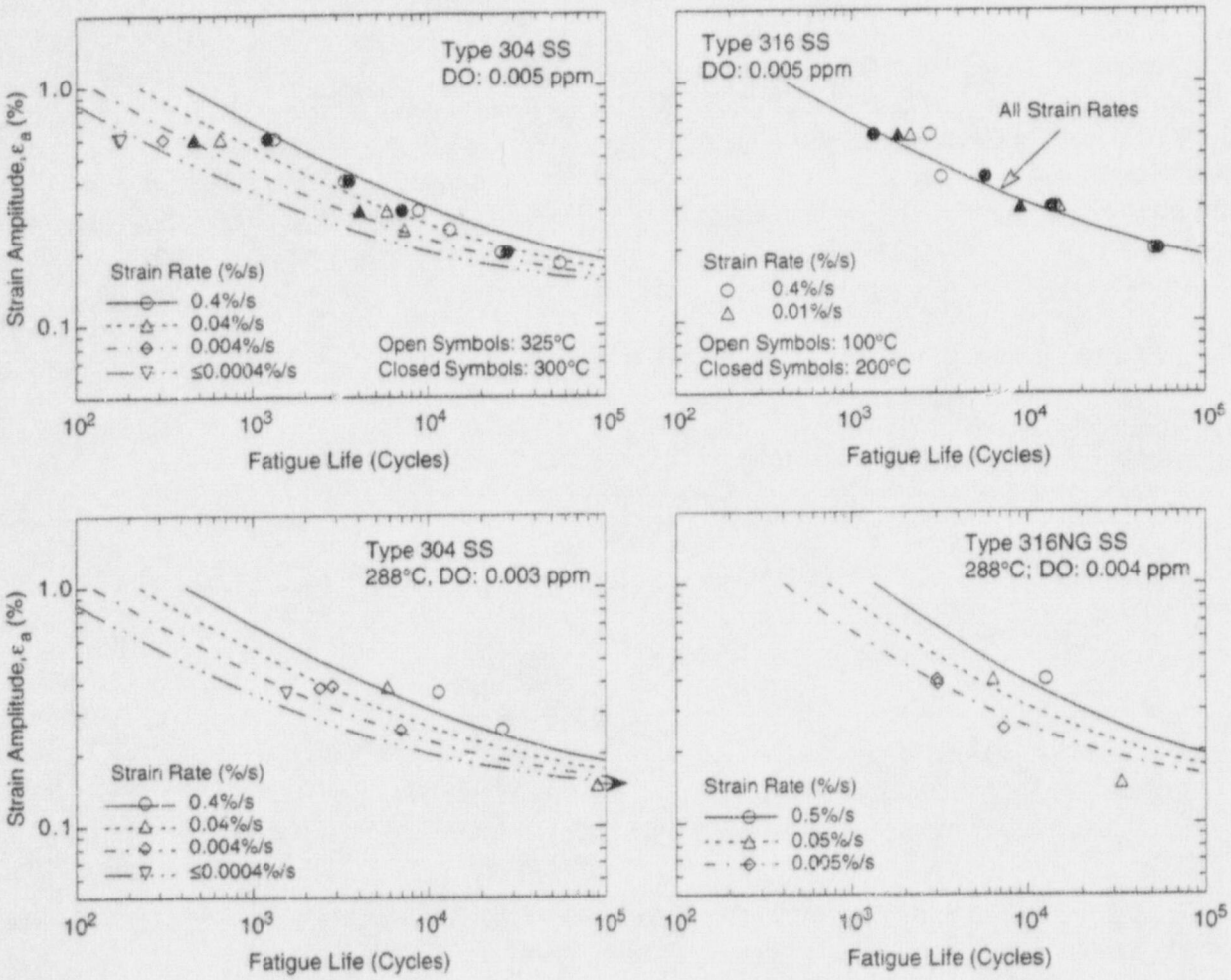

Figure 17. Experimental fatigue lives and S–N curves estimated from statistical models for austenitic SSs in water environments

the existing fatigue S–N data (Fig. 5). Also, as discussed above, although best-fit of the S–N data in LWR environments (Fig. 17) yields a steeper slope, the slope of the S–N curve in water was assumed to be the same as in air.

Upon completion of the modeling phase, the residual errors (i.e., the Cartesian distance from the prediction curve) should not show significant patterns such as heteroskedasticity (changing variance), or a non-zero slope. The residual errors for each variable, grouped by steel type and environment (air or water), are plotted in Figs. 18–22. Most data subsets and plots do not show patterns. In general, high variance tends to be associated with longer lives and lower strain amplitudes. Furthermore, biases seem to be traceable to heat-to-heat variation.

2.6 Design Fatigue Curves

The current ASME Section III Code design fatigue curves were based on experimental data on small polished test specimens. The design fatigue curves were obtained by adjusting the

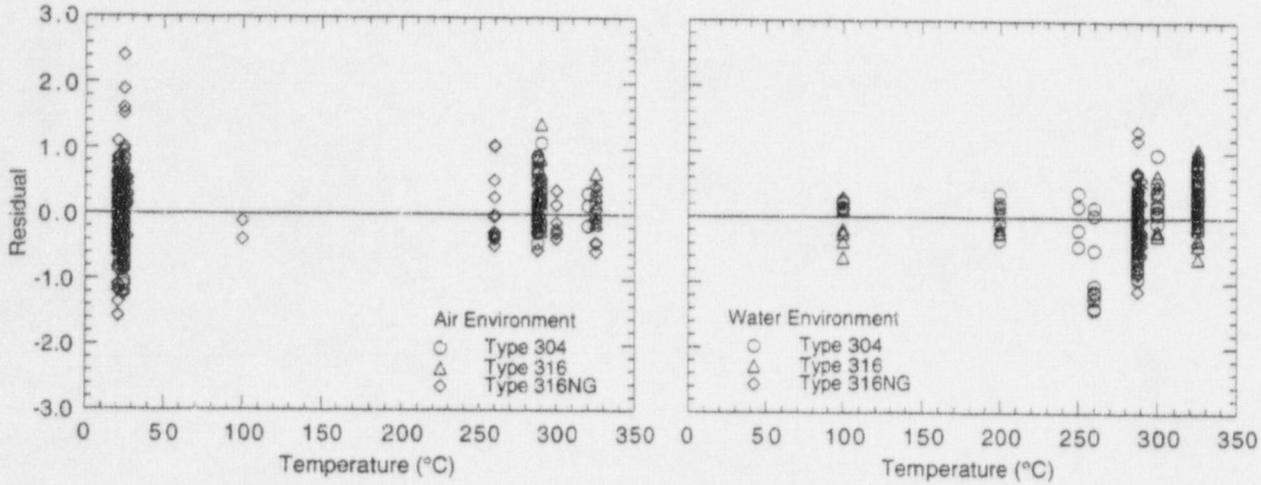

Figure 18. Residual error for austenitic SSs as function of test temperature

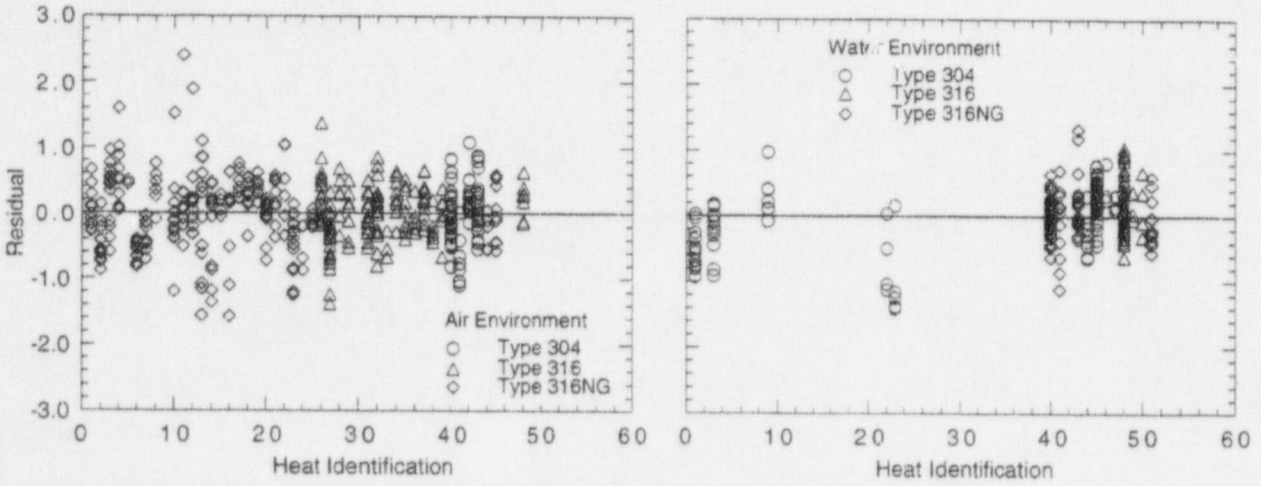

Figure 19. Residual error for austenitic SSs as function of material heat

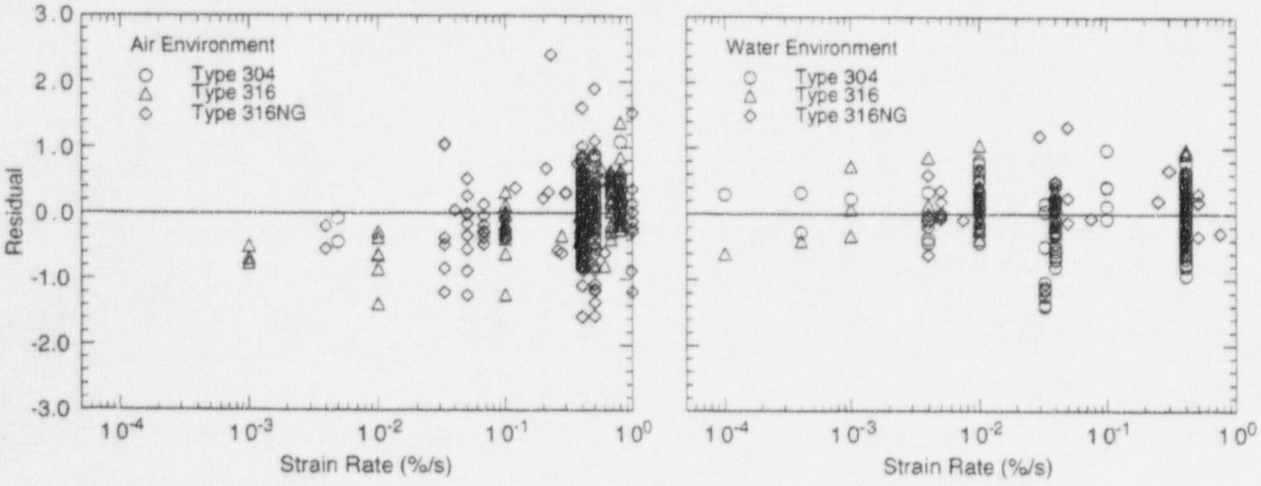

Figure 20. Residual error for austenitic SSs as function of loading strain rate

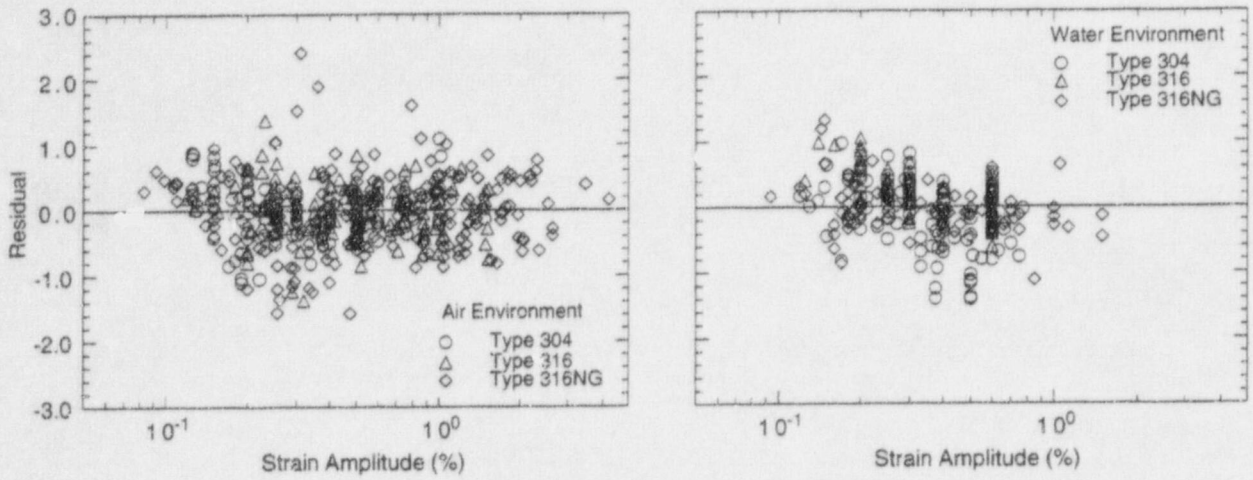

Figure 21. Residual error for austenitic SSs as function of applied strain amplitude

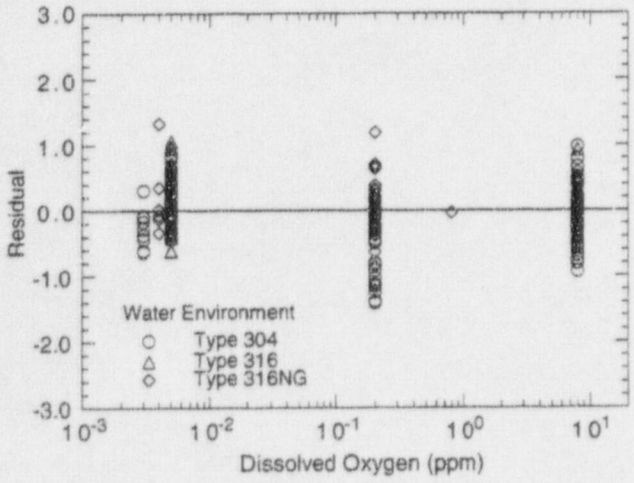

Figure 22. Residual error for austenitic SSs as function of DO in water

best-fit curve for the effect of mean stress and then lowering the adjusted curve by a factor of 2 on stress or 20 on life, whichever is more conservative, at each point of the curve. The best-fit curve to the experimental data,[35] expressed in terms of strain amplitude ε_a (%) and fatigue cycles N, for austenitic SSs is given by

$$\ln[N] = 6.954 - 2.0 \ln(\varepsilon_a - 0.167). \quad (6)$$

The mean curve, expressed in terms of stress amplitude S_a (MPa), which is the product of ε_a and elastic modulus E, is given by

$$S_a = 58020/\sqrt{N} + 299.92. \quad (7)$$

The room-temperature value of 195.1 GPa (28300 ksi) for the elastic modulus was used in converting the experimental strain-versus-life data to stress-versus-life curves. The best-fit curves were adjusted for the effect of mean stress by using the modified Goodman relation[35]

$$S_a' = S_a\left(\frac{\sigma_u - \sigma_y}{\sigma_u - S_a}\right) \text{ for } S_a < \sigma_y, \quad (8a)$$

and

$$S'_a = S_a \qquad \text{for } S_a > \sigma_y, \tag{8b}$$

where S'_a is the adjusted value of stress amplitude, and σ_y and σ_u are yield and ultimate strengths of the material, respectively. The Goodman relation assumes the maximum possible mean stress and typically gives a conservative adjustment for mean stress, at least when environmental effects are not significant. The design fatigue curves were then obtained by lowering the adjusted best-fit curve by a factor of 2 on stress or 20 on cycles, whichever was more conservative, to account for differences and uncertainties in fatigue life associated with material and loading conditions.

The same procedure has been used to develop design fatigue curves for LWR environments. However, because of the differences between the ASME mean curve and the best-fit curve to existing fatigue data (Fig. 5), the margin on strain for the current ASME Code design fatigue curve is closer to 1.5 than 2. Therefore, to be consistent with the current Code design curve, a factor of 1.5 rather than 2 was used in developing the design fatigue curves from the updated statistical models in air and LWR environments.

The design fatigue curves based on the statistical model for Types 304 and 316 SS in air and low- and high-DO water are shown in Figs. 23–25. A similar set of curves can be obtained from Eqs. 1b and 3b for Type 316NG SS. Because the fatigue life of Type 316NG is superior to that of Types 304 or 316 SS, Figs. 23–25 may be used conservatively for Type 316NG SS. In air, although the differences at low stress levels between the current ASME Code design curve and the design curve obtained from the updated statistical model at temperatures < 250°C have been reduced or eliminated by reducing the margin on stress from 2 to 1.5, significant differences still exist between the two curves. For example, at stress amplitudes > 300 MPa, estimates of life from the updated design curve are a factor of ≈2 lower than those from the ASME Code curve. Therefore, the actual margins on stress and life for the current ASME Code design fatigue curve are 1.5 and 10, respectively, instead of 2 and 20. Also, because of strain rate effects at temperatures > 250°C, estimated fatigue lives may be further reduced up to a factor of ≈3.5 at very slow strain rates.

As discussed above, the existing fatigue data indicate a threshold strain range of ≈0.32%, below which environmental effects on fatigue lives of austenitic SSs either do not occur or are insignificant. This value must be adjusted for the effects of mean stress and uncertainties due to material and loading variability. Threshold strain amplitudes are decreased by ≈10% to account for mean stress effects and by a factor of 1.5 to account for uncertainties in fatigue life associated with material and loading variability. Thus, a threshold strain amplitude of 0.097% (stress amplitude of 189 MPa) was selected, below which environmental effects on life are modest and are represented by the design curve for temperatures < 200°C (shown by the solid line in Figs. 24 and 25).

These curves can be used to perform ASME Code fatigue evaluations for components for service in LWR environments. For each set of load pair, a partial usage factor is obtained from the appropriate design fatigue curve. Information regarding the service conditions, such as temperature, strain rate, and DO level, are required for the evaluations. The procedure for obtaining these parameters depends on the details of the available information, i.e., whether the elapsed time versus temperature information for the transient is available. The maximum

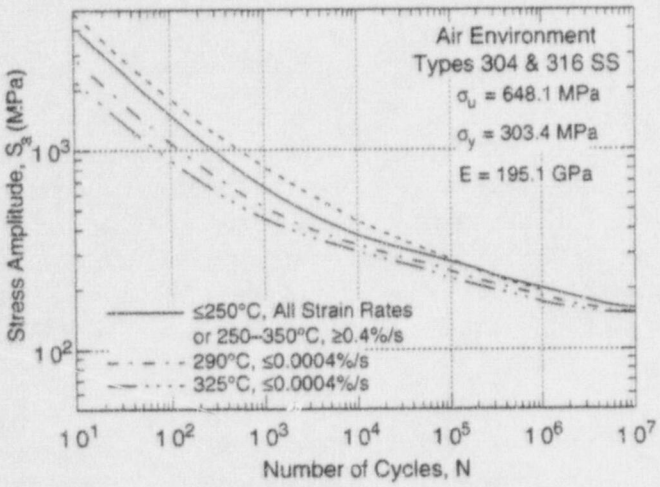

Figure 23.
Design fatigue curves for Types 304 and 316 SS in air

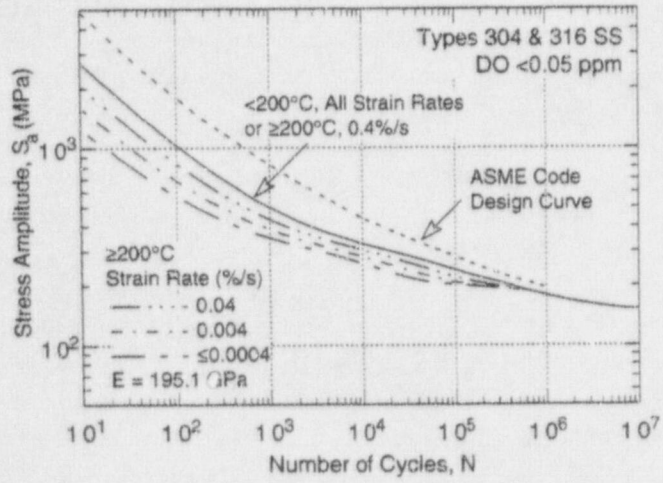

Figure 24.
Design fatigue curves for Types 304 and 316 SS in water with <0.05 ppm DO

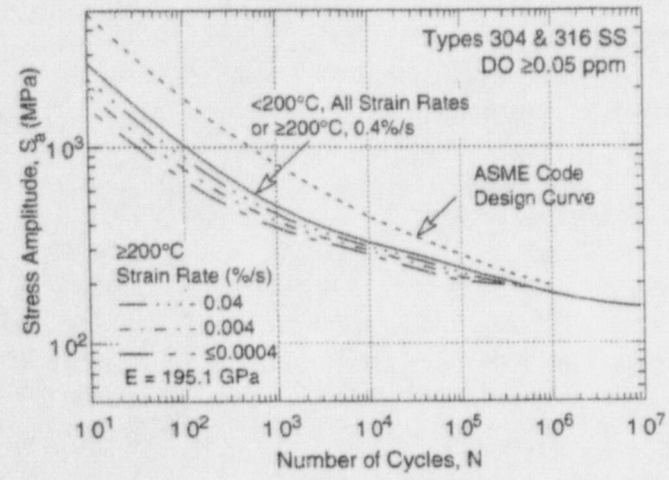

Figure 25.
Design fatigue curves for Types 304 and 316 SS in water with ≥0.05 ppm DO

values of temperature and DO level and the slowest strain rate during the transient may be used for a conservative estimate of life. Note that the design curves in LWR environments not only account for environmental effects on life but also include the difference between the current Code design curve and the updated design curve in air, i.e., the difference between the solid and dashed curves in Fig. 23.

2.7 Fatigue Life Correction Factor

The effects of reactor coolant environments on fatigue life have also been expressed in terms of a fatigue life correction factor F_{en}, which is the ratio of the life in air at room temperature to that in water at the service temperature.[6,36,37] To incorporate environmental effects into the ASME Code fatigue evaluation, a fatigue usage for a specific load pair based on the current Code fatigue design curve is multiplied by the correction factor. A fatigue life correction factor F_{en} can also be obtained from the statistical model, where

$$\ln(F_{en}) = \ln(N_{air}) - \ln(N_{water}). \tag{9}$$

From Eqs. 1a and 2a, the fatigue life correction factor relative to room-temperature air for Types 304 and 316 SSs is given by

$$F_{en} = \exp(0.935 - T^* \dot{\varepsilon}^* O^*), \tag{10}$$

where the threshold and saturation values for T^*, $\dot{\varepsilon}^*$, and O^* are defined in Eqs. 5a–5c. At temperatures ≥ 200°C and strain rates ≤ 0.0004%/s, Eq. 10 yields an F_{en} of ≈15 in low-DO PWR water (< 0.05 ppm DO) and ≈8 in high-DO water (≥ 0.05 ppm DO). At temperatures < 200°C, F_{en} is ≈2.5 in both low- and high-DO water at all strain rates.

3 Irradiation-Assisted Stress Corrosion Cracking of Austenitic SS

In recent years, failures of reactor-core internal components have increased after accumulation of fluence >0.5 x 10^{21} n·cm^{-2} (E >1 MeV) or ≈0.7 displacements per atom (dpa) in BWRs and at approximately one order of magnitude higher fluences in some PWR components. The general pattern of the observed failures indicates that, as nuclear plants age and neutron fluence increases, various nonsensitized austenitic SSs become susceptible to intergranular (IG) failure. Some components are known to have cracked under minimal applied stress. Although most failed components can be replaced, some safety-significant structural components (e.g., BWR top guide, shroud, and core plate) would be very difficult or impractical to replace. Therefore, the structural integrity of these components after accumulation of high fluence has been a subject of concern and extensive research has been conducted to provide an understanding of this type of degradation, which is commonly known as IASCC.

Irradiation produces profound effects both on local coolant water chemistry and component microstructure. Primary material effects of irradiation include alteration of local microchemistry, microstructure, and mechanical properties of the core internal components, usually fabricated from ASTM Type 304, 316, or 348 SSs. Irradiation produces defects and defect clusters in grain matrices and alters the dislocation and dislocation loop structures, leading to radiation-induced hardening, and in many cases, flow localization via dislocation channeling. Irradiation also leads to changes in the stability of second-phase precipitates and the local alloy chemistry near grain boundaries, precipitates, and defect clusters. Grain-boundary microchemistry that differs significantly from that of the bulk composition can be produced in association with not only radiation-induced segregation (RIS) but also thermally driven equilibrium and nonequilibrium segregation of alloying and impurity elements.

Irradiation-induced grain-boundary depletion of chromium has been considered for many years as the primary metallurgical process that causes IASCC, at least up to ≈5 x 10^{21} n·cm^{-2} (E >1 MeV) or ≈7 dpa. One of the most important factors that has been considered by many investigators to support the grain-boundary chromium-depletion mechanism is the observation that the dependence on water chemistry (i.e., oxidizing potential) of IGSCC of nonirradiated thermally sensitized material and of IASCC of irradiated solution-annealed material is very similar. However, as fluence level increases further, cracking in water has been observed at not only high but also low electrochemical potential (ECP) environments, such as in PWRs or BWRs that employ a hydrogen water chemistry (HWC). These observations are difficult to explain on the basis of a mechanism in which grain-boundary chromium depletion plays a primary role. Furthermore, strong heat-to-heat variation is very common in susceptibility to IASCC even among the same type, grade, and heats of SSs of nominally similar elemental composition.

In the present reporting period, our effort has focused on SSRT testing of model SS alloys irradiated in the Halden reactor and an analysis of cracked Types 304L and 304 SS BWR core shrouds to obtain a better understanding of the cracking mechanism(s).

3.1 Slow-Strain-Rate-Tensile Tests of Model Austenitic Stainless Steels Irradiated in Halden Reactor

(H. M. Chung, W. E. Ruther, and R. V. Strain)

The compositions of 27 model austenitic stainless steel alloys are given in Table 5. Slow-strain-rate-tensile tests and fractographic analysis by SEM have been completed for 16 alloys that were irradiated to a fluence of ≈0.3 x 10^{21} n·cm^{-2} (E > 1 MeV) at ≈288°C in a helium environment in the Halden heavy-water boiling reactor. Several tests were also conducted on alloys irradiated to ≈0.9 x 10^{21} n·cm^{-2} (E > 1 MeV). In addition to irradiated alloy specimens, nonirradiated control specimens were also tested under the same condition. All SSRT tests were conducted at a strain rate of 1.65 x 10^{-7} s^{-1} in simulated BWR water containing ≈8 ppm DO at 288°C. Electrochemical potential of SS was measured at the effluent from the autoclave at regular intervals.

Tables 6-8 show results from SSRT tests on nonirradiated control specimens and specimens irradiated to ≈0.3 x 10^{21} and ≈0.9 x 10^{21} n·cm^{-2} (E > 1 MeV), respectively. The tables also give results of SEM fractographic analysis of the specimens. In Tables 9 and 10, the SSRT test results (viz., uniform and total plastic strains and maximum stress) and SEM fractographic analysis (i.e., percent IGSCC and TGSCC, and the combined values) are correlated with the composition of nonirradiated and irradiated alloys, respectively.

The 0.2%-offset yield strengths and total elongations of nonirradiated control specimens of model austenitic SSs in water that contains ≈8 ppm DO at 289°C are shown in Figs. 26 and 27, respectively. The yield strengths of heats of nonirradiated solution-annealed Type 304 SS ranged 170-240 MPa, whereas the yield strengths of heats of Type 316 and 348 SS was significantly higher (280-350 MPa). Total elongation measured in water for most nonirradiated specimens was in the range of 17-59%, as shown in Fig. 27. However, heat-to-heat variation was significant among the same type of steels. In particular, three alloys exhibited unusually low ductility, namely, Type 304 SS Heat L7 (high oxygen concentration of ≈274 wppm), Heat L2 (high manganese and sulfur contents), and high-purity Type 348 SS Heat L24 that contains

Table 5. Composition of 27 commercial and laboratory model austenitic SSs irradiated in Halden reactor

ANL ID[a]	Source Heat ID	Composition (wt.%)										
		Ni	Si	P	S	Mn	C	N	Cr	O	B	Mo or Nb
C1	DAN-70378	8.12	0.50	0.038	0.002	1.00	0.060	0.060	18.11	-	<0.001	-
L2	BPC-4-111	10.50	0.82	0.080	0.034	1.58	0.074	0.102	17.02	0.0066	<0.001	-
C3	PNL-C-1	8.91	0.46	0.019	0.004	1.81	0.016	0.083	18.55	-	<0.001	-
L4	BPC-4-88	10.20	0.94	0.031	0.010	1.75	0.110	0.002	15.80	-	<0.001	-
L5	BPC-4-104	9.66	0.90	0.113	0.028	0.47	0.006	0.033	21.00	-	<0.001	-
L6	BPC-4-127	10.00	1.90	0.020	0.005	1.13	0.096	0.087	17.10	0.0058	<0.001	-
L7	BPC-4-112	10.60	0.18	0.040	0.038	1.02	0.007	0.111	15.40	0.0274	<0.001	-
L8	BPC-4-91	10.20	0.15	0.093	0.010	1.85	0.041	0.001	18.30	-	<0.001	-
C9	PNL-C-6	8.75	0.39	0.013	0.013	1.72	0.062	0.065	18.48	-	<0.001	-
C10	DAN-23381	8.13	0.55	0.033	0.002	1.00	0.060	0.086	18.19	-	<0.001	-
L11	BPC-4-93	8.15	0.47	0.097	0.009	1.02	0.014	0.004	17.40	-	<0.001	-
C12	DAN-23805	8.23	0.47	0.018	0.002	1.00	0.060	0.070	18.43	-	<0.001	-
L13	BPC-4-96	8.18	1.18	0.027	0.022	0.36	0.026	0.001	17.40	-	<0.001	-
L14	BPC-4-129	7.93	1.49	0.080	0.002	1.76	0.107	0.028	15.00	0.0045	<0.001	-
L15	BPC-4-126	8.00	1.82	0.010	0.013	1.07	0.020	0.085	17.80	0.0110	<0.001	-
C16	PNL-SS-14	12.90	0.38	0.014	0.002	1.66	0.020	0.011	16.92	-	<0.001	-
L17	BPC-4-128	8.00	0.66	0.090	0.009	0.48	0.061	0.078	15.30	0.0090	<0.001	-
L18	BPC-4-98	8.13	0.14	0.016	0.033	1.13	0.080	0.001	18.00	-	<0.001	-
C19	DAN-74827	8.08	0.45	0.031	0.003	0.99	0.060	0.070	18.21	-	<0.001	-
L20	BPC-4-101	8.91	0.17	0.010	0.004	0.41	0.002	0.002	18.10	-	<0.001	-
C21[b]	DAN-12455	10.24	0.51	0.034	0.001	1.19	0.060	0.020	16.28	-	<0.001	Mo 2.08
L22[c]	BPC-4-100	13.30	0.24	0.015	0.004	0.40	0.003	0.001	16.10	-	<0.001	Mo 2.04
L23[d]	BPC-4-114	12.04	0.68	0.030	0.047	0.96	0.043	0.092	17.30	0.0093	<0.001	Nb 1.06
L24[e]	BPC-4-105	12.30	0.03	0.007	0.005	0.48	0.031	0.002	16.90	-	<0.001	Nb 1.72
L25,C3	BPC-4-133	8.93	0.92	0.020	0.008	1.54	0.019	0.095	17.20	0.0085	0.010	-
L26,C19	BPC-4-131	8.09	0.79	0.004	0.002	0.91	0.070	0.089	17.20	0.0080	<0.001	-
L27,C21	BPC-4-132	10.30	0.96	0.040	0.002	0.97	0.057	0.019	15.30	-	0.030	Mo 2.01

[a]First letters "C" and "L" denote commercial and laboratory heats, respectively.
[b]Commercial-purity Type 316 SS.
[c]High-purity Type 316 SS.
[d]Commercial-purity Type 348 SS.
[e]High-purity Type 348 SS.

an unusually low concentration of silicon of ≈0.03 wt.%. As shown in Fig. 28, Heat L7 of Type 304 SS with high-oxygen content exhibited a large effect in water even in the nonirradiated condition. This observation is at least qualitatively consistent with a trend reported previously that higher oxygen concentration is conducive to higher susceptibility to IGSCC in irradiated steels, namely, for Type 304 SS BWR neutron-absorber tubes and control-blade sheath irradiated to a fluence of ≈2 x 10^{21} n·cm^{-2} (E > 1 MeV)[38] and for proton-irradiated Type 304L specimens at 400°C and tested at 288°C.[39] The result in Fig. 28 also is qualitatively consistent with a previous report in which oxygen contamination was a major factor in SCC of BWR core shroud welds.[40]

The yield and maximum strengths and uniform and total elongations of five commercial heats of Type 304 SS in simulated BWR water that contains ≈8 ppm DO are plotted in Fig. 29 both before and after irradiation to a fluence of ≈0.3 x 10^{-21} n·cm^{-2} (E > 1 MeV). Similar results for a specimen of Type 304 SS from a BWR control-blade sheath, irradiated in BWR-L

Table 6. Results of SSRT[a] tests and SEM fractography for nonirradiated control specimens of model SS alloys

Alloy Ident. No.	Fast-Neutron Fluence ($n \cdot cm^{-2}$)	SSRT No.	Feedwater Chemistry: Oxygen Conc. (ppm)	Feedwater Chemistry: Average ECP (mV SHE)	Feedwater Chemistry: Cond. at 25°C ($\mu S \cdot cm^{-1}$)	Feedwater Chemistry: pH at 25°C	SSRT Parameters: Yield Stress (MPa)	SSRT Parameters: Max. Stress (MPa)	SSRT Parameters: Uniform Elong. (%)	SSRT Parameters: Total Elong. (%)	Fracture Behavior: TGSCC (%)	Fracture Behavior: IGSCC (%)	Fracture Behavior: TG + IG SCC (%)
L23	0	CHR-1	8.6	+228	0.07	6.65	332	480	15.6	17.0	15	0	15
L7	0	CHR-2	8.0	+217	0.07	7.37	195	370	2.5	5.2	20	0	20
L7	0	CHR-7		Tested in Air			287	676	42.3	43.9	0	0	0
L14	0	CHR-3	8.6	+208	0.07	7.37	240	474	41.8	44.2	0	0	0
L17	0	CHR-4	7.5	+262	0.06	7.09	139	412	11.6	13.3	60	0	60
L6	0	CHR-5	7.9	+256	0.08	6.85	227	545	43.0	44.5	0	0	0
L27	0	CHR-6	9.3	+247	0.08	6.96	298	483	20.6	22.9	0	0	0
L26	0	CHR-8	9.4	+223	0.07	6.65	184	596	38.2	40.2	0	0	0
L2	0	CHR-9	8.6	+292	0.06	6.55	193	348	6.6	7.8	57	0	57
L25	0	CHR-10	8.2	+239	0.06	6.42	184	458	25.5	27.0	0	0	0
L15	0	CHR-11	8.2	+195	0.06	6.32	218	512	36.7	37.9	0	0	0
L24	0	CHR-12	8.4	+200	0.07	6.20	352	461	10.4	12.3	10	0	10
C1	0	CHR-13	8.1	+187	0.07	6.33	179	498	49.4	51.7	0	0	0
C19	0	CHR-14	8.8	+179	0.08	6.29	178	501	47.4	49.2	0	0	0
C9	0	CHR-15	8.5	+166	0.07	6.83	178	408	17.4	19.4	32	0	32
C12	0	CHR-16	8.5	+124	0.07	6.18	182	511	46.0	47.6	0	0	0
C10	0	CHR-17	9.2	+145	0.07	6.26	174	478	30.6	35.1	0	0	0
C21	0	CHR-18	9.2	+187	0.07	6.41	277	455	48.9	59.5	0	0	0

[a]Tested at 289°C at a strain rate of $1.65 \times 10^{-7}\ s^{-1}$ in BWR-simulated water containing ~8 ppm DO.

Table 7. Results of SSRT[a] tests and SEM fractography for model austenitic SSs irradiated in helium at 288°C to fluence of ≈0.3 :. 10^{21} n·cm^{-2} (E > 1 MeV)

Alloy Ident. No.	Fast-Neutron Fluence (n·cm^{-2})	SSRT No.	Feedwater Chemistry: Oxygen Conc. (ppm)	Feedwater Chemistry: Average ECP (mV SHE)	Feedwater Chemistry: Cond. at 25°C (μS·cm^{-1})	Feedwater Chemistry: pH at 25°C	SSRT Parameters: Yield Stress (MPa)	SSRT Parameters: Max. Stress (MPa)	SSRT Parameters: Uniform Elongation (%)	SSRT Parameters: Total Elongation (%)	Fracture Behavior: TGSCC (%)	Fracture Behavior: IGSCC (%)	Fracture Behavior: TG + IG SCC (%)
C1	0.45 x 10^{21}	HR-1	8.3	+184	0.07	7.03	490	680	13.4	16.6	4	0	4
L5	0.45 x 10^{21}	HR-2	9.7	+208	0.07	6.89	513	539	29.5	32.7	2	2	4
L22	0.45 x 10^{21}	HR-3	8.0	+236	0.07	6.80	360	596	6.6	9.4	50	15	65
C3	0.45 x 10^{21}	HR-4	8.7	+161	0.07	6.68	338	491	27.7	31.6	5	0	5
C16	0.45 x 10^{21}	HR-5	8.3	+204	0.08	6.74	370	527	17.6	20.6	2	0	2
L4	0.45 x 10^{21}	HR-6	9.0	+202	0.08	6.70	367	542	19.7	22.3	46	0	46
L18	0.45 x 10^{21}	HR-7	9.0	+203	0.08	6.33	503	572	6.3	8.8	54	0	54
C10	0.45 x 10^{21}	HR-8	8.2	+174	0.07	6.35	523	640	17.4	18.9	6	0	6
C21	0.45 x 10^{21}	HR-9	8.1	+149	0.08	6.49	480	620	15.9	19.4	4	0	4
L11	0.45 x 10^{21}	HR-10	9.0	+157	0.08	6.17	487	599	2.3	3.8	62	0	62
L13	0.45 x 10^{21}	HR-11	8.7	+164	0.08	6.17	248	461	22.1	24.8	8	0	8
L20	0.45 x 10^{21}	HR-12	8.4	+174	0.07	6.20	454	552	2.9	5.1	32	2	34
C19	0.45 x 10^{21}	HR-13	9.5	+132	0.12	6.36	554	682	10.5	14.7	7	0	7
C9	0.45 x 10^{21}	HR-14	8.0	+192	0.11	6.30	522	607	13.4	14.6	24	0	24
C12	0.45 x 10^{21}	HR-15	9.0	+195	0.08	6.40	404	589	20.4	24.2	5	0	5
L8	0.45 x 10^{21}	HR-16	9.0	+215	0.08	6.60	411	571	15.6	17.9	54	0	54

[a]Tested at 288°C at a strain rate of 1.65 x 10^{-7} s^{-1} in simulated BWR water that contains ≈8 ppm DO.

Table 8. Results of SSRT[a] tests and SEM fractography for model austenitic SSs irradiated in helium at 288°C to fluence of ≈0.9 x 10^{21} n·cm^{-2} (E > 1 MeV)

Alloy Ident. No.	Fast-Neutron Fluence (n·cm^{-2})	SSRT No.	Feedwater Chemistry: Oxygen Conc. (ppm)	Feedwater Chemistry: Average ECP (mV SHE)	Feedwater Chemistry: Cond. at 25°C (μS·cm^{-1})	Feedwater Chemistry: pH at 25°C	SSRT Parameters: Yield Stress (MPa)	SSRT Parameters: Max. Stress (MPa)	SSRT Parameters: Uniform Elongation (%)	SSRT Parameters: Total Elongation (%)	Fracture Behavior: TGSCC (%)	Fracture Behavior: IGSCC (%)	Fracture Behavior: TG + IGSCC (%)
L22	0.9 x 10^{21}	HR-17	8.0	+181	0.08	6.77	475	549	4.20	5.82	30	35	65
L11	0.9 x 10^{21}	HR-18	8.0	+191	0.08	6.55	820	856	0.43	1.65	50	14	64
L18	0.9 x 10^{21}	HR-19	8.0	+193	0.10	6.07	710	755	3.98	5.05	38	14	52
L20	0.9 x 10^{21}	HR-20	8.0	+225	0.07	6.75	515	574	1.85	3.66	-	-	-

[a]Tested at 288°C at a strain rate of 1.65 x 10^{-7} s^{-1} in simulated BWR water that contains ≈8 ppm DO.

Table 9. Correlation of results of SSRT tests and SEM fractography with composition (in wt.%) of nonirradiated control specimens of model SS alloys[a]

Alloy ID	Ni	Si	P	S	Mn	C	N	Cr	Mo/Nb	O (wppm)	Remark[a]	YS (MPa)	UTS (MPa)	UE (%)	TE (%)	TGSCC (%)	IGSCC (%)	TG+IGSCC (%)
L23	12.04	0.68	0.030	0.047	0.95	0.043	0.092	17.30	Nb 1.06	93	CP 348	332	580	15.6	17.0	15	0	15
L7	10.60	0.18	0.040	0.038	1.02	0.007	0.111	15.40	-	274	High N, O; Low Si, C	195	370	2.5	5.2	20	0	20
L14	7.93	1.49	0.080	0.002	1.76	0.107	0.028	15.00	-	45	High Si, P, C; Low S	240	585	41.8	44.2	0	0	0
L17	8.00	0.66	0.090	0.009	0.48	0.061	0.078	15.30	-	90	High P; Low S	189	412	11.6	13.3	60	0	60
L6	10.00	1.90	0.020	0.005	1.13	0.096	0.087	17.10	-	58	High Si, C, Cr; Low S	227	545	43.0	44.5	0	0	0
L27	10.30	0.96	0.040	0.002	0.97	0.057	0.019	15.30	Mo 2.01	-	CP 316 ; High B (0.030)	298	483	20.6	22.9	0	0	0
L26	8.09	0.79	0.004	0.002	0.91	0.070	0.089	17.20	-	80	Low P, S	184	596	38.2	40.2	0	0	0
L2	10.50	0.82	0.080	0.034	1.58	0.074	0.102	17.02	-	66	High P, S, Mn, N	193	348	6.6	7.8	57	0	57
L25	8.93	0.92	0.020	0.008	1.54	0.019	0.095	17.20	-	85	High B (0.010)	184	458	25.5	27.0	0	0	0
L15	8.00	1.82	0.010	0.013	1.07	0.020	0.085	17.80	-	110	High N; Low C	218	512	36.7	37.9	0	0	0
L24	12.30	0.03	0.007	0.005	0.48	0.031	0.002	16.90	Nb 1.72	-	HP 348; Low Si, N	352	461	10.4	12.3	10	0	10
C1	8.12	0.50	0.038	0.002	1.00	0.060	0.060	18.11	-	-	Low S, CP 304	179	498	49.4	51.7	0	0	0
C19	8.08	0.45	0.031	0.003	0.99	0.060	0.070	18.21	-	-	Low Si, S, CP 304	178	501	47.4	49.2	0	0	0
C9	8.75	0.39	0.013	0.013	1.72	0.062	0.065	18.48	-	-	Low Si, High Mn	178	408	17.4	19.4	32	0	32
C12	8.23	0.47	0.018	0.002	1.00	0.060	0.070	18.43	-	-	Low Si, S, P	182	511	46.0	47.6	0	0	0
C10	8.13	0.55	0.033	0.002	1.00	0.060	0.086	18.19	-	-	Low S, High N	174	478	30.6	35.1	0	0	0
C21	10.24	0.51	0.034	0.001	1.19	0.060	0.020	16.28	Mo 2.08	-	CP 316; Low B (0.001)	277	455	48.9	59.5	0	0	0

[a]HP = high purity, CP = commercial purity.

Table 10. Correlation of results of SSRT[a] tests and SEM fractography with composition (in wt.%) of irradiated model SS alloys[b]

Alloy ID	Ni	Si	P	S	Mn	C	N	Cr	Mo/Nb	Remark	Fluence (10^{20} cm^{-2})	YS (MPa)	UTS (MPa)	UE (%)	TE (%)	TGSCC (%)	IGSCC (%)	TG+IG (%)
C1	8.12	0.50	0.038	0.002	1.00	0.060	0.060	18.11	-	Low S, CP 304	3	490	680	13.4	16.6	4	0	4
L5	9.66	0.90	0.113	0.028	0.47	0.006	0.033	21.00	-	High P, Cr; Low C	3	513	539	29.5	32.7	2	2	4
L22	13.30	0.24	0.015	0.004	0.40	0.003	0.001	16.10	Mo 2.04	HP 316L; Low Si, N	3	360	596	6.6	9.4	50	15	65
											9	475	549	4.2	5.8	30	35	65
C3	8.91	0.46	0.019	0.004	1.81	0.016	0.083	18.55	-	CP 304L, Low Si	3	338	491	27.7	31.6	5	0	5
C16	12.90	0.38	0.014	0.002	1.66	0.020	0.011	16.92	-	High Ni; Low Si, S	3	370	527	17.6	20.6	2	0	2
L4	10.20	0.94	0.031	0.010	1.75	0.110	0.002	15.80	-	High Ni, Mn, C; Low N	3	367	542	19.7	22.3	38	0	38
L18	8.13	0.14	0.016	0.033	1.13	0.05	0.001	18.00	-	Low Si, N	3	503	572	6.3	8.8	54	0	54
											9	710	755	4.0	5.1	32	4	36
C10	8.13	0.55	0.033	0.002	1.00	0.060	0.086	18.19	-	Low S, CP 304	3	523	640	17.4	18.9	6	0	6
C21	10.24	0.51	0.034	0.001	1.19	0.060	0.020	16.28	Mo 2.08	CP 316	3	480	620	15.9	19.4	4	0	4
L11	8.15	0.47	0.097	0.009	1.02	0.014	0.004	17.40	-	High P; Low Si, C, S, N	3	487	599	2.3	3.8	62	0	62
											9	820	856	0.4	1.6	50	14	64
L13	8.18	1.18	0.027	0.022	0.36	0.026	0.001	17.40	-	High Si; Low Mn, C, N	3	248	461	22.1	24.8	8	0	8
L20	8.91	0.17	0.010	0.004	0.41	0.002	0.002	18.10	-	HP 304L; Low Si, N	3	454	552	2.9	5.1	32	2	34
											9	515	574	1.8	3.7	-	-	-
C19	8.08	0.45	0.031	0.003	0.99	0.060	0.070	18.21	-	Low Si, S	3	554	682	10.5	14.7	7	0	7
C9	8.75	0.39	0.013	0.013	1.72	0.062	0.065	18.48	-	Low Si; High Mn	3	522	607	13.4	14.6	24	0	24
C12	8.23	0.47	0.018	0.002	1.00	0.060	0.070	18.43	-	Low Si, P, S	3	404	589	20.4	24.2	5	0	5
L8	10.20	0.15	0.093	0.010	1.85	0.041	0.001	18.30	-	High Ni, P, Mn; Low Si, N	3	411	571	15.6	17.8	64	0	64

[a]Tested at 288°C at a strain rate of 1.65×10^{-7} s^{-1} in simulated water that contains ≈8 ppm DO.

[b]HP = high purity, CP = commercial purity.

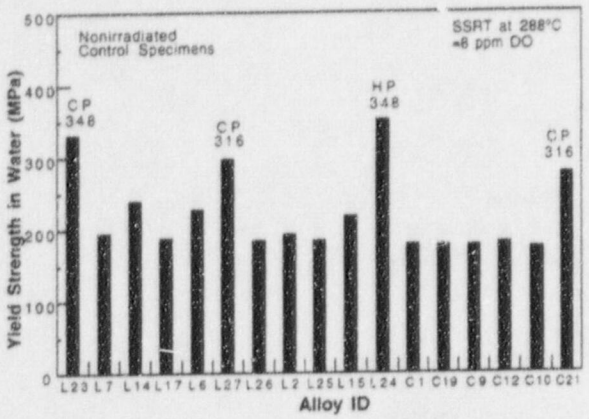

Figure 26.
Yield strength of nonirradiated control specimens of model SS alloys tested at 288°C in simulated BWR water that contains ≈8 ppm DO

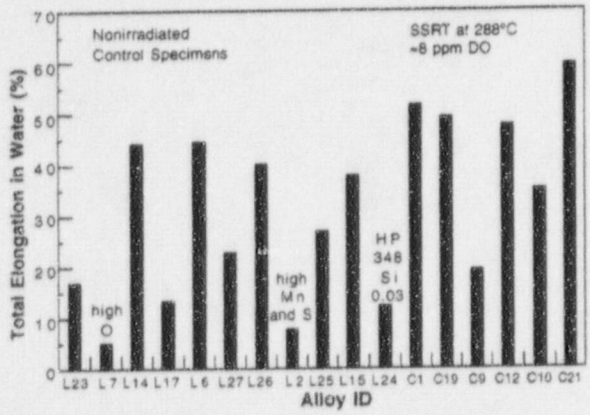

Figure 27.
Total elongation of nonirradiated control specimens of model SS alloys tested at 288°C in simulated BWR water that contains ≈ 8 ppm DO

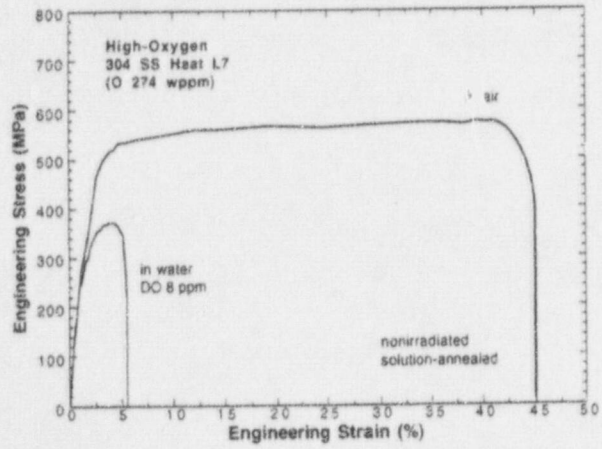

Figure 28.
Load versus elongation in air and simulated BWR water that contains ≈8 ppm DO at 288°C of nonirradiated Type 304 SS that contains unusually high concentration of oxygen (≈274 wppm)

to a fluence of ≈0.5 x 10^{-21} n·cm^{-2}, are also shown in the figure. The yield strengths of the solution-annealed materials after irradiation to ≈0.3 x 10^{-21} n·cm^{-2} (E > 1 MeV) increased from≈180 MPa to 400-600 MPa, whereas maximum strengths increased from 410-510 MPa to 600-680 MPa in test in 289°C water. Uniform and total elongations decreased from 17-49 to 10-20% and from 20-52 to 14-24%, respectively.

The effect of silicon content on irradiation-induced hardening, as manifested by the yield strengths of the alloys after irradiation to ≈0.3 x 10^{-21} n·cm^{-2} (E > 1 MeV), is interesting. In Table 11, the maximum strengths of 13 alloys tested in water with ≈8 ppm DO are correlated with the concentrations of silicon, carbon, and nitrogen. Only the alloys that contain unusually low concentrations of either silicon (<0.5 wt.%), carbon (<0.3 wt.%), or nitrogen

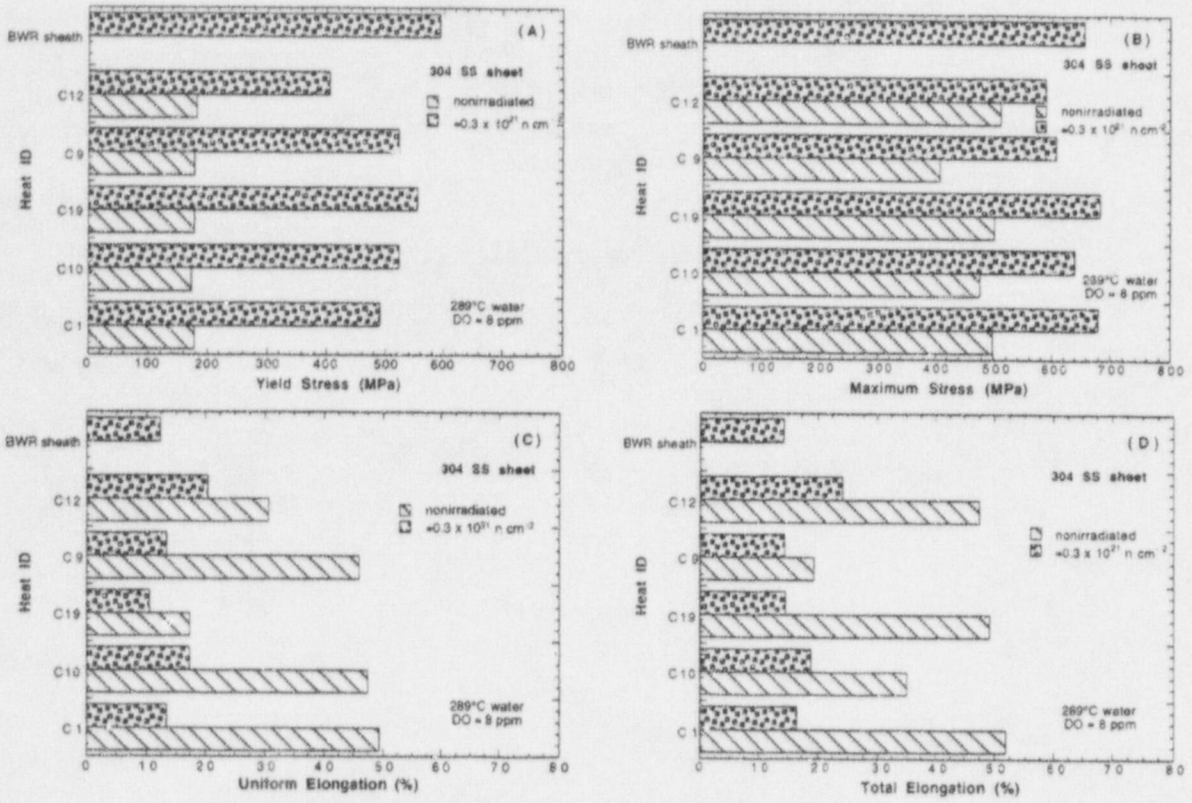

Figure 29. Slow-strain-rate tensile properties of commercial heats of Type 304 SS irradiated in helium in Halden reactor to a fluence of ≈0.3 x 10^{21} n·cm^{-2} (E > 1 MeV) and tested in simulated BWR water that contains ≈8 ppm DO at 288°C; (A) 0.2%-offset yield strength, (B) maximum stress, (C) uniform elongation, and (D) total elongation

(<0.005 wt.%) are listed in the table (low concentrations are denoted by bold type for the respective impurities). The other 3 alloys (i.e., commercial-grade Type 304 SSs, Heats C1 and C10, and Type 316 SS Heat C21) that contain high concentrations of silicon, carbon, and nitrogen were excluded from the table. Of the 13 alloys listed in the table, 3 alloys (Heats L22, L11, and L20) contain low concentrations of silicon, carbon, and nitrogen, and 1 alloy (Heat L13) contains low concentrations of carbon and nitrogen but a high concentration of silicon. Therefore, these 4 alloys were considered to be an ideal combination that can provide an information on the effect of silicon on irradiation-induced hardening. Interestingly, all 3 alloys that contain a low silicon concentration (0.17-0.47 wt.%) exhibited consistently higher degrees of irradiation-induced hardening than the alloy that contains a high silicon concentration of ≈1.18 wt.%. This is shown in Fig. 30. Consistent with this hardening behavior, the 3 alloys that contain a low concentration of silicon exhibit significantly lower ductility than the high-silicon alloy, i.e., 3.8-9.4 versus 24.8%. This is also shown in Fig. 30.

Miwa et al.[41] and Tsukada et al.[42] irradiated SSRT specimens of high-purity Type 304L SS (carbon, 0.003%; silicon, 0.01%; manganese, 1.36%; phosphorus, 0.001%; sulfur, 0.0014%; and nitrogen, 0.0014%), in which one alloy was doped with ≈0.69% silicon and the other without silicon addition, in helium at 240°C in the JRR-3 reactor to a fluence of ≈0.67 x 10^{-21} n·cm^{-2} (E > 1 MeV). Following SSRT tests at 300°C in water that contained ≈32 ppm

Table 11. Correlation of silicon, carbon, and nitrogen concentrations (in wt.%) with maximum strength and total elongation of model SS alloys irradiated to ≈0.3 x 10^{21} n·cm^{-2} (E > 1 MeV) in helium at 288°C and tested[a] at 288°C in simulated BWR water that contains ≈8 ppm DO

Alloy ID	Si	C	N	Remarks	Maximum Strength	Total Elongation
L5	0.90	**0.006**	0.033	High Si, Low C	539	32.7
L22	**0.24**	**0.003**	**0.001**	**Low Si, C, N**	**596**	**9.4**
C3	**0.46**	**0.016**	0.083	Low Si, C; High N	491	31.6
C16	**0.38**	**0.020**	0.011	Low Si, C	527	20.6
L4	0.94	0.110	**0.002**	High Si, C; Low N	542	22.3
L18	**0.14**	0.080	**0.001**	Low Si, N; High C	572	8.8
L11	**0.47**	**0.014**	**0.004**	**Low Si, C, N**	**599**	**3.8**
L13	1.18	**0.026**	**0.001**	**High Si; Low C, N**	**461**	**24.8**
L20	**0.17**	**0.002**	**0.002**	**Low Si, C, N**	**552**	**5.1**
C19	**0.45**	0.060	0.070	Low Si; High C, N	682	14.7
C9	**0.39**	0.062	0.065	Low Si; High C, N	607	14.6
C12	**0.47**	0.060	0.070	Low Si; High C, N	589	24.2
L8	**0.15**	0.041	**0.001**	Low Si, N	571	17.9

[a]Strain rate 1.65 x 10^{-7} s^{-1}.

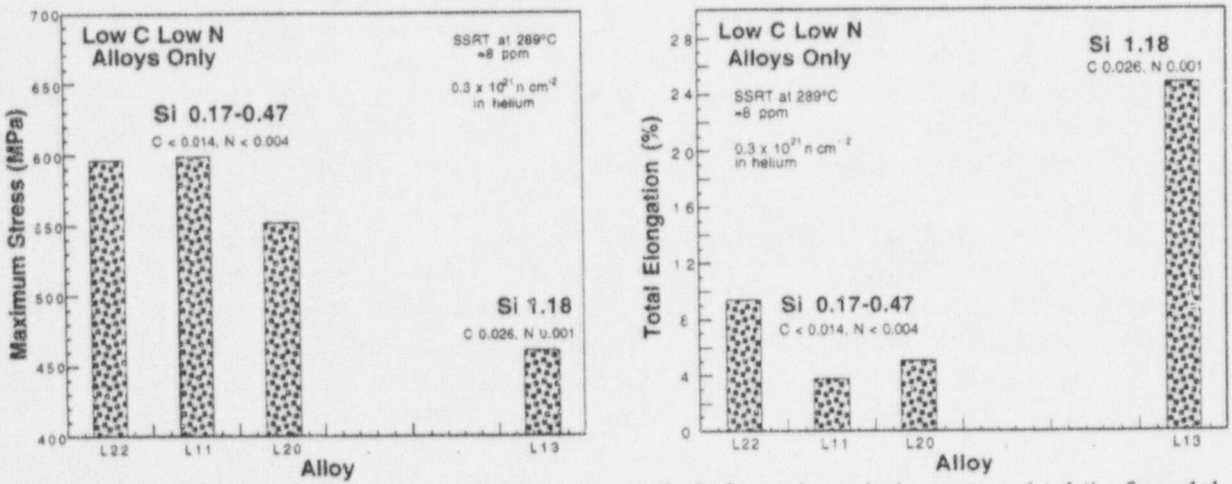

Figure 30. Effects of silicon on maximum strength (left) and total elongation (right) of model SS alloys that contain low carbon (<0.03 wt.%) and low nitrogen (<0.004%). Specimens were irradiated in helium at 288°C in Halden reactor to a fluence of ≈0.3 x 10^{21} n·cm^{-2} (E > 1 MeV) and tested at 288°C in simulated BWR water that contains ≈8 ppm DO.

DO, they observed that the high-silicon (0.69%) specimen exhibited significantly higher ductility than the low-silicon (0.01%) specimen, i.e., a total elongation of ≈21 versus 11%.[42] At the same time, they observed that the number density of Frank loops was significantly lower in the high-silicon specimen than in the low-silicon specimen, although the number density of small black-dot defect clusters appeared to be similar.[41] Because their SSRT test temperature was higher by ≈60°C than the irradiation temperature, some fraction of the defect clusters and loops probably annealed out during the test. Despite the uncertainty associated

with this, observations made in their investigations and in our study appear to be essentially consistent. This is, silicon atoms exert a profound effect on irradiation-induced hardening and irradiation-induced microstructural evolution in Types 304 and 304L SS.

Yield strength, maximum strength, uniform elongation, and total elongation for the specimens irradiated to ≈0.3 x 10^{21} n·cm^{-2} (E > 1 MeV) at 288°C in water that contains ≈8 ppm DO for each alloy are plotted in Figs. 31-34, respectively. Type 304 SS, Heat L13 that contains a high concentration of silicon (≈1.18%) and low concentrations of carbon (0.026%) and nitrogen (0.001%) exhibit unusually low yield and maximum strengths, as shown in Figs. 31 and 32, respectively, which indicates a softening effect of the high silicon concentration. From Figs. 33 and 34, respectively, it is evident that several alloys exhibit relatively low uniform and total elongations. The composition of the alloys, denoted in the figures, suggests that the concentrations of silicon, carbon, and nitrogen play important roles in irradiation-induced hardening. It appears that high concentrations of carbon and nitrogen are conducive to hardening with and without irradiation, whereas a high silicon concentration is conducive to more irradiation-induced hardening.

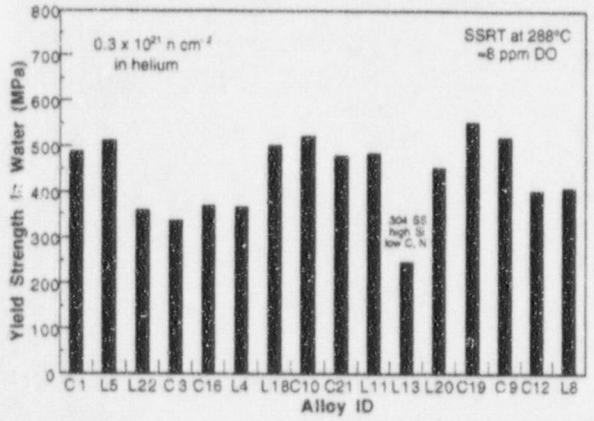

Figure 31.
Yield strength of model SS alloys irradiated in helium in Halden reactor to fluence of ≈0.3 x 10^{21} n·cm^{-2} (E > 1 MeV) and tested at 288°C in simulated BWR water that contains ≈8 ppm DO

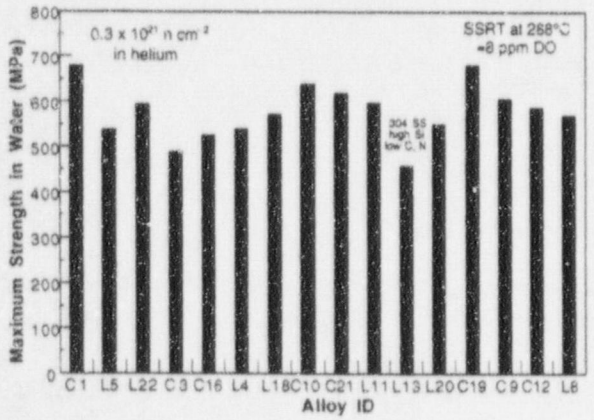

Figure 32.
Maximum strength of model SS alloys irradiated in helium in Halden reactor to fluence of ≈0.3 x 10^{21} n·cm^{-2} (E > 1 MeV) and tested at 288°C in simulated BWR water that contains ≈8 ppm DO

At a relatively low fluence of ≈0.3 x 10^{21} n·cm^{-2} (E > 1 MeV), susceptibility to IGSCC was insignificant except for high-purity heats of Type 304L and 316L SS (Fig. 35). Also, the threshold fluence for IASCC of the high-purity heats is lower than for commercial-grade heats. This observation is also consistent with results of a previous investigation which showed that at ≈2 x 10^{21} n·cm^{-2} (E > 1 MeV), BWR neutron-absorber tubes fabricated from high-purity heats of Type 304L SS were more susceptible to IASCC than neutron-absorber tubes and a control-blade sheath fabricated from commercial heats of Type 304 SS.[38]

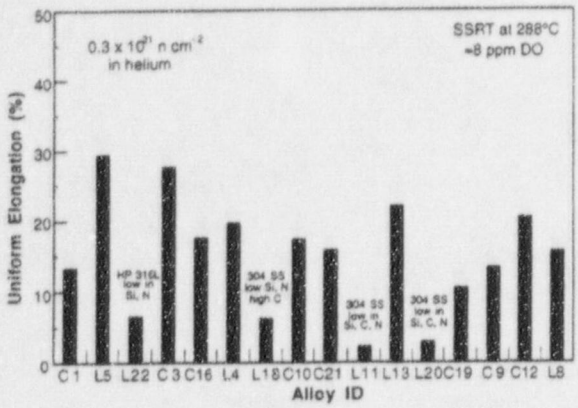

Figure 33.
Uniform elongation of model SS alloys irradiated in helium in Halden reactor to fluence of ≈0.3 x 10^{21} n·cm^{-2} (E > 1 MeV) and tested at 288°C in simulated BWR water that contains ≈8 ppm DO

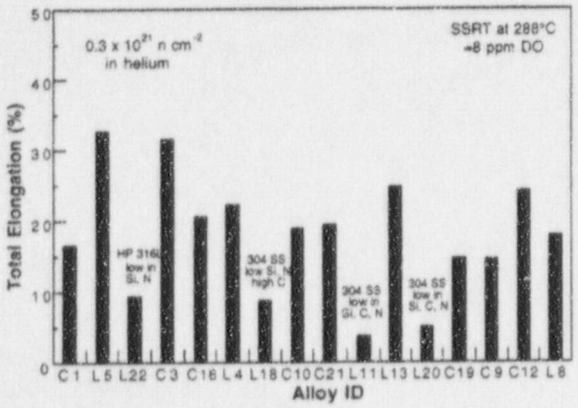

Figure 34.
Total elongation of model SS alloys irradiated in helium in Halden reactor to fluence of ≈0.3 x 10^{21} n·cm^{-2} (E > 1 MeV) and tested at 288°C in simulated BWR water that contains ≈8 ppm DO

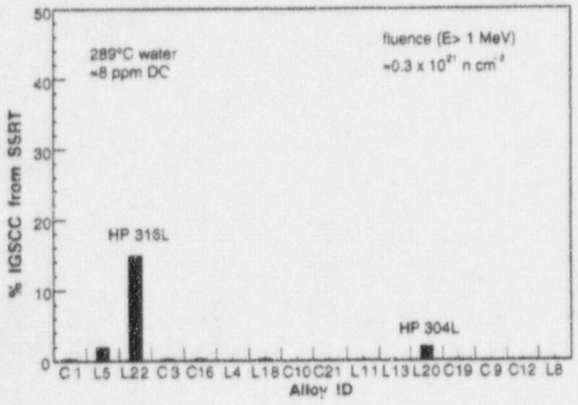

Figure 35.
Percent IGSCC of model SS alloys irradiated in helium in Halden reactor to fluence of ≈0.3 x 10^{21} n·cm^{-2} (E > 1 MeV) and tested at 288°C in simulated BWR water that contains ≈8 ppm DO

In contrast to IGSCC, susceptibility to TGSCC was significant for 7 of the 16 alloys at this low fluence (Fig. 36). Compositional characteristics of the 7 alloys and an alloy with low susceptibility denoted in the figure, also indicate that silicon and nitrogen play a role in TGSCC. Susceptibilities of all 16 alloys to IASCC at 0.3 x 10^{21} n·cm^{-2} (E > 1 MeV), measured in terms of combined percent IGSCC and percent TGSCC, are summarized in Fig. 37. The susceptibilities at this low fluence could be correlated best in terms of nitrogen and silicon concentrations. That is, all alloys that contain <50 wppm nitrogen and <1.0 wt.% silicon were susceptible, whereas all alloys that contain >50 wppm nitrogen or >1.0 wt.% silicon were relatively resistant. This result indicates that to reduce the susceptibility to IASCC, the concentrations of nitrogen and silicon should be >100 wppm and >1.0 wt.%, respectively. Because most commercial heats of Types 304 or 304L SS contain >100 wppm nitrogen, one should assess whether the silicon concentration is >1 wt.% in order to delay onset of and increase resistance to IASCC.

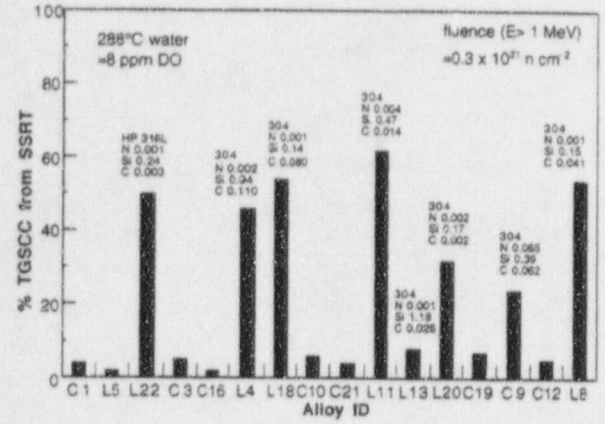

Figure 36.
Percent TGSCC of model SS alloys irradiated in helium in Halden reactor to fluence of ≈0.3 x 10^{21} n·cm^{-2} (E > 1 MeV) and tested at 288°C in simulated BWR water that contains ≈8 ppm DO

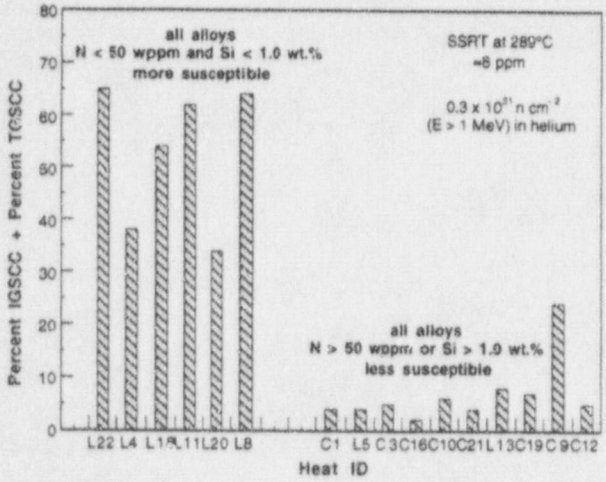

Figure 37.
Susceptibility to IGSCC and TGSCC of model SS alloys, irradiated in helium in Halden reactor to fluence of ≈0.3 x 10^{21} n·cm^{-2} (E > 1 MeV) and tested at 288°C in simulated BWR water, classified as a function of nitrogen and silicon contents of alloys

Previous experience suggests that susceptibility to IASCC is characterized by high susceptibility to TGSCC at low fluence, followed by transition from TGSCC to IGSCC as fluence increases. However, whether the same alloys that contain >50 wppm nitrogen or >1.0 wt.% silicon will remain resistant to IASCC at higher fluences will be confirmed by further tests on our medium- and high-fluence specimens, i.e., specimens irradiated to ≈0.9 x 10^{21} and ≈2.8 x 10^{21} n·cm^{-2}, respectively. Nevertheless, the results in Fig. 37 provide conclusive evidence that silicon and nitrogen concentrations >1 and >0.01 wt.%, respectively are effective in delaying the onset fluence of IASCC. This finding is also consistent with the results of the previous investigation which showed that for a fluence range of ≈0.6 x 10^{21} to ≈2 x 10^{21} n·cm^{-2}, Type 304L SS neutron-absorber tubes fabricated from commercial-purity material (high silicon) were more resistant to IASCC than high-purity material (low silicon).[38]

Initial tests were conducted on four medium-fluence SS specimens irradiated to ≈0.9 x 10^{21} n·cm^{-2} (E > 1 MeV). For these alloys (Heat ID L20, L22, L11, and L18), the effects of higher fluence on the yield stress, uniform and total strains, and the percent IGSCC and TGSCC were significant, as is shown in Fig. 38. Susceptibility of three of the alloys that contain <50 wppm nitrogen and <1.0 wt.% silicon (Heat ID L22, L11, and L18) to IGSCC was significant at ≈0.9 x 10^{21} n·cm^{-2} (E > 1 MeV). Preliminary results from the tests also indicate that when fluence increased from ≈0.3 x 10^{21} to ≈0.9 x 10^{21} n·cm^{-2}, susceptibility to TGSCC decreases in the low-nitrogen, low-silicon alloys, and at the same time, susceptibility to IGSCC increases at the expense of percent TGSCC (see Figs. 38E-G). This trend is consistent with observations on field-cracked components.

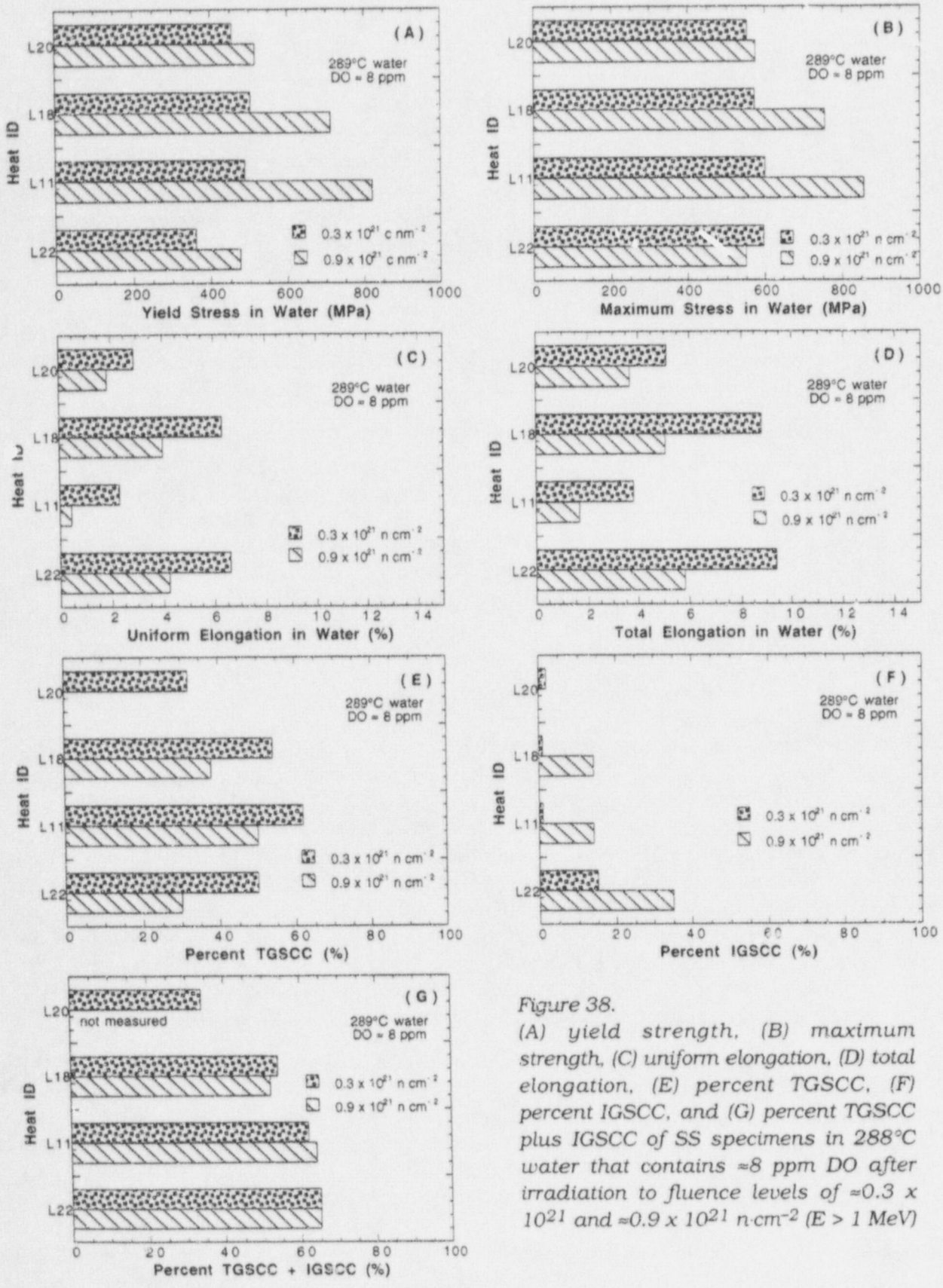

Figure 38.
(A) yield strength, (B) maximum strength, (C) uniform elongation, (D) total elongation, (E) percent TGSCC, (F) percent IGSCC, and (G) percent TGSCC plus IGSCC of SS specimens in 288°C water that contains ≈8 ppm DO after irradiation to fluence levels of ≈0.3 x 10^{21} and ≈0.9 x 10^{21} n·cm^{-2} (E > 1 MeV)

3.2 Fracture Toughness J-R Test of Austenitic Stainless Steels Irradiated in Halden Reactor (E. E. Gruber and O. K. Chopra)

The facility for conducting mechanical tests, e.g., fracture toughness J-R curve, fatigue crack growth, and tensile tests, on irradiated austenitic stainless steel specimens in a hot cell has been designed, fabricated, and assembled. Fracture toughness J-R curve tests are being conducted according to ASTM Specification E 1737 (Standard Test Method for J-Integral Characterization of Fracture Toughness), and fatigue crack growth tests are being conducted according to ASTM Specification E 647 (Standard Test Method for Measurement of Fatigue Crack Growth Rates) on 1/4-T CT specimens at room temperature and 288°C on nonirradiated specimens to validate the test procedure. The method involves pin loading of fatigue precracked specimens and determination of J as a function of crack growth. Load versus loadline (LL) displacement is recorded to calculate the J-integral. The calculated J-integral is plotted against estimated or physical crack lengths Δa, within specified limits of crack growth. The crack length and crack growth are being determined from both elastic compliance measurements and direct current (DC) potential drop technique.

During this reporting period, fracture toughness J-R curve tests and tensile tests were conducted on 50% CW Type 316NG SS at room temperature and 288°C. Tensile tests were also conducted on two heats of thermally aged CF-8M cast SS (ANL Heat 75 with 28% ferrite and Framatome Heat 4331 with 23% ferrite) to validate the test procedure.

3.3.1 Tensile Tests

Tensile tests were performed according to ASTM Specification E 8 "Standard Test Methods for Tension Testing of Metallic Materials" in the facility for mechanical testing of irradiated materials. Dog bone specimens (19.1 mm gauge length and 3.15 x 0.8 mm cross section) were used for all the tests (Fig. 39). Specimen extension was monitored and controlled outside of the high-temperature zone; extension rate for all the tests was 5.3×10^{-4}. The strain in the gauge length of the specimen is determined by subtracting the machine compliance from the measured extension. All tests were conducted at an extension rate of 0.01 mm·s^{-1} (which corresponds to an initial strain rate of 9×10^{-4} s^{-1}).

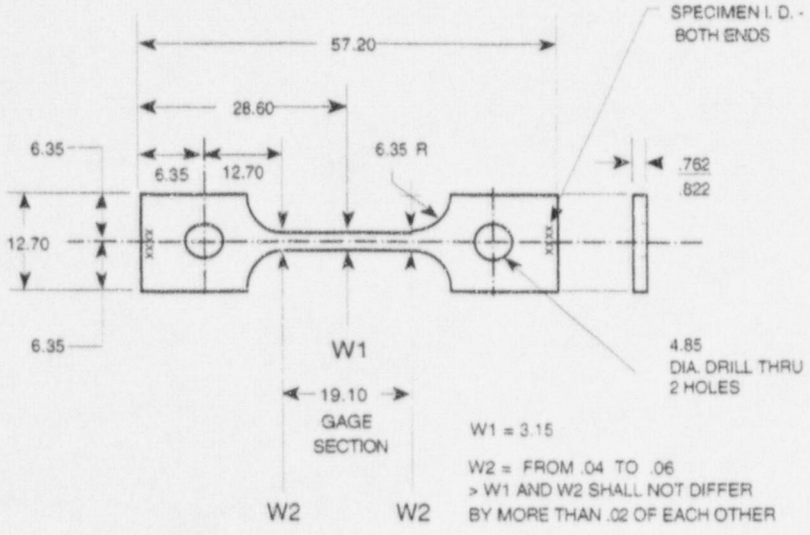

Figure 39. Configuration of fatigue test specimen (dimensions in mm)

Engineering stress versus strain curves for the ANL Heat 75 and Framatome Heat 4331 of CF-8M cast SS are shown in Fig. 40. The stress–strain curve for Heat 75 shows good agreement with the results obtained on cylindrical specimens (5.1 mm diameter and 20.3 mm gage length) of the material (Fig. 41).[43] The stress–strain curves for 50% CW Type 316NG SS at room temperature and 288°C are shown in Fig. 42. The results yield average flow stress values of 966 and 861 MPa (140 and 125 ksi), respectively, at room temperature and 288°C.

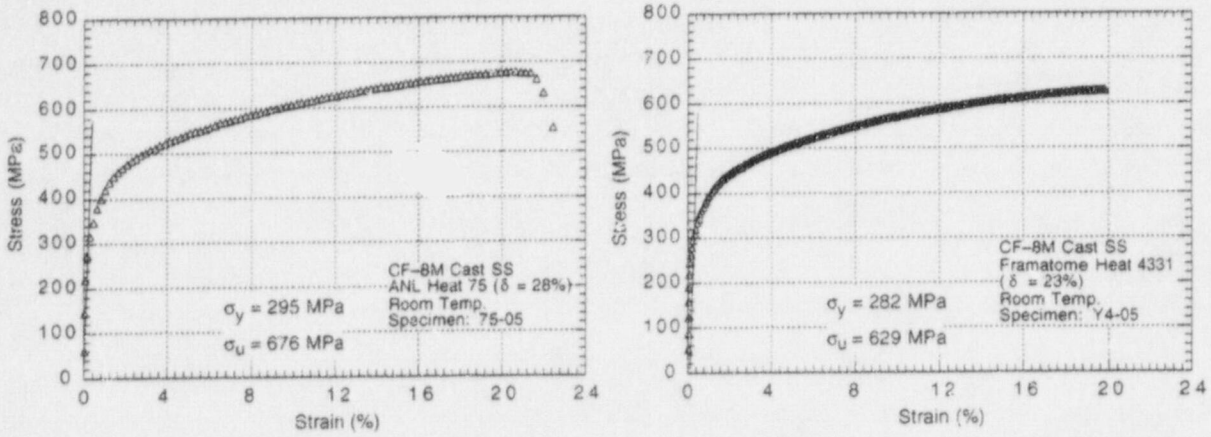

Figure 40. Engineering stress versus strain curves for dog bone specimens of two heats of CF-8M cast SS at room temperature

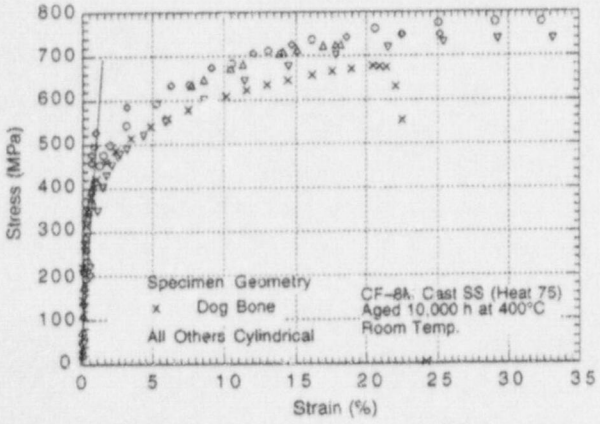

Figure 41. Engineering stress versus strain curves for cylindrical and dog bone specimens of CF-8M cast SS at room temperature

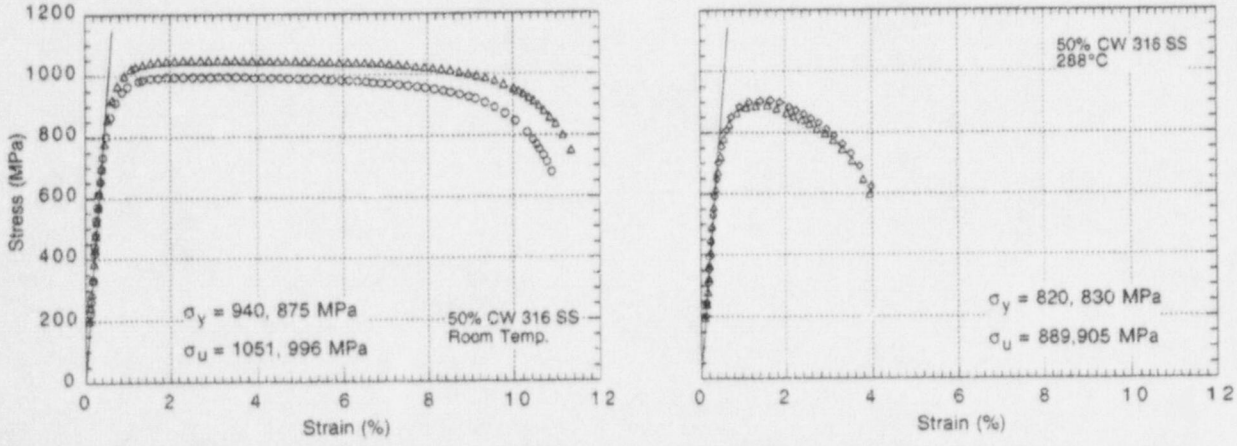

Figure 42. Engineering stress versus strain curves for dog bone specimens of 50% cold-worked Type 316NG SS at room temperature and 288°C

3.3.2 Fracture Toughness J–R Tests

Figures 43 and 44 show the load versus loadline displacement curves and fracture toughness J–R curves for 50% cold worked Type 316NG SS tested at room temperature and 288°C. In the present study, the J–R curves from DC potential method are corrected for both the initial and final crack lengths, whereas the curves from the elastic compliance method are corrected only for the initial precrack length. The J–R curves obtained from the elastic unloading compliance method show excellent agreement with those obtained from the DC potential method. The material shows poor toughness at 288°C, e.g., a J_{IC} value of ≈55 kJ/m^2.

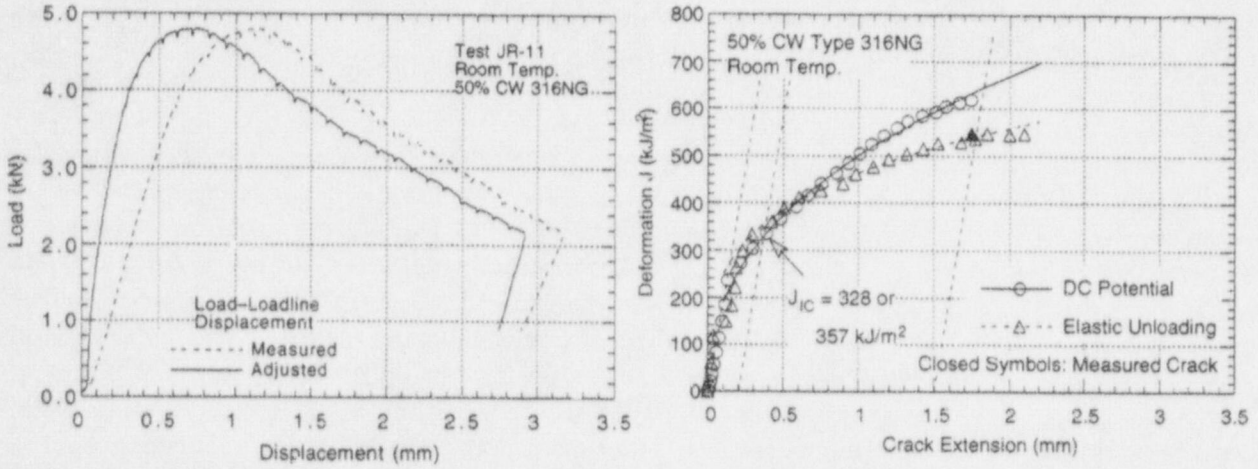

Figure 43. Load versus loadline displacement and fracture toughness J–R curves for 50% cold-worked Type 316NG SS specimen tested at room temperature

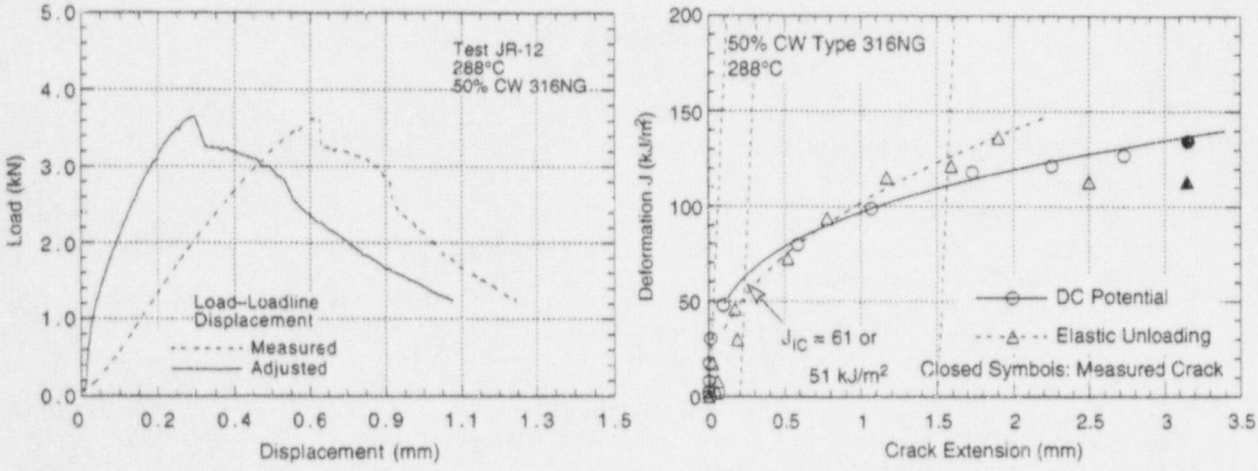

Figure 44. Load versus loadline displacement and fracture toughness J–R curves for 50% cold-worked Type 316NG SS specimen tested at 288°C

4 Environmentally Assisted Cracking of Alloys 600 and 690 in Simulated LWR Water (W. E. Ruther, W. K. Soppet, and T. F. Kassner)

The objective of this work is to evaluate the resistance of Alloys 600 and 690 to EAC in simulated LWR coolant environments. High-nickel alloys have experienced general corrosion (tube wall thinning), localized intergranular attack (IGA), and SCC in LWRs. Secondary-side IGA* and axial and circumferential SCC** have occurred in Alloy 600 tubes at tube support plates in many steam generators. Primary-water SCC of Alloy 600 steam generator tubes in PWRs at roll transitions and U-bends and in tube plugs*** is a widespread problem that has been studied intensively. Cracking has also occurred in Alloy 600 and other high-nickel alloys (e.g., Inconel-82 and -182 and Alloy X750) that are used in applications such as instrument nozzles and heater thermal sleeves in the pressurizer† and the penetrations for control-rod drive mechanisms in reactor vessel closure heads in the primary system of PWRs;†† in dissimilar-metal welds between SS piping and low-alloy steel nozzles, in jet pump hold-down beams,††† and in shroud-support-access-hole covers§ in BWRs. Alloy 600, in general, undergoes differing thermomechanical processing for applications other than those used for steam generator tubes. Because environmental degradation of the alloys in many cases is very sensitive to processing, further evaluation of even SCC is needed. In addition, experience strongly suggests that materials that are susceptible to SCC are also susceptible to environmental degradation of fatigue life and fatigue-crack growth properties. In this investigation, we have obtained information on the effect of temperature, load ratio R, and stress intensity (K) on EAC of Alloys 600 and 690 in simulated BWR and PWR water. Correlations for the crack growth rates (CGRs) were developed based on best fit of the data to equations that incorporate relevant loading parameters and dissolved oxygen concentration in water.

4.1 Material Characterization

4.1.1 Sources of Alloys 600 and 690 for Crack Growth Rate Tests

The Alloy 600 and 690 material was produced by INCO Alloys International, Huntington, WV. Most of the material was provided to us by the Electric Power Research Institute, Palo

---

* USNRC Information Notice No. 91-67, "Problems with the Reliable Detection of Intergranular Attack (IGA) of Steam Generator Tubing," Oct. 1991.

** USNRC Information Notice No. 90-49, "Stress Corrosion Cracking in PWR Steam Generator Tubes," Aug. 1990; Notice No. 91-43, "Recent Incidents Involving Rapid Increases in Primary-to-Secondary Leak Rate," July 1991; Notice No. 92-80, "Operation with Steam Generator Tubes Seriously Degraded," Dec. 1992; Notice No. 94-05, "Potential Failure of Steam Generator Tubes with Kinetically Welded Sleeves," Jan. 1994.

*** USNRC Information Notice No. 89-33, "Potential Failure of Westinghouse Steam Generator Tube Mechanical Plugs," March 1989; Notice No. 89-65, "Potential for Stress Corrosion Cracking in Steam Generator Tube Plugs Supplied by Babcock and Wilcox," Sept. 1989; Notice No. 94-87, "Unanticipated Crack in a Particular Heat of Alloy 600 Used for Westinghouse Mechanical Plugs for Steam Generator Tubes," Dec. 1994.

† USNRC Information Notice No. 90-10, "Primary Water Stress Corrosion Cracking (PWSCC) of Inconel 600," Feb. 1990.

†† USNRC Generic Letter 97-01: "Degradation of Control Rod Drive Mechanism and Other Vessel Closure Head Penetrations," Apr. 1, 1997; USNRC Information Notice No. 96-11, "Ingress of Demineralizer Resins Increases Potential for Stress Corrosion Cracking of Control Rod Drive Mechanism Penetrations," Feb. 1996; INPO Document SER 20-93 "Intergranular Stress Corrosion Cracking of Control Rod Drive Mechanism Penetrations," Sept. 1993.

††† USNRC Information Notice No. 93-101, "Jet Pump Hold-Down Beam Failure," Dec. 1993.

§ USNRC Information Notice No. 92-57, "Radial Cracking of Shroud Support Access Hole Cover Welds," Aug. 1992.

Alto, CA. One heat was obtained from INCO Alloys International and from the A. M. Castle and Company; several specimens were purchased from the Metal Samples Company. The heat of Alloy 600 (NX9244G) with a low-carbon content (0.03 wt.%) was also produced by INCO Alloys International for the Kobe Material Testing Laboratory Company Ltd., Hyogo, Japan. The Kobe Material Testing Laboratory heat treated the plates and cut them into small blocks (≈32 x 65 x 140 mm) for distribution to various laboratories that participated in the International Crack Growth-EAC investigation of Alloy 600 in simulated BWR and PWR environments. The compact-tension specimens of Alloy 600 with a nominal carbon content of ≈0.06% and all heats of Alloy 690 were in the orientation corresponding to identification code L-T for plates in ASTM Specification E399. Compact-tension specimens Alloy 600 with a low-carbon content were fabricated so that the orientation of the crack plane in the specimens corresponds to the identification code T-L for plates in the ASTM specification. The heat identification numbers, heat and heat-treatment identification code, product form, and source of materials for fabrication of 1T compact-tension (1TCT) specimens are given in Table 12.

4.1.2 Compositions and Tensile Properties of Solution–Annealed and Thermally Treated Alloys 600 and 690

The compositions of Alloys 600 and 690 are given in Tables 13 and 14, respectively. The tensile properties of cylindrical specimens of these materials in air at 25, 290, and 320°C and at a strain rate of 1.0×10^{-4} s^{-1} were determined in accordance with ASTM Standard E8. Vickers hardness was measured at room temperature, and average grain size of the various heats of Alloys 600 and 690 was determined by following the procedure in ASTM Standard E112. The results for Alloys 600 and 690, which were reported previously,[44-47] are given in Tables 15 and 16, respectively. Properties obtained from certified material test reports supplied by the vendors or documentation obtained from the EPRI are also included in Tables 15 and 16.

ASTM grain sizes for Heat Nos. NX8844B-33, J422, NX8197, NX8844J-26, and NX8844G-3 with ≈0.06% carbon are 8, 7, 6, 4, and 2, respectively, which correspond to average grain diameters, respectively, of ≈20, 30, 45, 90, and 180 μm.[44,45] In the case of the low-carbon heat of Alloy 600 (NX9244G), two blocks were solution-annealed at 1025 and 1115°C for 2 h, and two blocks that had been subjected to these solution heat treatments were thermally treated at 600°C for 24 h. Solution heat treatments at 1025 and 1115°C produced ASTM grain sizes of ≈1.0-1.5 and 0.2-0.4, respectively, corresponding to large average grain diameters of ≈250-210 and 340-310 μm. Alloy 690 heats NX8662HG-33, NX8625HG-21, and NX8244HK-1A have an ASTM grain size of 5, and heat NX8244HK-1B, which was annealed at a higher temperature (1093 versus 982°C), has a grain size of 2; the corresponding average grain diameters are ≈65 and 180 μm, respectively.[44,45]

A small section of each material was used to prepare metallographic specimens to qualitatively determine the degree of grain boundary carbide coverage by optical metallography. Specimens were polished to a 0.25–μm diamond finish with Struers DP–Spray, and a Vickers hardness indentation was made to provide a reference point for subsequent examination to reveal the carbide distribution and grain boundaries after two chemical etching methods. The specimens were electroetched in a 10% H_3PO_4 solution at ≈10 V for ≈25 s, rinsed in ethanol, and air-dried. Photomicrographs obtained at 500X magnification revealed that carbides were the predominant phase in the specimens. The specimens were repolished with 1.0 and 0.25–μm diamond spray, electroetched in a 5% nital solution (5 mL of HNO_3 in

Table 12. Product form and source of Alloys 690 and 600

Material	Heat No.	Material Condition	Heat/Heat Treat. Ident. Code	Product Form	Source
600	NX8197	Mill Annealed	1	1.0 in.-thick plate	A. M. Castle & Co.
600	NX8844J-26	Annealed 1038°C/1 h	2	1.0-in.-thick plate	EPRI[a]
600	J422	Mill Annealed	3	1T-CT specimens	Metal Samples Co.
600	NX9244G-J310	Annealed 1115°C/2h	4	1.25-in.-thick plate	Kobe Matl. Testing Lab.[b]
600	NX9244G-J311	Annealed 1115°C/2h + 600°C/24h	5	1.25-in.-thick plate	Kobe Matl. Testing Lab.[b]
600	NX9244G-J320	Annealed 1025°C/2h	6	1.25-in.-thick plate	Kobe Matl. Testing Lab.[b]
600	NX9244G-J321	Annealed 1025°C/2h + 600°C/24h	7	1.25-in.-thick plate	Kobe Matl. Testing Lab.[b]
600	NX8844B-33	Annealed 872°C/1 h	8	1.0-in.-thick plate	EPRI[a]
600	NX8844G-3	Hot Worked 982°C, 20% Reduction	9	1.0-in.-thick plate	EPRI[a]
690	NX8244HK-1A	Annealed 982°C/1 h	10	1.0-in.-thick plate	EPRI[a]
690	NX8244HK-1B	Annealed 1093°C/1 h	11	1.0-in.-thick plate	EPRI[a]
690	NX8662HG-33	Annealed + 715°C/5 h	12	1.34-in.-thick plate	INCO Alloys Intl., Inc.
690	NX8625HG-21	Annealed + 715°C/5 h	13	1.34-in.-thick plate	EPRI[a]

[a]INCO Alloys Intl., Inc. of Huntington, WV, produced numerous heats of Alloys 600 and 690 for the Electric Power Research Institute, Palo Alto, CA, which provided materials for this study.

[b]INCO Alloys Intl., Inc. of Huntington, WV, produced the alloys for the Kobe Material Testing Laboratory, Co., Hyogo, Japan, where the alloys were heat treated and cut into small blocks.

Table 13. Composition of Alloy 600 for corrosion fatigue tests

Heat No.	Analysis	Composition (wt.%)															
		Cr	Mo	Ni	Fe	Mn	Si	C	N	P	S	B	Cu	Ti	Al	Co	Nb+Ta
NX8197	Vendor	15.88	–	75.05	7.76	0.22	0.23	0.080	–	0.006	0.002	–	0.12	0.27	0.26	0.05	0.07
	ANL	15.43	0.58	73.82	9.20	0.20	0.27	0.080	0.0099	0.016	0.002	0.002	0.11	0.18	0.24	0.06	0.05
NX8844	Vendor	14.97	0.15	75.21	8.26	0.26	0.24	0.069	0.01	0.009	<0.001	0.004	0.22	0.29	0.27	0.04	–
NX8844B-33	ANL	15.03	0.17	75.16	7.93	0.24	0.27	0.080	0.0146	0.019	0.001	0.003	0.22	0.21	0.28	0.04	0.04
NX8844J-26	ANL	15.00	0.16	74.94	8.14	0.23	0.32	0.060	0.0155	0.014	0.002	0.004	0.22	0.24	0.24	0.03	0.03
NX8844G-3	ANL	15.14	0.16	74.78	8.28	0.23	0.35	0.070	0.0145	0.015	0.002	0.005	0.22	0.25	0.25	0.04	0.04
J422	Vendor	15.36	–	75.72	7.51	0.21	0.32	0.080	–	0.008	<0.001	–	0.15	0.24	0.28	0.05	0.07
	ANL	15.37	0.23	76.36	7.27	0.20	0.32	0.080	0.0145	0.016	0.004	0.002	0.15	0.16	0.27	0.05	0.06
NX9244G	Vendor	15.51	–	75.32	7.90	0.23	0.25	0.032	0.01	0.007	<0.001	0.001	0.09	0.39	0.20	–	0.02
NX9244G-J31	ANL	15.47	0.13	75.40	7.73	0.23	0.37	0.040	0.0052	0.010	0.001	0.001	0.07	0.40	0.17	0.06	<0.01
NX9244G-J32	ANL	16.39	0.11	75.50	7.44	0.22	0.35	0.030	0.0067	0.011	0.001	0.001	0.08	0.40	0.17	0.06	0.01

Table 14. Composition of Alloy 690 for corrosion fatigue tests

Heat No.	Analysis	Composition (wt.%)															
		Cr	Mo	Ni	Fe	Mn	Si	C	N	P	S	B	Cu	Ti	Al	Co	Nb+Ta
NX8244HK	Vendor	30.03	–	59.85	9.20	0.20	0.14	0.018	0.01	0.004	<0.001	0.002	<0.01	0.20	0.36	0.003	–
NX8244HK-1A	ANL	30.66	<0.01	59.09	9.22	0.20	0.18	0.024	0.010	0.004	0.002	0.002	<0.01	0.20	0.31	<0.01	<0.01
NX8244HK-1B	ANL	30.64	<0.01	59.20	9.19	0.21	0.18	0.023	0.011	0.005	0.002	0.002	<0.01	0.19	0.32	<0.01	<0.01
NX8662HG-33	Vendor	30.25	–	59.31	9.54	0.10	0.16	0.030	0.050	0.008	<0.001	0.004	0.04	0.28	0.33	0.022	–
	ANL	30.46	0.04	58.88	9.22	0.11	0.16	0.030	0.047	0.017	0.001	0.003	0.05	0.25	0.32	0.020	0.01
NX8625HG-21	Vendor	30.28	–	58.56	10.00	0.11	0.26	0.027	0.030	0.009	<0.001	0.004	0.06	0.32	0.44	0.036	–
	ANL	30.64	0.02	58.10	9.84	0.12	0.32	0.030	0.029	0.009	0.002	0.004	0.01	0.28	0.39	0.030	<0.01

100 mL ethanol) at ≈10 V for ≈35 s, rinsed in ethanol, and air dried. The same locations on the specimens were photographed once again at a magnification of 500X, with the aid of the hardness indentation, to better reveal grain boundaries and obtain a qualitative estimate of the extent of carbide precipitation thereon.

Photomicrographs of five heats of Alloy 600 with ≈0.06 wt.% carbon indicated a uniform distribution of intergranular and intragranular carbides (NX8844B-33), continuous (NX8197), or semicontinuous (NX8844J-26, J422, and NX8844G-3) carbide precipitation at the grain boundaries and a significant amount of intragranular carbide.[44,45] Because of the low carbon content (≈0.03%) and relatively high solution-annealing temperatures of Heat NX9244G, intergranular carbides were not observed in the specimens by optical and scanning electron microscopy. Photomicrographs of the four heats of Alloy 690 (≈0.03 wt.% carbon) revealed continuous precipitation of carbides at the grain boundaries, with relatively few intragranular carbides.[44,45] The precipitate phases present in Alloys 600 and 690 are Cr-rich M_7C_3 and $M_{23}C_6$ carbides and Ti(C,N) carbonitrides.[48-50] In general, the microstructures are consistent with the thermomechanical processing histories and carbon concentrations vis-a`-vis the solubility of carbon in the materials.[51] Namely, according to the carbon solubility data, annealing temperatures of 1025 and 1115°C for the low-carbon Alloy 600 were high enough (>1000°C) to dissolve carbon in the grain matrix. However, none of the other materials was annealed at a temperature sufficient to dissolve all of the carbon in the grain matrix (i.e., >1200°C for Alloy 690 with ≈0.03% carbon, and >1080°C for Alloy 600 with ≈0.06% carbon); consequently, carbides are present on grain boundaries as well as within the grains of these materials.

The dependence of yield stress on grain size for the various heats of Alloy 600 follows a Petch relationship, i.e., $\sigma_y = \sigma_i + k \cdot d^{-1/2}$, where σ_y is the yield stress; d is the grain diameter; k, an empirical constant; and σ_i, the "friction" stress, which is a measure of intrinsic resistance of the material for dislocation motion. Heat treatment at 600°C for 24 h of the low-carbon content heat (NX9244G) has virtually no effect on the tensile properties when compared with this material in the solution-annealed condition. Yield stress also decreases as average grain diameter increases for Alloy 690; however, heats with only two grain sizes (i.e., ASTM 5 and 2) were investigated.

4.2 Experimental Methods for Measuring CGR in Alloys 600 and 690

The experimental procedures relevant to our mechanical loading systems are similar to those in ASTM E647. The tests are performed under controlled loading conditions with closed-loop servo-controlled machines (MTS™ systems). The contribution to the load that arises from the pressure difference between the inside and the outside of the autoclave is taken into consideration. Additional mechanical contributions that arise from friction between the pull rod in the load train and the autoclave pressure seal are typically <0.4% of the mechanical loading force under autoclave operating pressure and temperature.

The tests in air are performed in a system that is also used for tests in simulated reactor coolant environments. Air is circulated at a slow rate through the autoclave at atmospheric pressure to help maintain a uniform temperature within the autoclave. For tests in air, there is no mechanical contribution from pressure differences between the inside and the outside of the autoclave or from friction in the load train, because there is no seal between the pull rod and the autoclave.

Table 15. Tensile properties of Alloy 600 in various heat-treatment conditions

Alloy 600 Heat No.	Material Condition	Test No.	Spec. No.	Temp. (°C)	σ_u (MPa)	σ_y (MPa)	ε_t (%)	RA (%)	Hardness[a] (VN)	Hardness (R_b)	ASTM Grain Size
NX8197	Mill Annealed	–[b]	–[b]	25	683.3	256.5	42.0	–	–	81	–
NX8197	Mill Annealed	T7	197-04[c]	25	683.9	373.6	42.2	64.4	182	91	6
NX8197	Mill Annealed	T12	197-05[c]	25	685.4	392.8	41.6	64.9	–	–	–
NX8197	Mill Annealed	T3	197-02[c]	290	668.1	316.[c]	46.8	62.2	–	–	–
NX8844J-26	Annealed 1038°C/1 h	–[b]	–[b]	25	694.3	298.6	41.0	–	–	86	4
NX8844J-26	Annealed 1038°C/1 h	T21	J26-05[c]	25	653.5	245.5	49.2	61.1	173	87	4
NX8844J-26	Annealed 1038°C/1 h	T23	J26-06[c]	290	637.8	234.0	45.2	53.3	–	–	–
NX8844J-26	Annealed 1038°C/1 h	T44	J26-08[c]	290	626.5	218.0	48.7	57.2	–	–	–
NX8844J-26	Annealed 1038°C/1 h	T25	J26-07[c]	320	639.4	246.8	45.8	48.9	–	–	–
J422	Mill Annealed	–[b]	–[b]	25	722.6	273.0	40.0	–	–	87	–
J422	Mill Annealed	T20	IN-05[c]	25	732.8	370.7	39.2	64.5	197	93	7
J422	Mill Annealed	T9	IN-03[c]	290	699.4	313.7	40.1	53.5	–	–	–
J422	Mill Annealed	T11	IN-04[c]	320	697.9	311.3	39.0	53.9	–	–	–
NX9244G	Mill Annealed	–[b]	–[b]	25	657.0	300.0	43.9	60.6	–	83	–
NX9244G-J310	Annealed 1115°C/2 h	T40	J310-01[c]	25	551.7	188.7	58.7	77.5	144	78	0.4
NX9244G-J310	Annealed 1115°C/2 h	T41	J310-02[c]	290	508.9	155.7	65.5	68.8	–	–	–
NX9244G-J310	Annealed 1115°C/2 h	T42	J310-03[c]	320	507.5	146.1	67.7	69.5	–	–	–
NX9244G-J311	Annealed 1115°C/2 h + 600°C/24 h	T30	J311-03[d]	25	545.7	194.5	57.2	61.5	–	–	–
NX9244G-J311	Annealed 1115°C/2 h + 600°C/24 h	T31	J311-04[c]	25	553.1	196.4	56.8	63.0	142	77	0.2
NX9244G-J311	Annealed 1115°C/2 h + 600°C/24 h	T33	J311-05[c]	290	517.0	155.7	66.7	65.9	–	–	–
NX9244G-J311	Annealed 1115°C/2 h + 600°C/24 h	T36	J311-06[c]	320	514.9	155.7	65.3	60.6	–	–	–
NX9244G-J320	Annealed 1025°C/2 h	T43	J320-04[c]	25	580.6	205.1	62.7	82.0	145	78	1.0
NX9244G-J320	Annealed 1025°C/2 h	T38	J320-02[c]	290	547.9	155.7	68.4	72.2	–	–	–
NX9244G-J320	Annealed 1025°C/2 h	T39	J320-03[c]	320	551.9	154.5	69.9	70.1	–	–	–
NX9244G-J321	Annealed 1025°C/2 h + 600°C/24 h	T32	J321-03[c]	25	582.0	208.4	59.5	66.1	148	79	1.5
NX9244G-J321	Annealed 1025°C/2 h + 600°C/24 h	T35	J321-05[c]	290	552.1	172.5	65.2	59.8	–	–	–
NX9244G-J321	Annealed 1025°C/2 h + 600°C/24 h	T34	J321-04[c]	320	551.6	166.9	67.0	64.4	–	–	–
NX8844B-33	Annealed 872°C/1 h	–[b]	–[b]	25	748.8	339.9	35.5	–	–	90	7.5
NX8844B-33	Annealed 872°C/1 h	T19	B33-05[c]	25	714.9	333.2	39.6	66.9	190	91	8
NX8844B-33	Annealed 872°C/1 h	T8	B33-03[c]	290	686.1	282.6	38.6	61.1	–	–	–
NX8844B-33	Annealed 872°C/1 h	T10	B33-04[c]	320	680.6	282.6	39.1	55.5	–	–	–
NX8844G-3	Hot Worked 982°C, 20% Reduction	–[b]	–[b]	25	697.8	355.1	38.5	–	–	85	2.5
NX8844G-3	Hot Worked 982°C, 20% Reduction	T13	G3-05[c]	25	666.4	335.3	43.5	56.9	173	88	2
NX8844G-3	Hot Worked 982°C, 20% Reduction	T15	G3-06[c]	290	630.1	292.2	44.1	53.5	–	–	–
NX8844G-3	Hot Worked 982°C, 20% Reduction	T17	G3-07[c]	320	630.3	297.0	44.9	54.9	–	–	–

[a]Vickers hardness at room temperature, 500 gf, 15 s.
[b]Results from vendor documents.
[c]Tensile tests conducted in air at a strain rate of 1.0×10^{-4} s^{-1}.

A DC potential-drop measurement system is used for both the tests in air and those in an HP water environment. The specimens in the load train are electrically insulated from the autoclave and each other by using oxidized Zircaloy 705 pins (oxidized by heating at 550°C for 4-8 h) to attach the specimens to the load train. Resistance across the crack is measured by the potential drop for each specimen as a computer automatically controls a programmable DC power supply to direct the electrical current first in one direction and then in the reverse direction. The DC and drops in potential are measured by high-accuracy, stable, scanning multimeters that are controlled by the computer over an IEEE-488 interface. Hundreds of measurements are averaged for one reading, which is transformed to a crack length by a software algorithm that is integral to the control computer. Corrosion-fatigue specimens are held at operating conditions without mechanical loading until the resistance of the specimens stabilizes, typically one week, before the initial fatigue loading at R = 0.4 is applied.

Table 16. Tensile properties of Alloy 690 in various heat-treatment conditions

Alloy 690 Heat No.	Material Condition	Test No.	Spec. No.	Temp. (°C)	σ_u (MPa)	σ_y (MPa)	ε_t (%)	RA (%)	Hardness[a] (VN)	Hardness (R_b)	ASTM Grain Size
NX8244HK-1A	Annealed 982°C/1 h	–[b]	–[b]	25	665.0	245.2	51.0	–	–	78	–
NX8244HK-1A	Annealed 982°C/1 h	T14	K1A-03[c]	25	647.7	256.3	56.9	75.2	160	83	5
NX8244HK-1A	Annealed 982°C/1 h	T16	K1A-04[c]	290	569.8	195.4	58.5	71.8	–	–	–
NX8244HK-1A	Annealed 982°C/1 h	T18	K1A-05[c]	320	572.2	196.4	58.2	71.7	–	–	–
NX8244HK-1B	Annealed 1093°C/1 h	–[b]	–[b]	25	602.8	212.3	59.0	–	–	70	–
NX8244HK-1B	Annealed 1093°C/1 h	T22	K1B-05[c]	25	592.2	215.6	70.5	71.6	146	78	2
NX8244HK-1B	Annealed 1093°C/1 h	T24	K1B-06[c]	290	504.9	145.2	70.6	68.1	–	–	–
NX8244HK-1B	Annealed 1093°C/1 h	T26	K1B-07[c]	320	499.4	150.9	67.1	67.3	–	–	–
NX8662HG-33	Annealed + 715°C/5 h	–[b]	–[b]	25	670.2	291.7	43.5	–	–	82	5
NX8662HG-33	Annealed + 715°C/5 h	T6	HG-03[c]	25	683.8	292.1	48.7	63.2	214	96	5
NX8662HG-33	Annealed + 715°C/5 h	T2	HG-01[c]	290	601.2	237.1	49.7	61.6	–	–	–
NX8662HG-33	Annealed + 715°C/5 h	T4	HG-02[c]	320	598.8	232.3	50.7	62.8	–	–	–
NX8625HG-21	Annealed + 715°C/5 h	–[b]	–[b]	25	660.5	268.9	48.0	–	–	82	4
NX8625HG-21	Annealed + 715°C/5 h	T27	G21-03[c]	25	641.8	297.0	56.4	75.2	163	84	5
NX8625HG-21	Annealed + 715°C/5 h	T28	G21-04[c]	290	570.9	225.2	56.0	58.8	–	–	–
NX8625HG-21	Annealed + 715°C/5 h	T29	G21-06[c]	320	567.8	220.4	56.9	61.3	–	–	–

[a]Vickers hardness at room temperature, 500 gf, 15 s.
[b]Results from vendor document.
[c]Tensile tests conducted in air at a strain rate of 1.0×10^{-4} s^{-1}.

Resolution of the crack length varies somewhat from one specimen to another and depends on the alloy composition and uniform crack length; a typical value is ±0.05 mm (0.002 in.) for Alloy 600 or 690.

When tests are conducted in a simulated PWR environment (boric acid, lithium hydroxide, and hydrogen overpressure), the DC potential-drop system, which indicates negative CGRs, fails shortly after the cracks begin to grow. Our best explanation is that hydrogen enters the metal matrix and changes the intrinsic resistance of the specimen. For CGR tests in simulated PWR water, a compliance technique that was used previously was upgraded to perform measurements without interrupting the corrosion-fatigue test.

The compliance measurement system is composed of MTS™ Model 632.10 hermetically sealed crack-opening-displacement (COD) gauges interfaced to a computer data acquisition system along with a conditioned load cell signal. Prior to each test, the COD gauges are calibrated with a micrometer fixture to an accuracy of ±1% at the desired test temperature. The micrometer fixture is calibrated with gauge blocks that are traceable to the National Institute of Standards and Technology. The resulting typical COD gauge output transfer function is 0.075 mm/V. Experience with compliance measurements with MTS™ clip gauges indicates that the resolution is ±0.025 mm (0.001 in.). The computer data acquisition system accepts the multiplexed load and COD voltage signals with a resolution of ±0.05% of the applied voltage range. Compliance data from the load cell and COD gauges are acquired during the unloading phase of the ramp waveform. Initially, the load-versus-COD data are graphically analyzed to select the region of the waveform with the steepest linear slope to optimize the data acquisition period. The compliance value for a test cycle is computed by a least-squares linear-regression analysis of 250 data samples. The computer software monitors the fit of the linear regression curve for a minimum correlation coefficient of 0.999. During a corrosion-fatigue test, 10 successive load-line compliance values are recorded at 1-h time intervals, averaged, and applied to a subroutine that calculates crack length by means of a

polynomial elastic compliance expression derived for CT and wedge-opening-load specimens.[52] However, for conditions of accelerated crack growth, the measurement time interval can be reduced to 10 min.

Both the initial crack length and the crack length and shape at the end of the test are determined from the fracture surface for comparison with measurements inferred from COD or DC potential-drop measurements. The specimen is cut into two pieces along the midplane of the thickness, and the crack in one piece is extended by fracturing at a cryogenic temperature. One of these segments is used to examine the fracture surface by SEM. Excess metal in the noncracked region of the other piece is removed with a cutoff wheel, and a transverse section is prepared and polished for metallographic evaluation of the region that contains the corrosion-fatigue crack to confirm the nature of the crack path and determine whether crack branching had occurred.

Water for the CGR test systems is obtained from a reverse-osmosis purification system and is passed through a demineralizer with mixed-bed ion-exchange resins; the conductivity is $<0.1\ \mu S \cdot cm^{-1}$. To avoid contamination by nonionic organic contaminants, the water flows though a final water purification system (e.g., a Millipore Super-Q Ultrapure Water System™ coupled with an Ultra Dynamics UV Purifier™) that contains a bed of activated charcoal, an Organex bed, a resin bed, and a 0.2-μm filter. The purified water is stored in 135-L SS feedwater tanks that are refilled weekly. The feedwater tanks are connected to the autoclave systems with SS tubing. Whenever the conductivity of the stored feedwater solution increases to $\geq 0.1\ \mu S \cdot cm^{-1}$ during the storage period, the tanks are spray-sterilized/passivated with a 10% hydrogen peroxide solution and thoroughly rinsed with deionized water prior to refilling. The DO level is adjusted by vacuum sparging of the filled tanks; nitrogen or hydrogen is used for low-DO tests and oxygen-nitrogen gas mixtures are used to establish predetermined DO levels. Final adjustment of the effluent DO in the latter tests is achieved by slightly varying the storage tank pressure and/or the flow rate of water in the autoclave. The DO concentration in the effluent stream from the autoclaves is monitored by Chemetrics™ ampoules and/or by an Orbisphere™ DO monitor. The electrochemical potential of platinum and SS electrodes is measured versus a room-temperature 0.1N KCl/Ag/AgCl reference electrode located in the high-temperature effluent stream (289°C) from the autoclave. The platinum potential, in particular, responds rapidly to changes in DO concentrations in simulated LWR coolant water.

4.3 Data Base for Crack Growth Rates of Alloys 600 and 690 in Air and Water

Crack growth experiments were performed on sets of 1TCT specimens of Alloys 600 and 690 to explore the effects on CGRs of temperature, load ratio, stress intensity, and water chemistry; namely DO and dissolved hydrogen in deionized water, and ionic impurities (e.g., chromate and sulfate) in several experiments. Experiments were also performed in simulated PWR primary-system water that contained either 450 or 1200 ppm boron and 2.25 ppm lithium (added to the feedwater as H_3BO_3 and LiOH), 3–58 $cm^3\ H_2 \cdot kg^{-1}\ H_2O$, and ≈1 ppb DO. Hydrazine (750 ppb) was added to feedwater in several experiments to scavenge residual DO to a very low level; however, it raised conductivity from ≈25 to 42 $\mu S \cdot cm^{-1}$. In these experiments, the role of H_3BO_3, LiOH, and dissolved hydrogen in crack growth was investigated vis-a-vis HP deoxygenated water. Temperature and dissolved-hydrogen concentration in water influence the stability of NiO on nickel-base alloys and conceivably could influence EAC of the alloys if a slip-dissolution or slip-oxidation mechanism for crack propagation was operative.[53] Crack

growth experiments were also performed on 1TCT specimens of these alloys in air at several temperatures between 35 and 320°C.[54] The results of the CGR experiments in air and aqueous environments under cyclic loading conditions have been reported previously.[44-47,53,54] The results for Alloys 600 and 690 are summarized in Tables 17 and 18, respectively.

4.4 Analysis of CGR Data

4.4.1 Quality Assessment of Crack Growth Data

Initially, a least-squares regression analysis was performed on CGR data sets for Alloys 600 and 690 in air and water environments to determine the best-fit to the Paris[55] power-law equation:

$$CGR = C \cdot \Delta K^n. \tag{11}$$

The predicted CGRs were then compared with experimental values in air and water environments to examine the potential cause for any experimental points that deviate from the predicted values by factors >≈5. No "outliers" were found in the CGRs of these alloys in air at 35, 135, and 289°C, although CGRs of $<1 \times 10^{-11}$ m·s^{-1} were not included in the analysis. However, for Alloy 600 in aqueous environments, the comparison revealed several experimental CGRs that lie a factor of >≈5 both above and below the predicted values. Before we began to analyze the effects of loading, material, and environmental variables on the rates, the tables of original data were first checked for possible data entry errors; none were found. Further review of the original data revealed that in hindsight, several factors can account for larger than expected deviations between predicted and experimental values. For example, in some of the experiments on Alloy 600,[46] the test times after decreasing the load ratio were too short (e.g., ≈10-20 h) to attain a valid steady-state rate, although the crack-length-versus-time data were adequate to obtain a transient-rate measurement in route to a higher steady-state rate.

Occasionally, large changes in water chemistry, e.g., decreases in DO from ≈5 ppm to ≈1 ppb in HP water or a similar change in DO accompanied by the addition of H_3BO_3 and LiOH, produced transient CGRs that were greater than the steady-state value, which was eventually attained after a longer time period in the new environment.[53] Lastly, in several instances when the experimental CGRs are $<3 \times 10^{-11}$ m·s^{-1}, large variations between experimental and predicted values were encountered. Examination of the test sequence revealed that this typically occurred when the load ratio is increased from low (<0.8) to high (0.9-0.95) values at constant K_{max} (a decrease in ΔK). In numerous instances, the CGRs decrease to values that are at or below the sensitivity level of the crack-length-monitoring system in an ≈1000 h test.[46,47] Consequently, in a subsequent analysis of the CGR data for Alloys 600 and 690 in simulated BWR and PWR environments, rates of $<3 \times 10^{-11}$ m·s^{-1} were deleted, as were transient CGR data caused by large variations in water chemistry followed by insufficient time periods to accommodate changes to either the crack-tip chemistry or the nature of the corrosion-product layer on the specimens. Thus, a detailed examination of the test conditions in the tables of original data provided a rationale for deleting from the analysis some data that otherwise would tend to augment the normal variability of the CGR data.

Table 17. Summary of crack growth rate data for Alloy 600 in air, high-purity, and simulated PWR water at several temperatures between 35 and 320°C

Alloy 600 Heat No.	Heat Treatment Condition	Specimen Number	Test Environment	Temp. (°C)	Load Ratio	Kmax (MPa·m$^{1/2}$)	ΔK	CGR (m·s^{-1})	Crack Length Measurement	NUREG Report, Table, Page No.
NX8197	MA	197-07	HP <5 ppb DO	320	0.60	33.20	13.28	9.98E-10	DCPD	NUREG/CR-6383, Tbl 8, p. 22
NX8197	MA	197-07	HP <5 ppb DO	320	0.90	33.30	3.33	2.80E-11	DCPD	NUREG/CR-6383, Tbl 8, p. 22
NX8197	MA	197-07	HP <5 ppb DO	320	0.90	33.90	3.39	1.30E-11	DCPD	NUREG/CR-6383, Tbl 8, p. 22
NX8197	MA	197-07	HP <5 ppb DO	320	0.90	33.60	3.36	1.20E-11	DCPD	NUREG/CR-6383, Tbl 8, p. 22
NX8197	MA	197-07	HP <5 ppb DO	320	0.60	33.90	13.56	4.28E-10	DCPD	NUREG/CR-6383, Tbl 8, p. 22
NX8197	MA	197-07	HP <5 ppb DO	320	0.60	34.50	13.80	1.70E-09	DCPD	NUREG/CR-6383, Tbl 8, p. 22
NX8844J-26	SA 1038°C/1h	J26-01	HP <1 ppb DO	320	0.20	30.80	24.64	9.48E-09	DCPD	NUREG/CR-4667, Vol. 22, Tbl 14, p. 60
NX8844J-26	SA 1038°C/1h	J26-01	HP <1 ppb DO	320	0.90	31.10	3.11	1.40E-11	DCPD	NUREG/CR-4667, Vol. 22, Tbl 14, p. 60
NX8844J-26	SA 1038°C/1h	J26-01	HP <1 ppb DO	320	0.90	45.10	4.51	5.50E-11	DCPD	NUREG/CR-4667, Vol. 22, Tbl 14, p. 60
NX8844J-26	SA 1038°C/1h	J26-01	HP <1 ppb DO	320	0.90	59.90	5.99	8.20E-11	DCPD	NUREG/CR-4667, Vol. 22, Tbl 14, p. 60
NX8844J-26	SA 1038°C/1h	J26-01	HP <1 ppb DO	320	0.85	60.70	9.11	5.17E-10	DCPD	NUREG/CR-4667, Vol. 22, Tbl 14, p. 60
NX8197	MA	197-07	HP 6 ppm DO	320	0.60	33.50	13.40	2.25E-09	DCPD	NUREG/CR-6383, Tbl 8, p. 22
NX8197	MA	197-07	HP 6 ppm DO	320	0.90	33.70	3.37	1.49E-10	DCPD	NUREG/CR-6383, Tbl 8, p. 22
NX8197	MA	197-09	PWR <2 ppb DO + H_2	320	0.80	31.90	6.38	5.60E-11	Compliance	NUREG/CR-6383, Tbl 9, p. 27
NX8197	MA	197-09	PWR <2 ppb DO + H_2	320	0.80	31.00	6.20	1.35E-10	Compliance	NUREG/CR-6383, Tbl 9, p. 27
NX8197	MA	197-09	PWR <2 ppb DO + H_2	320	0.80	32.70	6.54	5.60E-11	Compliance	NUREG/CR-6383, Tbl 9, p. 27
NX8197	MA	197-09	PWR <2 ppb DO + H_2	320	0.80	30.60	6.12	6.80E-11	Compliance	NUREG/CR-6383, Tbl 9, p. 27
NX8197	MA	197-09	PWR <2 ppb DO + H_2	320	0.80	32.10	6.42	6.80E-11	Compliance	NUREG/CR-6383, Tbl 9, p. 27
NX9244G	SA 1115°C/2h	J310-01	PWR <1 ppb DO + H_2	320	0.70	26.30	7.90	7.96E-10	Compliance	NUREG/CR-4667, Vol. 24, Tbl 16, p. 75
NX9244G	SA 1115°C/2h	J310-01	PWR <1 ppb DO + H_2	320	0.60	27.00	10.80	1.18E-09	Compliance	NUREG/CR-4667, Vol. 24, Tbl 16, p. 75
NX9244G	SA 1115°C/2h	J310-01	PWR <1 ppb DO + H_2	320	0.50	28.50	14.20	1.66E-09	Compliance	NUREG/CR-4667, Vol. 24, Tbl 16, p. 75
NX9244G	SA 1115°C/2h	J310-01	PWR <1 ppb DO + H_2	320	0.40	29.20	17.50	2.66E-09	Compliance	NUREG/CR-4667, Vol. 24, Tbl 16, p. 75
NX9244G	SA 1115°C/2h	J310-01	PWR <1 ppb DO + H_2	320	0.30	29.50	20.70	2.68E-09	Compliance	NUREG/CR-4667, Vol. 24, Tbl 16, p. 75
NX9244G	SA 1115°C/2h	J310-01	PWR <1 ppb DO + H_2	320	0.80	29.50	5.90	9.40E-11	Compliance	NUREG/CR-4667, Vol. 24, Tbl 16, p. 75
NX9244G	SA 1115°C/2h	J310-01	PWR <1 ppb DO + H_2	320	0.55	30.40	13.68	1.37E-09	Compliance	NUREG/CR-4667, Vol. 24, Tbl 16, p. 75
NX9244G	SA 1115°C/2h	J310-01	PWR <1 ppb DO + H_2	320	0.90	30.60	3.06	2.20E-11	Compliance	NUREG/CR-4667, Vol. 24, Tbl 16, p. 75
NX9244G	SA 1115°C/2h	J310-01	PWR <1 ppb DO + H_2	320	0.65	31.20	10.92	1.17E-09	Compliance	NUREG/CR-4667, Vol. 24, Tbl 16, p. 75
NX9244G	SA 1115°C/2h	J310-01	PWR <1 ppb DO + H_2	320	0.85	31.40	4.71	4.40E-11	Compliance	NUREG/CR-4667, Vol. 24, Tbl 16, p. 75
NX9244G	SA 1115°C/2h	J310-01	PWR <1 ppb DO + H_2	320	0.67	31.70	10.45	7.69E-10	Compliance	NUREG/CR-4667, Vol. 24, Tbl 16, p. 75
NX9244G	SA 1115°C/2h	J310-01	PWR <1 ppb DO + H_2	320	0.45	32.20	17.69	2.76E-09	Compliance	NUREG/CR-4667, Vol. 24, Tbl 16, p. 75
NX9244G	SA 1115°C/2h	J310-01	PWR <1 ppb DO + H_2	320	0.35	32.50	21.14	2.17E-09	Compliance	NUREG/CR-4667, Vol. 24, Tbl 16, p. 75
NX9244G	SA 1115°C/2h	J310-01	PWR <1 ppb DO + H_2	320	0.20	33.10	26.46	3.92E-09	Compliance	NUREG/CR-4667, Vol. 24, Tbl 16, p. 75
NX9244G	SA 1115°C/2h	J310-01	PWR <1 ppb DO + H_2	320	0.33	33.60	22.68	3.21E-09	Compliance	NUREG/CR-4667, Vol. 24, Tbl 16, p. 75
NX9244G	SA 1115°C/2h	J310-01	PWR <1 ppb DO + H_2	320	0.63	33.80	12.51	7.45E-10	Compliance	NUREG/CR-4667, Vol. 24, Tbl 16, p. 75
NX9244G	1115°C/2h+600°C/24h	J311-01	PWR <1 ppb DO + H_2	320	0.70	25.10	7.52	2.03E-10	Compliance	NUREG/CR-4667, Vol. 24, Tbl 16, p. 75
NX9244G	1115°C/2h+600°C/24h	J311-01	PWR <1 ppb DO + H_2	320	0.60	25.20	10.10	1.83E-10	Compliance	NUREG/CR-4667, Vol. 24, Tbl 16, p. 75
NX9244G	1115°C/2h+600°C/24h	J311-01	PWR <1 ppb DO + H_2	320	0.50	25.40	12.70	3.49E-10	Compliance	NUREG/CR-4667, Vol. 24, Tbl 16, p. 75
NX9244G	1115°C/2h+600°C/24h	J311-01	PWR <1 ppb DO + H_2	320	0.40	25.60	15.40	9.15E-10	Compliance	NUREG/CR-4667, Vol. 24, Tbl 16, p. 75
NX9244G	1115°C/2h+600°C/24h	J311-01	PWR <1 ppb DO + H_2	320	0.30	26.10	18.20	2.40E-09	Compliance	NUREG/CR-4667, Vol. 24, Tbl 16, p. 75

Table 17. Contd.

Alloy 600 Heat No.	Heat Treatment Condition	Specimen Number	Test Environment	Temp. (°C)	Load Ratio	K_{max} (MPa·m$^{1/2}$)	ΔK	CGR (m s^{-1})	Crack Length Measurement	NUREG Report, Table, Page No.
NX9244G	1115°C/2h+600°C/24h	J311-01	PWR <1 ppb DO + H_2	320	0.80	26.20	5.24	1.03E-10	Compliance	NUREG/CR-4667, Vol. 24, Tbl 16, p. 75
NX9244G	1115°C/2h+600°C/24h	J311-01	PWR <1 ppb DO + H_2	320	0.55	26.30	11.84	3.21E-10	Compliance	NUREG/CR-4667, Vol. 24, Tbl 16, p. 75
NX9244G	1115°C/2h+600°C/24h	J311-01	PWR <1 ppb DO + H_2	320	0.90	26.50	2.65	2.50E-11	Compliance	NUREG/CR-4667, Vol. 24, Tbl 16, p. 75
NX9244G	1115°C/2h+600°C/24h	J311-01	PWR <1 ppb DO +H_2	320	0.65	26.60	9.31	1.11E-10	Compliance	NUREG/CR-4667, Vol. 24, Tbl 16, p. 75
NX9244G	1115°C/2h+600°C/24h	J311-01	PWR <1 ppb DO + H_2	320	0.85	26.60	3.99	4.00E-12	Compliance	NUREG/CR-4667, Vol. 24, Tbl 16, p. 75
NX9244G	1115°C/2h+600°C/24h	J311-01	PWR <1 ppb DO + H_2	320	0.67	26.60	8.78	8.30E-11	Compliance	NUREG/CR-4667, Vol. 24, Tbl 16, p. 75
NX9244G	1115°C/2h+600°C/24h	J311-01	PWR <1 ppb DO + H_2	320	0.45	26.70	14.69	1.29E-09	Compliance	NUREG/CR-4667, Vol. 24, Tbl 16, p. 75
NX9244G	1115°C/2h+600°C/24h	J311-01	PWR <1 ppb DO + H_2	320	0.35	26.90	17.46	7.07E-10	Compliance	NUREG/CR-4667, Vol. 24, Tbl 16, p. 75
NX9244G	1115°C/2h+600°C/24h	J311-01	PWR <1 ppb DO + H_2	320	0.20	27.30	21.86	4.02E-09	Compliance	NUREG/CR-4667, Vol. 24, Tbl 16, p. 75
NX9244G	1115°C/2h+600°C/24h	J311-01	PWR <1 ppb DO + H_2	320	0.33	27.80	18.74	3.49E-09	Compliance	NUREG/CR-4667, Vol. 24, Tbl 16, p. 75
NX9244G	1115°C/2h+600°C/24h	J311-01	PWR <1 ppb DO + H_2	320	0.63	27.80	10.27	1.43E-10	Compliance	NUREG/CR-4667, Vol. 24, Tbl 16, p. 75
NX9244G	SA 1025°C/2h	J320-01	PWR <1 ppb DO + H_2	320	0.40	25.30	15.18	1.98E-09	Compliance	NUREG/CR-4667, Vol. 24, Tbl 17, p. 76
NX9244G	SA 1025°C/2h	J320-01	PWR <1 ppb DO + H_2	320	0.70	25.80	7.74	1.13E-09	Compliance	NUREG/CR-4667, Vol. 24, Tbl 17, p. 76
NX9244G	SA 1025°C/2h	J320-01	PWR <1 ppb DO + H_2	320	0.40	26.20	15.72	1.86E-09	Compliance	NUREG/CR-4667, Vol. 24, Tbl 17, p. 76
NX9244G	SA 1025°C/2h	J320-01	PWR <1 ppb DO + H_2	320	0.60	26.70	10.68	1.04E-09	Compliance	NUREG/CR-4667, Vol. 24, Tbl 17, p. 76
NX9244G	SA 1025°C/2h	J320-01	PWR <1 ppb DO + H_2	320	0.50	27.10	13.55	1.62E-09	Compliance	NUREG/CR-4667, Vol. 24, Tbl 17, p. 76
NX9244G	SA 1025°C/2h	J320-01	PWR <1 ppb DO + H_2	320	0.30	27.60	19.32	2.26E-09	Compliance	NUREG/CR-4667, Vol. 24, Tbl 17, p. 76
NX9244G	SA 1025°C/2h	J320-01	PWR <1 ppb DO + H_2	320	0.80	27.90	5.58	2.63E-10	Compliance	NUREG/CR-4667, Vol. 24, Tbl 17, p. 76
NX9244G	SA 1025°C/2h	J320-01	PWR <1 ppb DO + H_2	320	0.90	28.70	2.87	1.52E-10	Compliance	NUREG/CR-4667, Vol. 24, Tbl 17, p. 76
NX9244G	SA 1025°C/2h	J320-01	PWR <1 ppb DO + H_2	320	0.25	29.10	21.80	2.86E-09	Compliance	NUREG/CR-4667, Vol. 24, Tbl 17, p. 76
NX9244G	SA 1025°C/2h	J320-01	PWR <1 ppb DO + H_2	320	0.75	29.20	7.30	4.15E-10	Compliance	NUREG/CR-4667, Vol. 24, Tbl 17, p. 76
NX9244G	SA 1025°C/2h	J320-01	PWR <1 ppb DO + H_2	320	0.85	29.40	4.41	6.80E-11	Compliance	NUREG/CR-4667, Vol. 24, Tbl 17, p. 76
NX9244G	SA 1025°C/2h	J320-01	PWR <1 ppb DO + H_2	320	0.73	29.90	8.23	5.77E-10	Compliance	NUREG/CR-4667, Vol. 24, Tbl 17, p. 76
NX9244G	SA 1025°C/2h	J320-01	PWR <1 ppb DO + H_2	320	0.20	30.50	24.40	3.87E-09	Compliance	NUREG/CR-4667, Vol. 24, Tbl 17, p. 76
NX9244G	SA 1025°C/2h	J320-01	PWR <1 ppb DO + H_2	320	0.95	34.80	1.74	6.50E-11	Compliance	NUREG/CR-4667, Vol. 24, Tbl 17, p. 76
NX9244G	SA 1025°C/2h	J320-01	PWR 2 ppb DO + H_2	320	0.95	39.60	1.98	1.10E-10	Compliance	NUREG/CR-4667, Vol. 24, Tbl 17, p. 76
NX9244G	SA 1025°C/2h	J320-01	PWR 2 ppb DO + H_2	320	0.95	45.80	2.29	2.27E-10	Compliance	NUREG/CR-4667, Vol. 24, Tbl 17, p. 76
NX9244G	1025°C/2h+600°C/24h	J321-01	PWR <1 ppb DO + H_2	320	0.40	24.40	14.64	1.00E-09	Compliance	NUREG/CR-4667, Vol. 24, Tbl 17, p. 76
NX9244G	1025°C/2h+600°C/24h	J321-01	PWR <1 ppb DO + H_2	320	0.70	24.50	7.35	6.64E-10	Compliance	NUREG/CR-4667, Vol. 24, Tbl 17, p. 76
NX9244G	1025°C/2h+600°C/24h	J321-01	PWR <1 ppb DO + H_2	320	0.40	24.60	14.76	8.09E-10	Compliance	NUREG/CR-4667, Vol. 24, Tbl 17, p. 76
NX9244G	1025°C/2h+600°C/24h	J321-01	PWR <1 ppb DO + H_2	320	0.60	24.70	9.88	2.55E-10	Compliance	NUREG/CR-4667, Vol. 24, Tbl 17, p. 76
NX9244G	1025°C/2h+600°C/24h	J321-01	PWR <1 ppb DO + H_2	320	0.50	24.80	12.40	6.21E-10	Compliance	NUREG/CR-4667, Vol. 24, Tbl 17, p. 76
NX9244G	1025°C/2h+600°C/24h	J321-01	PWR <1 ppb DO + H_2	320	0.30	25.40	17.78	2.54E-09	Compliance	NUREG/CR-4667, Vol. 24, Tbl 17, p. 76
NX9244G	1025°C/2h+600°C/24h	J321-01	PWR <1 ppb DO + H_2	320	0.80	25.50	5.10	1.08E-10	Compliance	NUREG/CR-4667, Vol. 24, Tbl 17, p. 76
NX9244G	1025°C/2h+600°C/24h	J321-01	PWR <1 ppb DO + H_2	320	0.90	26.00	2.60	1.18E-10	Compliance	NUREG/CR-4667, Vol. 24, Tbl 17, p. 76
NX9244G	1025°C/2h+600°C/24h	J321-01	PWR <1 ppb DO + H_2	320	0.25	26.50	19.90	4.71E-09	Compliance	NUREG/CR-4667, Vol. 24, Tbl 17, p. 76
NX9244G	1025°C/2h+600°C/24h	J321-01	PWR <1 ppb DO + H_2	320	0.75	26.50	6.63	1.25E-10	Compliance	NUREG/CR-4667, Vol. 24, Tbl 17, p. 76
NX9244G	1025°C/2h+600°C/24h	J321-01	PWR <1 ppb DO + H_2	320	0.85	26.50	3.98	1.00E-12	Compliance	NUREG/CR-4667, Vol. 24, Tbl 17, p. 76
NX9244G	1025°C/2h+600°C/24h	J321-01	PWR <1 ppb DO + H_2	320	0.73	26.60	7.31	1.15E-10	Compliance	NUREG/CR-4667, Vol. 24, Tbl 17, p. 76
NX9244G	1025°C/2h+600°C/24h	J321-01	PWR <1 ppb DO + H_2	320	0.20	27.40	21.90	7.78E-09	Compliance	NUREG/CR-4667, Vol. 24, Tbl 17, p. 76
NX9244G	1025°C/2h+600°C/24h	J321-01	PWR <1 ppb DO + H_2	320	0.95	31.30	1.56	1.00E-12	Compliance	NUREG/CR-4667, Vol. 24, Tbl 17, p. 76
NX9244G	1025°C/2h+600°C/24h	J321-01	PWR 2 ppb DO + H_2	320	0.95	35.80	1.79	1.00E-12	Compliance	NUREG/CR-4667, Vol. 24, Tbl 17, p. 76
NX9244G	1025°C/2h+600°C/24h	J321-01	PWR 2 ppb DO + H_2	320	0.95	40.30	2.01	2.50E-11	Compliance	NUREG/CR-4667, Vol. 24, Tbl 17, p. 76

Table 17. Contd.

Alloy 600 Heat No.	Heat Treatment Condition	Specimen Number	Test Environment	Temp. [°C]	Load Ratio	Kmax (MPa·m^1/2)	ΔK	CGR (m·s⁻¹)	Crack Length Measurement	NUREG Report, Table, Page No.
NX8197	MA	197-07	HP <5 ppb DO	289	0.20	32.50	26.00	3.67E-09	DCPD	NUREG/CR-6383, Tbl 8, p. 22
NX8197	MA	197-07	HP <5 ppb DO	289	0.60	32.80	13.12	1.04E-09	DCPD	NUREG/CR-6383, Tbl 8, p. 22
NX8197	MA	197-07	HP <5 ppb DO	289	0.90	32.90	3.29	8.00E-12	DCPD	NUREG/CR-6383, Tbl 8, p. 22
NX8197	MA	197-07	HP <5 ppb DO	289	0.90	34.50	3.45	7.00E-11	DCPD	NUREG/CR-6383, Tbl 8, p. 22
NX8197	MA	197-07	HP <5 ppb DO	289	0.60	34.50	13.80	3.29E-10	DCPD	NUREG/CR-6383, Tbl 8, p. 22
NX8197	MA	197-07	HP <5 ppb DO	289	0.20	34.80	27.84	1.14E-08	DCPD	NUREG/CR-6383, Tbl 8, p. 22
NX8197	MA	197-07	HP <5 ppb DO	289	0.90	34.70	3.47	2.60E-11	DCPD	NUREG/CR-6383, Tbl 8, p. 22
NX8197	MA	197-07	HP <5 ppb DO	289	0.60	34.70	13.88	9.60E-11	DCPD	NUREG/CR-6383, Tbl 8, p. 22
NX8197	MA	197-07	HP 6 ppm DO	289	0.20	31.30	25.04	8.68E-09	DCPD	NUREG/CR-6383, Tbl 8, p. 22
NX8197	MA	197-07	HP 6 ppm DO	289	0.60	31.80	12.72	2.80E-09	DCPD	NUREG/CR-6383, Tbl 8, p. 22
NX8197	MA	197-07	HP 6 ppm DO	289	0.90	32.20	3.22	5.20E-10	DCPD	NUREG/CR-6383, Tbl 8, p. 22
NX9244G	SA 1025°C/2h	J320-02	HP ≈300 ppb DO	289	0.45	31.20	17.16	2.33E-09	DCPD	NUREG/CR-4667, Vol. 23, Tbl 17, p. 60
NX9244G	SA 1025°C/2h	J320-02	HP ≈300 ppb DO	289	0.40	31.70	19.02	4.18E-09	DCPD	NUREG/CR-4667, Vol. 23, Tbl 17, p. 60
NX9244G	SA 1025°C/2h	J320-02	HP ≈300 ppb DO	289	0.35	32.30	21.00	5.16E-09	DCPD	NUREG/CR-4667, Vol. 23, Tbl 17, p. 60
NX9244G	SA 1025°C/2h	J320-02	HP ≈300 ppb DO	289	0.30	34.10	23.87	1.18E-08	DCPD	NUREG/CR-4667, Vol. 23, Tbl 17, p. 60
NX9244G	SA 1025°C/2h	J320-02	HP ≈300 ppb DO	289	0.50	34.80	17.40	4.42E-09	DCPD	NUREG/CR-4667, Vol. 23, Tbl 17, p. 60
NX9244G	SA 1025°C/2h	J320-02	HP ≈300 ppb DO	289	0.20	36.20	28.96	1.94E-08	DCPD	NUREG/CR-4667, Vol. 23, Tbl 17, p. 60
NX9244G	SA 1025°C/2h	J320-02	HP ≈300 ppb DO	289	0.60	36.50	14.60	2.67E-09	DCPD	NUREG/CR-4667, Vol. 23, Tbl 17, p. 60
NX9244G	SA 1025°C/2h	J320-02	HP ≈300 ppb DO	289	0.75	36.80	9.20	1.24E-09	DCPD	NUREG/CR-4667, Vol. 23, Tbl 17, p. 60
NX9244G	SA 1025°C/2h	J320-02	HP ≈300 ppb DO	289	0.90	37.00	3.70	1.12E-10	DCPD	NUREG/CR-4667, Vol. 23, Tbl 17, p. 60
NX9244G	SA 1025°C/2h	J320-02	HP ≈300 ppb DO	289	0.95	37.10	1.86	1.00E-11	DCPD	NUREG/CR-4667, Vol. 23, Tbl 17, p. 60
NX9244G	SA 1025°C/2h	J320-02	HP ≈300 ppb DO	289	0.70	37.30	11.19	2.24E-09	DCPD	NUREG/CR-4667, Vol. 23, Tbl 17, p. 60
NX9244G	SA 1025°C/2h	J320-02	HP ≈300 ppb DO	289	0.83	37.50	6.38	5.64E-10	DCPD	NUREG/CR-4667, Vol. 23, Tbl 17, p. 60
NX9244G	SA 1025°C/2h	J320-02	HP ≈300 ppb DO	289	0.20	38.30	30.64	1.41E-08	DCPD	NUREG/CR-4667, Vol. 23, Tbl 17, p. 60
NX9244G	SA 1025°C/2h	J320-02	HP ≈300 ppb DO	289	0.65	39.00	13.65	1.44E-09	DCPD	NUREG/CR-4667, Vol. 23, Tbl 17, p. 60
NX9244G	1025°C/2h+600°C/24h	J321-02	HP ≈300 ppb DO	289	0.45	31.00	17.05	1.26E-09	DCPD	NUREG/CR-4667, Vol. 23, Tbl 17, p. 60
NX9244G	1025°C/2h+600°C/24h	J321-02	HP ≈300 ppb DO	289	0.40	31.20	18.72	1.56E-09	DCPD	NUREG/CR-4667, Vol. 23, Tbl 17, p. 60
NX9244G	1025°C/2h+600°C/24h	J321-02	HP ≈300 ppb DO	289	0.35	31.30	20.35	1.53E-09	DCPD	NUREG/CR-4667, Vol. 23, Tbl 17, p. 60
NX9244G	1025°C/2h+600°C/24h	J321-02	HP ≈300 ppb DO	289	0.30	31.80	22.26	2.72E-09	DCPD	NUREG/CR-4667, Vol. 23, Tbl 17, p. 60
NX9244G	1025°C/2h+600°C/24h	J321-02	HP ≈300 ppb DO	289	0.50	32.00	16.00	1.43E-09	DCPD	NUREG/CR-4667, Vol. 23, Tbl 17, p. 60
NX9244G	1025°C/2h+600°C/24h	J321-02	HP ≈300 ppb DO	289	0.20	32.40	25.92	7.51E-09	DCPD	NUREG/CR-4667, Vol. 23, Tbl 17, p. 60
NX9244G	1025°C/2h+600°C/24h	J321-02	HP ≈300 ppb DO	289	0.60	32.60	13.04	1.20E-09	DCPD	NUREG/CR-4667, Vol. 23, Tbl 17, p. 60
NX9244G	1025°C/2h+600°C/24h	J321-02	HP ≈300 ppb DO	289	0.75	32.70	8.18	7.45E-10	DCPD	NUREG/CR-4667, Vol. 23, Tbl 17, p. 60
NX9244G	1025°C/2h+600°C/24h	J321-02	HP ≈300 ppb DO	289	0.90	32.90	3.29	1.25E-10	DCPD	NUREG/CR-4667, Vol. 23, Tbl 17, p. 60
NX9244G	1025°C/2h+600°C/24h	J321-02	HP ≈300 ppb DO	289	0.95	33.00	1.65	4.80E-11	DCPD	NUREG/CR-4667, Vol. 23, Tbl 17, p. 60
NX9244G	1025°C/2h+600°C/24h	J321-02	HP ≈300 ppb DO	289	0.70	33.20	9.96	1.55E-09	DCPD	NUREG/CR-4667, Vol. 23, Tbl 17, p. 60
NX9244G	1025°C/2h+600°C/24h	J321-02	HP ≈300 ppb DO	289	0.83	33.30	5.66	3.21E-10	DCPD	NUREG/CR-4667, Vol. 23, Tbl 17, p. 60
NX9244G	1025°C/2h+600°C/24h	J321-02	HP ≈300 ppb DO	289	0.20	33.60	26.88	4.98E-09	DCPD	NUREG/CR-4667, Vol. 23, Tbl 17, p. 60
NX9244G	1025°C/2h+600°C/24h	J321-02	HP ≈300 ppb DO	289	0.65	33.80	11.83	9.81E-10	DCPD	NUREG/CR-4667, Vol. 23, Tbl 17, p. 60

Table 17. Contd.

Alloy 600 Heat No.	Heat Treatment Condition	Specimen Number	Test Environment	Temp. (°C)	Load Ratio	Kmax (MPa·m$^{1/2}$)	ΔK	CGR (m·s^{-1})	Crack Length Measurement	NUREG Report, Table, Page No.
NX9244G	SA 1115°C/2h	J310-02	HP ≈300 ppb DO	289	0.50	29.60	14.80	2.29E-09	DCPD	NUREG/CR-4667, Vol. 23, Tbl 18, p. 61
NX9244G	SA 1115°C/2h	J310-02	HP ≈300 ppb DO	289	0.60	30.00	12.00	1.57E-09	DCPD	NUREG/CR-4667, Vol. 23, Tbl 18, p. 61
NX9244G	SA 1115°C/2h	J310-02	HP ≈300 ppb DO	289	0.70	30.40	9.12	9.87E-10	DCPD	NUREG/CR-4667, Vol. 23, Tbl 18, p. 61
NX9244G	SA 1115°C/2h	J310-02	HP ≈300 ppb DO	289	0.75	30.50	7.63	6.34E-10	DCPD	NUREG/CR-4667, Vol. 23, Tbl 18, p. 61
NX9244G	SA 1115°C/2h	J310-02	HP ≈300 ppb DO	289	0.90	31.10	3.11	8.90E-11	DCPD	NUREG/CR-4667, Vol. 23, Tbl 18, p. 61
NX9244G	SA 1115°C/2h	J310-02	HP ≈300 ppb DO	289	0.85	31.20	4.67	1.37E-10	DCPD	NUREG/CR-4667, Vol. 23, Tbl 18, p. 61
NX9244G	SA 1115°C/2h	J310-02	HP ≈300 ppb DO	289	0.80	31.30	6.26	3.05E-10	DCPD	NUREG/CR-4667, Vol. 23, Tbl 18, p. 61
NX9244G	SA 1115°C/2h	J310-02	HP ≈300 ppb DO	289	0.45	31.80	17.49	2.09E-09	DCPD	NUREG/CR-4667, Vol. 23, Tbl 18, p. 61
NX9244G	SA 1115°C/2h	J310-02	HP ≈300 ppb DO	289	0.40	32.40	19.44	3.53E-09	DCPD	NUREG/CR-4667, Vol. 23, Tbl 18, p. 61
NX9244G	SA 1115°C/2h	J310-02	HP ≈300 ppb DO	289	0.35	33.00	21.45	4.63E-09	DCPD	NUREG/CR-4667, Vol. 23, Tbl 18, p. 61
NX9244G	SA 1115°C/2h	J310-02	HP ≈300 ppb DO	289	0.68	33.70	10.78	1.18E-09	DCPD	NUREG/CR-4667, Vol. 23, Tbl 18, p. 61
NX9244G	SA 1115°C/2h	J310-02	HP ≈300 ppb DO	289	0.95	33.80	1.69	7.80E-11	DCPD	NUREG/CR-4667, Vol. 23, Tbl 18, p. 61
NX9244G	SA 1115°C/2h	J310-02	HP ≈300 ppb DO	289	0.30	35.20	24.64	7.88E-09	DCPD	NUREG/CR-4667, Vol. 23, Tbl 18, p. 61
NX9244G	SA 1115°C/2h	J310-02	HP ≈300 ppb DO	289	0.20	36.40	29.12	2.36E-08	DCPD	NUREG/CR-4667, Vol. 23, Tbl 18, p. 61
NX9244G	1115°C/2h+600°C/24h	J311-02	HP ≈300 ppb DO	289	0.50	29.60	14.80	2.24E-09	DCPD	NUREG/CR-4667, Vol. 23, Tbl 18, p. 61
NX9244G	1115°C/2h+600°C/24h	J311-02	HP ≈300 ppb DO	289	0.60	29.90	11.90	1.36E-09	DCPD	NUREG/CR-4667, Vol. 23, Tbl 18, p. 61
NX9244G	1115°C/2h+600°C/24h	J311-02	HP ≈300 ppb DO	289	0.70	30.20	9.07	9.18E-10	DCPD	NUREG/CR-4667, Vol. 23, Tbl 18, p. 61
NX9244G	1115°C/2h+600°C/24h	J311-02	HP ≈300 ppb DO	289	0.75	30.40	7.60	6.07E-10	DCPD	NUREG/CR-4667, Vol. 23, Tbl 18, p. 61
NX9244G	1115°C/2h+600°C/24h	J311-02	HP ≈300 ppb DO	289	0.90	31.00	3.10	8.20E-11	DCPD	NUREG/CR-4667, Vol. 23, Tbl 18, p. 61
NX9244G	1115°C/2h+600°C/24h	J311-02	HP ≈300 ppb DO	289	0.85	31.10	4.67	2.08E-10	DCPD	NUREG/CR-4667, Vol. 23, Tbl 18, p. 61
NX9244G	1115°C/2h+600°C/24h	J311-02	HP ≈300 ppb DO	289	0.80	31.30	6.26	4.18E-10	DCPD	NUREG/CR-4667, Vol. 23, Tbl 18, p. 61
NX9244G	1115°C/2h+600°C/24h	J311-02	HP ≈300 ppb DO	289	0.45	31.60	17.38	1.82E-09	DCPD	NUREG/CR-4667, Vol. 23, Tbl 18, p. 61
NX9244G	1115°C/2h+600°C/24h	J311-02	HP ≈300 ppb DO	289	0.40	32.10	19.26	2.54E-09	DCPD	NUREG/CR-4667, Vol. 23, Tbl 18, p. 61
NX9244G	1115°C/2h+600°C/24h	J311-02	HP ≈300 ppb DO	289	0.35	32.40	21.06	2.53E-09	DCPD	NUREG/CR-4667, Vol. 23, Tbl 18, p. 61
NX9244G	1115°C/2h+600°C/24h	J311-02	HP ≈300 ppb DO	289	0.68	32.70	10.46	6.92E-10	DCPD	NUREG/CR-4667, Vol. 23, Tbl 18, p. 61
NX9244G	1115°C/2h+600°C/24h	J311-02	HP ≈300 ppb DO	289	0.95	32.80	1.64	1.30E-11	DCPD	NUREG/CR-4667, Vol. 23, Tbl 18, p. 61
NX9244G	1115°C/2h+600°C/24h	J311-02	HP ≈300 ppb DO	289	0.30	33.70	23.59	4.63E-09	DCPD	NUREG/CR-4667, Vol. 23, Tbl 18, p. 61
NX9244G	1115°C/2h+600°C/24h	J311-02	HP ≈300 ppb DO	289	0.20	34.40	27.52	1.32E-08	DCPD	NUREG/CR-4667, Vol. 23, Tbl 18, p. 61
NX8844J-26	SA 1038°C/1h	J26-02	PWR <1 ppb DO	289	0.54	30.40	13.98	1.04E-09	Compliance	NUREG/CR-4667, Vol. 24, Tbl 15, p. 73
NX8844J-26	SA 1038°C/1h	J26-02	PWR <1 ppb DO	289	0.50	30.90	15.45	1.80E-09	Compliance	NUREG/CR-4667, Vol. 24, Tbl 15, p. 73
NX8844J-26	SA 1038°C/1h	J26-02	PWR <1 ppb DO	289	0.45	31.80	17.49	3.39E-09	Compliance	NUREG/CR-4667, Vol. 24, Tbl 15, p. 73
NX8844J-26	SA 1038°C/1h	J26-02	PWR <1 ppb DO	289	0.40	32.80	19.68	5.95E-09	Compliance	NUREG/CR-4667, Vol. 24, Tbl 15, p. 73
NX8844J-26	SA 1038°C/1h	J26-02	PWR <1 ppb DO	289	0.35	33.80	21.97	9.29E-09	Compliance	NUREG/CR-4667, Vol. 24, Tbl 15, p. 73
NX8844J-26	SA 1038°C/1h	J26-02	PWR <1 ppb DO	289	0.30	35.30	24.71	1.43E-08	Compliance	NUREG/CR-4667, Vol. 24, Tbl 15, p. 73
NX8844J-26	SA 1038°C/1h	J26-02	PWR <1 ppb DO	289	0.25	36.10	27.08	1.90E-08	Compliance	NUREG/CR-4667, Vol. 24, Tbl 15, p. 73
NX8844J-26	SA 1038°C/1h	J26-02	PWR <1 ppb DO	289	0.20	37.20	29.76	2.55E-08	Compliance	NUREG/CR-4667, Vol. 24, Tbl 15, p. 73
NX8844J-26	SA 1038°C/1h	J26-02	PWR <1 ppb DO	289	0.70	37.40	11.22	6.20E-10	Compliance	NUREG/CR-4667, Vol. 24, Tbl 15, p. 73
NX8844J-26	SA 1038°C/1h	J26-02	PWR <1 ppb DO	289	0.75	37.70	9.43	3.73E-10	Compliance	NUREG/CR-4667, Vol. 24, Tbl 15, p. 73
NX8844J-26	SA 1038°C/1h	J26-02	PWR <1 ppb DO	289	0.80	37.70	7.54	5.00E-12	Compliance	NUREG/CR-4667, Vol. 24, Tbl 15, p. 73
NX8844J-26	SA 1038°C/1h	J26-02	PWR <1 ppb DO	289	0.50	41.50	20.75	8.06E-09	Compliance	NUREG/CR-4667, Vol. 24, Tbl 15, p. 73
NX8844J-26	SA 1038°C/1h	J26-02	PWR <1 ppb DO	289	0.40	42.20	25.32	1.24E-08	Compliance	NUREG/CR-4667, Vol. 24, Tbl 15, p. 73

Table 17. Contd.

Alloy 600 Heat No.	Heat Treatment Condition	Specimen Number	Test Environment	Temp. (°C)	Load Ratio	Kmax (MPa·m^1/2)	ΔK	CGR (m·s^-1)	Crack Length Measurement	NUREG Report, Table, Page No.
J422	MA	IN-1	HP ≈300 ppb DO	289	0.95	28.00	1.40	1.00E-11	DCPD	NUREG/CR-6383, Tbl 6, p. 13
J422	MA	IN-1	HP ≈300 ppb DO	289	0.80	28.10	5.62	7.00E-11	DCPD	NUREG/CR-6383, Tbl 6, p. 13
J422	MA	IN-1	HP ≈300 ppb DO	289	0.60	28.40	11.36	2.70E-09	DCPD	NUREG/CR-6383, Tbl 6, p. 13
J422	MA	IN-1	HP ≈300 ppb DO+imp	289	0.95	28.50	1.43	1.70E-11	DCPD	NUREG/CR-6383, Tbl 6, p. 13
J422	MA	IN-1	HP ≈300 ppb DO+imp	289	0.95	28.70	1.44	7.80E-12	DCPD	NUREG/CR-6383, Tbl 6, p. 13
J422	MA	IN-1	HP ≈300 ppb DO+imp	289	0.95	29.50	1.48	3.40E-10	DCPD	NUREG/CR-6383, Tbl 6, p. 13
J422	MA	IN-1	HP ≈300 ppb DO+imp	289	0.95	30.60	1.53	3.30E-10	DCPD	NUREG/CR-6383, Tbl 6, p. 13
J422	MA	IN-1	HP ≈300 ppb DO+imp	289	0.95	31.30	1.57	2.00E-10	DCPD	NUREG/CR-6383, Tbl 6, p. 13
J422	MA	IN-1	HP ≈300 ppb DO+imp	289	0.95	32.00	1.60	1.50E-10	DCPD	NUREG/CR-6383, Tbl 6, p. 13
J422	MA	IN-1	HP ≈300 ppb DO+imp	289	0.95	33.80	1.69	1.40E-10	DCPD	NUREG/CR-6383, Tbl 6, p. 13
J422	MA	IN-1	HP ≈300 ppb DO+imp	289	0.95	34.60	1.73	1.80E-10	DCPD	NUREG/CR-6383, Tbl 6, p. 13
J422	MA	IN-1	HP ≈300 ppb DO	289	0.95	34.80	1.74	9.00E-11	DCPD	NUREG/CR-6383, Tbl 6, p. 13
J422	MA	IN-1	HP ≈300 ppb DO+imp	289	0.95	35.50	1.78	3.00E-10	DCPD	NUREG/CR-6383, Tbl 6, p. 13
J422	MA	IN-2	HP ≈6 ppm DO	289	0.80	31.70	6.34	2.67E-10	DCPD	NUREG/CR-6383, Tbl 7, p. 17
J422	MA	IN-2	HP ≈6 ppm DO	289	0.50	31.70	15.85	2.37E-10	DCPD	NUREG/CR-6383, Tbl 7, p. 17
J422	MA	IN-2	HP ≈6 ppm DO	289	0.20	33.10	26.48	9.80E-09	DCPD	NUREG/CR-6383, Tbl 7, p. 17
J422	MA	IN-2	HP ≈6 ppm DO	289	0.80	32.70	6.54	5.72E-10	DCPD	NUREG/CR-6383, Tbl 7, p. 17
NX8197	MA	197-09	PWR <2 ppb DO + H_2	289	0.80	32.40	6.48	2.09E-10	Compliance	NUREG/CR-6383, Tbl 9, p. 27
NX8197	MA	197-09	PWR <2 ppb DO + H_2	289	0.80	31.20	6.24	7.30E-11	Compliance	NUREG/CR-6383, Tbl 9, p. 27
NX8197	MA	197-09	PWR <2 ppb DO + H_2	289	0.80	31.40	6.28	2.70E-11	Compliance	NUREG/CR-6383, Tbl 9, p. 27
NX8197	MA	197-09	PWR <2 ppb DO + H_2	289	0.80	31.40	6.28	4.50E-11	Compliance	NUREG/CR-6383, Tbl 9, p. 27
NX8197	MA	197-09	PWR <2 ppb DO + H_2	289	0.80	31.80	6.36	6.80E-11	Compliance	NUREG/CR-6383, Tbl 9, p. 27
NX8197	MA	197-09	PWR <2 ppb DO + H_2	289	0.80	30.30	6.06	2.50E-11	Compliance	NUREG/CR-6383, Tbl 9, p. 27
J422	MA	IN-2	PWR <2 ppb DO + H_2	289	0.90	29.40	2.94	9.60E-11	DCPD	NUREG/CR-6383, Tbl 7, p. 17
J422	MA	IN-2	PWR <2 ppb DO + H_2	289	0.80	30.70	6.14	1.60E-09	DCPD	NUREG/CR-6383, Tbl 7, p. 17
J422	MA	IN-2	PWR <2 ppb DO + H_2	289	0.80	30.70	6.14	3.60E-11	DCPD	NUREG/CR-6383, Tbl 7, p. 17
NX8844J-26	SA 1038°C/1h	J26-01	HP <1ppb DO	240	0.90	44.50	4.45	2.20E-11	DCPD	NUREG/CR-4667, Vol. 22, Tbl 14, p. 60
NX8844J-26	SA 1038°C/1h	J26-01	HP <1ppb DO	240	0.40	48.40	29.04	1.72E-08	DCPD	NUREG/CR-4667, Vol. 22, Tbl 14, p. 60
NX8844J-26	SA 1038°C/1h	J26-01	HP <1ppb DO	240	0.80	48.80	9.76	4.22E-10	DCPD	NUREG/CR-4667, Vol. 22, Tbl 14, p. 60
NX8844J-26	SA 1038°C/1h	J26-01	HP <1ppb DO	240	0.60	49.70	19.88	6.11E-09	DCPD	NUREG/CR-4667, Vol. 22, Tbl 14, p. 60
NX8844J-26	SA 1038°C/1h	J26-01	HP <1ppb DO	240	0.20	52.20	41.76	5.72E-08	DCPD	NUREG/CR-4667, Vol. 22, Tbl 14, p. 60
NX8844J-26	SA 1038°C/1h	J26-01	HP <1ppb DO	240	0.90	56.20	5.62	2.99E-10	DCPD	NUREG/CR-4667, Vol. 22, Tbl 14, p. 60
NX8844J-26	SA 1038°C/1h	J26-03	air	35	0.50	30.60	15.30	9.34E-10	DCPD	NUREG/CR-4667, Vol. 22, Tbl 10, p. 52
NX8844J-26	SA 1038°C/1h	J26-03	air	35	0.45	30.90	17.00	1.14E-09	DCPD	NUREG/CR-4667, Vol. 22, Tbl 10, p. 52
NX8844J-26	SA 1038°C/1h	J26-03	air	35	0.40	31.30	18.78	1.64E-09	DCPD	NUREG/CR-4667, Vol. 22, Tbl 10, p. 52
NX8844J-26	SA 1038°C/1h	J26-03	air	35	0.35	31.60	20.54	2.19E-09	DCPD	NUREG/CR-4667, Vol. 22, Tbl 10, p. 52
NX8844J-26	SA 1038°C/1h	J26-03	air	35	0.30	32.30	22.61	2.84E-09	DCPD	NUREG/CR-4667, Vol. 22, Tbl 10, p. 52
NX8844J-26	SA 1038°C/1h	J26-03	air	35	0.25	32.80	24.60	3.65E-09	DCPD	NUREG/CR-4667, Vol. 22, Tbl 10, p. 52
NX8844J-26	SA 1038°C/1h	J26-03	air	35	0.20	33.00	26.40	4.08E-09	DCPD	NUREG/CR-4667, Vol. 22, Tbl 10, p. 52
NX8844J-26	SA 1038°C/1h	J26-03	air	35	0.55	33.40	15.03	9.97E-10	DCPD	NUREG/CR-4667, Vol. 22, Tbl 10, p. 52

Table 17. Contd.

Alloy 600 Heat No.	Heat Treatment Condition	Specimen Number	Test Environment	Temp. (°C)	Load Ratio	Kmax (MPa·m$^{1/2}$)	ΔK	CGR (m·s^{-1})	Crack Length Measurement	NUREG Report, Table, Page No.
NX8844J-26	SA 1038°C/1h	J26-03	air	35	0.70	34.10	10.23	3.58E-10	DCPD	NUREG/CR-4667, Vol. 22, Tbl 10, p. 52
NX8844J-26	SA 1038°C/1h	J26-03	air	35	0.80	34.30	6.86	1.38E-10	DCPD	NUREG/CR-4667, Vol. 22, Tbl 10, p. 52
NX8844J-26	SA 1038°C/1h	J26-03	air	35	0.65	34.60	12.11	5.68E-10	DCPD	NUREG/CR-4667, Vol. 22, Tbl 10, p. 52
NX8844J-26	SA 1038°C/1h	J26-03	air	35	0.90	34.70	3.47	1.60E-11	DCPD	NUREG/CR-4667, Vol. 22, Tbl 10, p. 52
NX8844J-26	SA 1038°C/1h	J26-03	air	35	0.85	34.80	5.22	5.60E-11	DCPD	NUREG/CR-4667, Vol. 22, Tbl 10, p. 52
NX8844J-26	SA 1038°C/1h	J26-03	air	130	0.60	35.30	14.12	1.06E-09	DCPD	NUREG/CR-4667, Vol. 22, Tbl 11, p. 53
NX8844J-26	SA 1038°C/1h	J26-03	air	130	0.70	35.50	10.65	4.60E-10	DCPD	NUREG/CR-4667, Vol. 22, Tbl 11, p. 53
NX8844J-26	SA 1038°C/1h	J26-03	air	130	0.80	35.50	7.10	1.29E-10	DCPD	NUREG/CR-4667, Vol. 22, Tbl 11, p. 53
NX8844J-26	SA 1038°C/1h	J26-03	air	130	0.90	35.60	3.56	1.10E-11	DCPD	NUREG/CR-4667, Vol. 22, Tbl 11, p. 53
NX8844J-26	SA 1038°C/1h	J26-03	air	130	0.50	35.90	17.95	1.76E-09	DCPD	NUREG/CR-4667, Vol. 22, Tbl 11, p. 53
NX8844J-26	SA 1038°C/1h	J26-03	air	130	0.40	36.30	21.78	2.96E-09	DCPD	NUREG/CR-4667, Vol. 22, Tbl 11, p. 53
NX8844J-26	SA 1038°C/1h	J26-03	air	130	0.30	36.80	25.76	4.88E-09	DCPD	NUREG/CR-4667, Vol. 22, Tbl 11, p. 53
NX8844J-26	SA 1038°C/1h	J26-03	air	130	0.20	37.20	29.76	6.83E-09	DCPD	NUREG/CR-4667, Vol. 22, Tbl 11, p. 53
NX8844J-26	SA 1038°C/1h	J26-03	air	130	0.85	37.50	5.63	9.90E-11	DCPD	NUREG/CR-4667, Vol. 22, Tbl 11, p. 53
NX8197	MA	197-10	air	289	0.20	31.40	25.12	5.88E-09	DCPD	NUREG/CR-4667, Vol. 22, Tbl 12, p. 54
NX8197	MA	197-10	air	289	0.80	31.50	6.30	1.99E-10	DCPD	NUREG/CR-4667, Vol. 22, Tbl 12, p. 54
NX8197	MA	197-10	air	289	0.40	32.20	19.32	3.36E-09	DCPD	NUREG/CR-4667, Vol. 22, Tbl 12, p. 54
NX8197	MA	197-10	air	289	0.90	32.30	3.23	5.00E-12	DCPD	NUREG/CR-4667, Vol. 22, Tbl 12, p. 54
NX8197	MA	197-10	air	289	0.60	40.10	16.04	1.86E-09	DCPD	NUREG/CR-4667, Vol. 22, Tbl 12, p. 54
NX8197	MA	197-10	air	289	0.40	41.40	24.84	7.68E-09	DCPD	NUREG/CR-4667, Vol. 22, Tbl 12, p. 54
NX8197	MA	197-10	air	289	0.20	42.60	34.08	1.88E-08	DCPD	NUREG/CR-4667, Vol. 22, Tbl 12, p. 54
NX8197	MA	197-10	air	289	0.90	42.70	4.27	3.40E-11	DCPD	NUREG/CR-4667, Vol. 22, Tbl 12, p. 54
NX8197	MA	197-10	air	289	0.40	46.80	28.08	1.15E-08	DCPD	NUREG/CR-4667, Vol. 22, Tbl 12, p. 54
NX8197	MA	197-10	air	289	0.60	47.70	19.08	3.21E-09	DCPD	NUREG/CR-4667, Vol. 22, Tbl 12, p. 54
NX8197	MA	197-10	air	289	0.90	47.80	4.78	5.20E-11	DCPD	NUREG/CR-4667, Vol. 22, Tbl 12, p. 54
NX8197	MA	197-10	air	289	0.30	55.60	38.92	1.37E-08	DCPD	NUREG/CR-4667, Vol. 22, Tbl 12, p. 54
NX8197	MA	197-10	air	289	0.90	55.80	5.58	1.12E-10	DCPD	NUREG/CR-4667, Vol. 22, Tbl 12, p. 54
NX8197	MA	197-10	air	289	0.95	55.90	2.80	7.00E-12	DCPD	NUREG/CR-4667, Vol. 22, Tbl 12, p. 54
NX8844B-33	SA 872°C/1h	B33-01	air	320	0.20	26.32	21.06	3.68E-09	DCPD	NUREG/CR-4667, Vol. 25, Tbl 17, p. 58
NX8844B-33	SA 872°C/1h	B33-01	air	320	0.25	26.80	20.10	4.05E-09	DCPD	NUREG/CR-4667, Vol. 25, Tbl 17, p. 58
NX8844B-33	SA 872°C/1h	B33-01	air	320	0.30	27.55	19.29	3.98E-09	DCPD	NUREG/CR-4667, Vol. 25, Tbl 17, p. 58
NX8844B-33	SA 872°C/1h	B33-01	air	320	0.35	28.18	18.32	3.37E-09	DCPD	NUREG/CR-4667, Vol. 25, Tbl 17, p. 58
NX8844B-33	SA 872°C/1h	B33-01	air	320	0.40	28.53	17.12	2.76E-09	DCPD	NUREG/CR-4667, Vol. 25, Tbl 17, p. 58
NX8844B-33	SA 872°C/1h	B33-01	air	320	0.50	28.72	14.36	1.66E-09	DCPD	NUREG/CR-4667, Vol. 25, Tbl 17, p. 58
NX8844B-33	SA 872°C/1h	B33-01	air	320	0.60	28.80	11.52	8.44E-10	DCPD	NUREG/CR-4667, Vol. 25, Tbl 17, p. 58
NX8844B-33	SA 872°C/1h	B33-01	air	320	0.70	28.99	8.70	4.59E-10	DCPD	NUREG/CR-4667, Vol. 25, Tbl 17, p. 58
NX8844B-33	SA 872°C/1h	B33-01	air	320	0.75	29.13	7.28	3.26E-10	DCPD	NUREG/CR-4667, Vol. 25, Tbl 17, p. 58
NX8844B-33	SA 872°C/1h	B33-01	air	320	0.80	29.37	5.87	2.76E-10	DCPD	NUREG/CR-4667, Vol. 25, Tbl 17, p. 58
NX8844B-33	SA 872°C/1h	B33-01	air	320	0.83	29.59	5.03	1.38E-10	DCPD	NUREG/CR-4667, Vol. 25, Tbl 17, p. 58
NX8844B-33	SA 872°C/1h	B33-01	air	320	0.86	29.65	4.15	6.60E-11	DCPD	NUREG/CR-4667, Vol. 25, Tbl 17, p. 58
NX8844B-33	SA 872°C/1h	B33-01	air	320	0.90	29.70	2.97	1.60E-11	DCPD	NUREG/CR-4667, Vol. 25, Tbl 17, p. 58

Table 18. Summary of crack growth rate data for Alloy 690 in air, high-purity, and simulated PWR water at several temperatures between 35 and 320°C

Alloy 690 Heat No.	Heat Treatment Condition	Specimen Number	Test Environment	Temp. (°C)	Load Ratio	K_{max} (MPa $m^{1/2}$)	ΔK	CGR ($m \cdot s^{-1}$)	Crack Length Measurement	NUREG Report, Table, Page No.
NX8662HG-33	MA & TT 715°C/5h	HG-07	HP <5 ppb DO + H_2	320	0.60	33.00	13.20	2.40E-09	DCPD	NUREG/CR-6383, Tbl 8, p. 22
NX8662HG-33	MA & TT 715°C/5h	HG-07	HP <5 ppb DO + H_2	320	0.90	33.10	3.31	2.00E-12	DCPD	NUREG/CR-6383, Tbl 8, p. 22
NX8662HG-33	MA & TT 715°C/5h	HG-07	HP <5 ppb DO + H_2	320	0.90	33.70	3.37	1.10E-11	DCPD	NUREG/CR-6383, Tbl 8, p. 22
NX8662HG-33	MA & TT 715°C/5h	HG-07	HP <5 ppb DO + H_2	320	0.90	33.80	3.38	5.00E-12	DCPD	NUREG/CR-6383, Tbl 8, p. 22
NX8662HG-33	MA & TT 715°C/5h	HG-07	HP <5 ppb DO + H_2	320	0.90	33.70	15.00	5.00E-12	DCPD	NUREG/CR-6383, Tbl 8, p. 22
NX8662HG-33	MA & TT 715°C/5h	HG-07	HP <5 ppb DO + H_2	320	0.60	35.10	14.04	2.30E-09	DCPD	NUREG/CR-6383, Tbl 8, p. 22
NX8662HG-33	MA & TT 715°C/5h	HG-07	HP <5 ppb DO + H_2	320	0.60	37.50	15.00	3.12E-09	DCPD	NUREG/CR-6383, Tbl 8, p. 22
NX8662HG-33	MA & TT 715°C/5h	HG-07	HP 6 ppm DO	320	0.60	33.50	13.40	3.88E-09	DCPD	NUREG/CR-6383, Tbl 8, p. 22
NX8662HG-33	MA & TT 715°C/5h	HG-07	HP 6 ppm DO	320	0.90	33.60	3.36	9.20E-11	DCPD	NUREG/CR-6383, Tbl 8, p. 22
NX8625HG-21	SA & TT 715°C/5h	G21-01	HP <1 ppb DO	320	0.20	30.70	24.56	6.96E-09	DCPD	NUREG/CR-4667, Vol 22, Tbl 14, p. 59
NX8625HG-21	SA & TT 715°C/5h	G21-01	HP <1 ppb DO	320	0.90	30.90	3.09	1.90E-11	DCPD	NUREG/CR-4667, Vol 22, Tbl 14, p. 59
NX8625HG-21	SA & TT 715°C/5h	G21-01	HP <1 ppb DO	320	0.90	45.20	4.52	5.30E-11	DCPD	NUREG/CR-4667, Vol 22, Tbl 14, p. 59
NX8625HG-21	SA & TT 715°C/5h	G21-01	HP <1 ppb DO	320	0.90	61.20	6.12	2.67E-10	DCPD	NUREG/CR-4667, Vol 22, Tbl 14, p. 59
NX8625HG-21	SA & TT 715°C/5h	G21-01	HP <1 ppb DO	320	0.85	63.10	9.47	1.16E-09	DCPD	NUREG/CR-4667, Vol 22, Tbl 14, p. 59
NX8625HG-21	SA & TT 715°C/5h	G21-02	HP <1 ppb DO	320	0.20	30.80	24.64	5.89E-09	DCPD	NUREG/CR-4667, Vol 22, Tbl 13, p. 58
NX8625HG-21	SA & TT 715°C/5h	G21-02	HP <1 ppb DO	320	0.90	31.00	3.10	2.00E-12	DCPD	NUREG/CR-4667, Vol 22, Tbl 13, p. 58
NX8625HG-21	SA & TT 715°C/5h	G21-02	HP <1 ppb DO	320	0.20	38.40	30.72	1.91E-08	DCPD	NUREG/CR-4667, Vol 22, Tbl 13, p. 58
NX8625HG-21	SA & TT 715°C/5h	G21-02	HP <1 ppb DO	320	0.30	40.80	28.56	2.19E-08	DCPD	NUREG/CR-4667, Vol 22, Tbl 13, p. 58
NX8625HG-21	SA & TT 715°C/5h	G21-02	HP <1 ppb DO	320	0.50	42.00	21.00	1.05E-08	DCPD	NUREG/CR-4667, Vol 22, Tbl 13, p. 58
NX8625HG-21	SA & TT 715°C/5h	G21-02	HP <1 ppb DO	320	0.70	43.00	12.90	2.94E-09	DCPD	NUREG/CR-4667, Vol 22, Tbl 13, p. 58
NX8625HG-21	SA & TT 715°C/5h	G21-02	HP <1 ppb DO	320	0.90	43.10	4.31	6.00E-12	DCPD	NUREG/CR-4667, Vol 22, Tbl 13, p. 58
NX8625HG-21	SA & TT 715°C/5h	G21-02	HP <1 ppb DO	320	0.90	60.40	6.04	1.64E-10	DCPD	NUREG/CR-4667, Vol 22, Tbl 13, p. 58
NX8244HK-1A	SA 982°C/1h	K1A-01	HP <1 ppb DO	320	0.20	31.20	24.96	9.54E-09	DCPD	NUREG/CR-4667, Vol 22, Tbl 13, p. 58
NX8244HK-1A	SA 982°C/1h	K1A-01	HP <1 ppb DO	320	0.90	31.30	3.13	7.00E-12	DCPD	NUREG/CR-4667, Vol 22, Tbl 13, p. 58
NX8244HK-1A	SA 982°C/1h	K1A-01	HP <1 ppb DO	320	0.20	38.70	30.96	2.16E-08	DCPD	NUREG/CR-4667, Vol 22, Tbl 13, p. 58
NX8244HK-1A	SA 982°C/1h	K1A-01	HP <1 ppb DO	320	0.30	40.50	28.35	1.84E-08	DCPD	NUREG/CR-4667, Vol 22, Tbl 13, p. 58
NX8244HK-1A	SA 982°C/1h	K1A-01	HP <1 ppb DO	320	0.50	42.90	21.45	9.53E-09	DCPD	NUREG/CR-4667, Vol 22, Tbl 13, p. 58
NX8244HK-1A	SA 982°C/1h	K1A-01	HP <1 ppb DO	320	0.70	43.80	13.14	3.00E-09	DCPD	NUREG/CR-4667, Vol 22, Tbl 13, p. 58
NX8244HK-1A	SA 982°C/1h	K1A-01	HP <1 ppb DO	320	0.90	43.90	4.39	2.00E-11	DCPD	NUREG/CR-4667, Vol 22, Tbl 13, p. 58
NX8244HK-1A	SA 982°C/1h	K1A-01	HP <1 ppb DO	320	0.90	59.10	5.91	1.88E-10	DCPD	NUREG/CR-4667, Vol 22, Tbl 13, p. 58
NX8244HK-1B	SA 1093°C/1h	K1B-01	HP <1 ppb DO	320	0.20	31.00	24.80	8.41E-09	DCPD	NUREG/CR-4667, Vol 22, Tbl 13, p. 58
NX8244HK-1B	SA 1093°C/1h	K1B-01	HP <1 ppb DO	320	0.90	31.70	3.17	4.00E-12	DCPD	NUREG/CR-4667, Vol 22, Tbl 13, p. 58
NX8244HK-1B	SA 1093°C/1h	K1B-01	HP <1 ppb DO	320	0.20	39.40	31.52	2.10E-08	DCPD	NUREG/CR-4667, Vol 22, Tbl 13, p. 58
NX8244HK-1B	SA 1093°C/1h	K1B-01	HP <1 ppb DO	320	0.30	41.00	28.70	1.73E-08	DCPD	NUREG/CR-4667, Vol 22, Tbl 13, p. 58
NX8244HK-1B	SA 1093°C/1h	K1B-01	HP <1 ppb DO	320	0.50	43.70	21.85	9.53E-09	DCPD	NUREG/CR-4667, Vol 22, Tbl 13, p. 58
NX8244HK-1B	SA 1093°C/1h	K1B-01	HP <1 ppb DO	320	0.70	44.50	13.35	2.62E-09	DCPD	NUREG/CR-4667, Vol 22, Tbl 13, p. 58
NX8244HK-1B	SA 1093°C/1h	K1B-01	HP <1 ppb DO	320	0.90	44.60	4.46	3.00E-12	DCPD	NUREG/CR-4667, Vol 22, Tbl 13, p. 58
NX8244HK-1B	SA 1093°C/1h	K1B-01	HP <1 ppb DO	320	0.90	59.20	5.92	1.80E-10	DCPD	NUREG/CR-4667, Vol 22, Tbl 13, p. 58
NX8662HG-33	MA +TT 715°C/5h	HG-09	PWR <2 ppb DO + H_2	320	0.80	31.10	6.26	2.19E-10	Compliance	NUREG/CR-6383, Tbl 9, p. 27
NX8662HG-33	MA +TT 715°C/5h	HG-09	PWR <2 ppb DO + H_2	320	0.80	32.40	6.48	3.25E-10	Compliance	NUREG/CR-6383, Tbl 9, p. 27
NX8662HG-33	MA +TT 715°C/5h	HG-09	PWR <2 ppb DO + H_2	320	0.80	36.90	7.38	3.73E-10	Compliance	NUREG/CR-6383, Tbl 9, p. 27
NX8662HG-33	MA +TT 715°C/5h	HG-09	PWR <2 ppb DO + H_2	320	0.80	38.00	7.60	4.19E-10	Compliance	NUREG/CR-6383, Tbl 9, p. 27
NX8662HG-33	MA +TT 715°C/5h	HG-09	PWR <2 ppb DO + H_2	320	0.80	41.40	8.28	7.51E-10	Compliance	NUREG/CR-6383, Tbl 9, p. 27

Table 18. Contd.

Alloy 690 Heat No.	Heat Treatment Condition	Specimen Number	Test Environment	Temp. (°C)	Load Ratio	K_{max} (MPa·m$^{1/2}$)	ΔK	CGR (m·s^{-1})	Crack Length Measurement	NUREG Report, Table, Page No.
NX8625HG-21	SA & TT 715°C/5h	G21-02	HP <1 ppb DO	289	0.90	43.10	4.31	1.00E-12	DCPD	NUREG/CR-4667, Vol 22, Tbl 13, p. 58
NX8625HG-21	SA & TT 715°C/5h	G21-02	HP <1 ppb DO	289	0.40	53.50	32.10	2.71E-08	DCPD	NUREG/CR-4667, Vol 22, Tbl 13, p. 58
NX8625HG-21	SA & TT 715°C/5h	G21-02	HP <1 ppb DO	289	0.80	54.80	10.96	1.02E-09	DCPD	NUREG/CR-4667, Vol 22, Tbl 13, p. 58
NX8625HG-21	SA & TT 715°C/5h	G21-02	HP <1 ppb DO	289	0.40	59.40	35.64	3.91E-08	DCPD	NUREG/CR-4667, Vol 22, Tbl 13, p. 58
NX8625HG-21	SA & TT 715°C/5h	G21-02	HP <1 ppb DO	289	0.87	62.00	8.06	1.53E-10	DCPD	NUREG/CR-4667, Vol 22, Tbl 13, p. 58
NX8625HG-21	SA & TT 715°C/5h	G21-02	HP <1 ppb DO	289	1.00	62.10	0.00	6.00E-12	DCPD	NUREG/CR-4667, Vol 22, Tbl 13, p. 58
NX8625HG-21	SA & TT 715°C/5h	G21-02	HP <1 ppb DO	289	0.10	68.90	62.01	1.55E-07	DCPD	NUREG/CR-4667, Vol 22, Tbl 13, p. 58
NX8244HK-1A	SA 982°C/1h	K1A-01	HP <1 ppb DO	289	0.90	43.90	4.39	1.00E-12	DCPD	NUREG/CR-4667, Vol 22, Tbl 13, p. 58
NX8244HK-1A	SA 982°C/1h	K1A-01	HP <1 ppb DO	289	0.40	53.40	32.04	3.46E-08	DCPD	NUREG/CR-4667, Vol 22, Tbl 13, p. 58
NX8244HK-1A	SA 982°C/1h	K1A-01	HP <1 ppb DO	289	0.80	54.20	10.84	1.22E-09	DCPD	NUREG/CR-4667, Vol 22, Tbl 13, p. 58
NX8244HK-1A	SA 982°C/1h	K1A-01	HP <1 ppb DO	289	0.40	58.60	35.16	3.26E-08	DCPD	NUREG/CR-4667, Vol 22, Tbl 13, p. 58
NX8244HK-1A	SA 982°C/1h	K1A-01	HP <1 ppb DO	289	0.87	61.20	7.96	4.17E-10	DCPD	NUREG/CR-4667, Vol 22, Tbl 13, p. 58
NX8244HK-1A	SA 982°C/1h	K1A-01	HP <1 ppb DO	289	1.00	61.40	0.00	1.00E-11	DCPD	NUREG/CR-4667, Vol 22, Tbl 13, p. 58
NX8244HK-1A	SA 982°C/1h	K1A-01	HP <1 ppb DO	289	0.10	65.00	58.50	1.23E-07	DCPD	NUREG/CR-4667, Vol 22, Tbl 13, p. 58
NX8244HK-1B	SA 1093°C/1h	K1B-01	HP <1 ppb DO	289	0.90	44.60	4.46	1.00E-12	DCPD	NUREG/CR-4667, Vol 22, Tbl 13, p. 58
NX8244HK-1B	SA 1093°C/1h	K1B-01	HP <1 ppb DO	289	0.40	54.00	32.40	2.55E-08	DCPD	NUREG/CR-4667, Vol 22, Tbl 13, p. 58
NX8244HK-1B	SA 1093°C/1h	K1B-01	HP <1 ppb DO	289	0.80	54.70	10.94	1.11E-09	DCPD	NUREG/CR-4667, Vol 22, Tbl 13, p. 58
NX8244HK-1B	SA 1093°C/1h	K1B-01	HP <1 ppb DO	289	0.40	58.80	35.28	3.12E-08	DCPD	NUREG/CR-4667, Vol 22, Tbl 13, p. 58
NX8244HK-1B	SA 1093°C/1h	K1B-01	HP <1 ppb DO	289	0.87	60.30	7.84	3.52E-10	DCPD	NUREG/CR-4667, Vol 22, Tbl 13, p. 58
NX8244HK-1B	SA 1093°C/1h	K1B-01	HP <1 ppb DO	289	1.00	60.50	0.00	1.10E-11	DCPD	NUREG/CR-4667, Vol 22, Tbl 13, p. 58
NX8244HK-1B	SA 1093°C/1h	K1B-01	HP <1 ppb DO	289	0.10	62.90	56.61	8.99E-08	DCPD	NUREG/CR-4667, Vol 22, Tbl 13, p. 58
NX8662HG-33	MA & TT 715°C/5h	HG-07	HP <5 ppb DO + H_2	289	0.20	32.20	25.76	9.83E-09	DCPD	NUREG/CR-6383, Tbl 8, p. 22
NX8662HG-33	MA & TT 715°C/5h	HG-07	HP <5 ppb DO + H_2	289	0.60	32.50	13.00	1.72E-09	DCPD	NUREG/CR-6383, Tbl 8, p. 22
NX8662HG-33	MA & TT 715°C/5h	HG-07	HP <5 ppb DO + H_2	289	0.90	32.60	3.26	6.00E-12	DCPD	NUREG/CR-6383, Tbl 8, p. 22
NX8662HG-33	MA & TT 715°C/5h	HG-07	HP <5 ppb DO + H_2	289	0.60	37.90	15.16	2.36E-09	DCPD	NUREG/CR-6383, Tbl 8, p. 22
NX8662HG-33	MA & TT 715°C/5h	HG-07	HP <5 ppb DO + H_2	289	0.20	38.60	30.88	1.57E-08	DCPD	NUREG/CR-6383, Tbl 8, p. 22
NX8662HG-33	MA & TT 715°C/5h	HG-07	HP <5 ppb DO + H_2	289	0.90	39.00	3.90	1.70E-11	DCPD	NUREG/CR-6383, Tbl 8, p. 22
NX8662HG-33	MA & TT 715°C/5h	HG-07	HP <5 ppb DO + H_2	289	0.60	39.20	15.68	1.61E-09	DCPD	NUREG/CR-6383, Tbl 8, p. 22
NX8662HG-33	MA & TT 715°C/5h	HG-07	HP 6 ppm DO	289	0.20	31.00	24.80	7.63E-09	DCPD	NUREG/CR-6383, Tbl 8, p. 22
NX8662HG-33	MA & TT 715°C/5h	HG-07	HP 6 ppm DO	289	0.90	31.40	12.56	2.47E-09	DCPD	NUREG/CR-6383, Tbl 8, p. 22
NX8662HG-33	MA & TT 715°C/5h	HG-07	HP 6 ppm DO	289	0.60	31.60	3.16	8.20E-11	DCPD	NUREG/CR-6383, Tbl 8, p. 22
NX8662HG-33	MA +TT 715°C/5h	HG-09	PWR <2 ppb DO + H_2	289	0.80	30.70	6.14	1.29E-10	Compliance	NUREG/CR-6383, Tbl 9, p. 27
NX8662HG-33	MA +TT 715°C/5h	HG-09	PWR <2 ppb DO + H_2	289	0.80	33.00	6.60	2.20E-10	Compliance	NUREG/CR-6383, Tbl 9, p. 27
NX8662HG-33	MA +TT 715°C/5h	HG-09	PWR <2 ppb DO + H_2	289	0.80	33.90	6.78	2.30E-10	Compliance	NUREG/CR-6383, Tbl 9, p. 27
NX8662HG-33	MA +TT 715°C/5h	HG-09	PWR <2 ppb DO + H_2	289	0.80	34.30	6.86	2.51E-10	Compliance	NUREG/CR-6383, Tbl 9, p. 27
NX8662HG-33	MA +TT 715°C/5h	HG-09	PWR <2 ppb DO + H_2	289	0.80	35.70	7.14	3.93E-10	Compliance	NUREG/CR-6383, Tbl 9, p. 27
NX8662HG-33	MA +TT 715°C/5h	HG-09	PWR <2 ppb DO + H_2	289	0.80	38.60	7.72	2.18E-10	Compliance	NUREG/CR-6383, Tbl 9, p. 27
NX8662HG-33	MA +TT 715°C/5h	HG-09	PWR <2 ppb DO + H_2	289	0.80	39.90	7.98	5.39E-10	Compliance	NUREG/CR-6383, Tbl 9, p. 27
NX8244HK-1B	SA 1093°C/1h	K1B-02	PWR <1 ppb DO	289	0.54	31.30	14.40	2.29E-09	Compliance	NUREG/CR-4667, Vol 24, Tbl 15, p. 72
NX8244HK-1B	SA 1093°C/1h	K1B-02	PWR <1 ppb DO	289	0.50	32.50	16.25	3.52E-09	Compliance	NUREG/CR-4667, Vol 24, Tbl 15, p. 72
NX8244HK-1B	SA 1093°C/1h	K1B-02	PWR <1 ppb DO	289	0.45	33.90	18.65	4.97E-09	Compliance	NUREG/CR-4667, Vol 24, Tbl 15, p. 72
NX8244HK-1B	SA 1093°C/1h	K1B-02	PWR <1 ppb DO	289	0.40	35.00	21.00	6.94E-09	Compliance	NUREG/CR-4667, Vol 24, Tbl 15, p. 72

Table 18. Contd.

Alloy 690 Heat No.	Heat Treatment Condition	Specimen Number	Test Environment	Temp. (°C)	Load Ratio	K_{max} (MPa·m$^{1/2}$)	ΔK	CGR (m·s^{-1})	Crack Length Measurement	NUREG Report, Table, Page No.
NX8244HK-1B	SA 1093°C/1h	K1B-02	PWR <1 ppb DO	289	0.35	36.00	23.40	9.38E-09	Compliance	NUREG/CR-4667, Vol 24, Tbl 15, p. 72
NX8244HK-1B	SA 1093°C/1h	K1B-02	PWR <1 ppb DO	289	0.30	37.40	26.18	1.27E-08	Compliance	NUREG/CR-4667, Vol 24, Tbl 15, p. 72
NX8244HK-1B	SA 1093°C/1h	K1B-02	PWR <1 ppb DO	289	0.25	38.20	28.61	1.68E-08	Compliance	NUREG/CR-4667, Vol 24, Tbl 15, p. 72
NX8244HK-1B	SA 1093°C/1h	K1B-02	PWR <1 ppb DO	289	0.20	39.10	31.27	2.25E-08	Compliance	NUREG/CR-4667, Vol 24, Tbl 15, p. 72
NX8244HK-1B	SA 1093°C/1h	K1B-02	PWR <1 ppb DO	289	0.70	39.90	11.97	1.63E-09	Compliance	NUREG/CR-4667, Vol 24, Tbl 15, p. 72
NX8244HK-1B	SA 1093°C/1h	K1B-02	PWR <1 ppb DO	289	0.75	40.60	10.15	1.17E-09	Compliance	NUREG/CR-4667, Vol 24, Tbl 15, p. 72
NX8244HK-1B	SA 1093°C/1h	K1B-02	PWR <1 ppb DO	289	0.80	40.60	8.12	5.00E-12	Compliance	NUREG/CR-4667, Vol 24, Tbl 15, p. 72
NX8244HK-1B	SA 1093°C/1h	K1B-02	PWR <1 ppb DO	289	0.50	46.30	23.15	9.40E-09	Compliance	NUREG/CR-4667, Vol 24, Tbl 15, p. 72
NX8244HK-1B	SA 1093°C/1h	K1B-02	PWR <1 ppb DO	289	0.40	47.30	28.38	1.38E-08	Compliance	NUREG/CR-4667, Vol 24, Tbl 15, p. 72
NX8625HG-21	SA & TT 715°C/5h	G21-01	HP <1 ppb DO	240	0.90	44.60	4.46	2.70E-11	DCPD	NUREG/CR-4667, Vol 22, Tbl 14, p. 59
NX8625HG-21	SA & TT 715°C/5h	G21-01	HP <1 ppb DO	240	0.40	47.70	28.62	1.34E-08	DCPD	NUREG/CR-4667, Vol 22, Tbl 14, p. 59
NX8625HG-21	SA & TT 715°C/5h	G21-01	HP <1 ppb DO	240	0.80	48.10	9.62	6.80E-10	DCPD	NUREG/CR-4667, Vol 22, Tbl 14, p. 59
NX8625HG-21	SA & TT 715°C/5h	G21-01	HP <1 ppb DO	240	0.60	48.90	19.56	5.11E-09	DCPD	NUREG/CR-4667, Vol 22, Tbl 14, p. 59
NX8625HG-21	SA & TT 715°C/5h	G21-01	HP <1 ppb DO	240	0.20	55.60	44.48	4.44E-08	DCPD	NUREG/CR-4667, Vol 22, Tbl 14, p. 59
NX8625HG-21	SA & TT 715°C/5h	G21-01	HP <1 ppb DO	240	0.90	60.70	6.07	7.00E-11	DCPD	NUREG/CR-4667, Vol 22, Tbl 14, p. 59
NX8244HK-1B	SA 1093°C/1h	K1B-03	air	35	0.50	30.50	15.25	1.05E-09	DCPD	NUREG/CR-4667, Vol 22, Tbl 10, p. 52
NX8244HK-1B	SA 1093°C/1h	K1B-03	air	35	0.45	30.90	17.00	1.34E-09	DCPL	NUREG/CR-4667, Vol 22, Tbl 10, p. 52
NX8244HK-1B	SA 1093°C/1h	K1B-03	air	35	0.40	31.30	18.78	1.55E-09	DCPD	NUREG/CR-4667, Vol 22, Tbl 10, p. 52
NX8244HK-1B	SA 1093°C/1h	K1B-03	air	35	0.35	31.60	20.54	2.18E-09	DCPD	NUREG/CR-4667, Vol 22, Tbl 10, p. 52
NX8244HK-1B	SA 1093°C/1h	K1B-03	air	35	0.30	32.50	22.75	3.81E-09	DCPD	NUREG/CR-4667, Vol 22, Tbl 10, p. 52
NX8244HK-1B	SA 1093°C/1h	K1B-03	air	35	0.25	33.30	24.98	5.67E-09	DCPD	NUREG/CR-4667, Vol 22, Tbl 10, p. 52
NX8244HK-1B	SA 1093°C/1h	K1B-03	air	35	0.20	33.70	26.96	8.30E-09	DCPD	NUREG/CR-4667, Vol 22, Tbl 10, p. 52
NX8244HK-1B	SA 1093°C/1h	K1B-03	air	35	0.55	34.50	15.53	1.53E-09	DCPD	NUREG/CR-4667, Vol 22, Tbl 10, p. 52
NX8244HK-1B	SA 1093°C/1h	K1B-03	air	35	0.70	35.40	10.62	4.90E-10	DCPD	NUREG/CR-4667, Vol 22, Tbl 10, p. 52
NX8244HK-1B	SA 1093°C/1h	K1B-03	air	35	0.80	35.60	7.12	2.05E-10	DCPD	NUREG/CR-4667, Vol 22, Tbl 10, p. 52
NX8244HK-1B	SA 1093°C/1h	K1B-03	air	35	0.65	36.10	12.63	8.04E-10	DCPD	NUREG/CR-4667, Vol 22, Tbl 10, p. 52
NX8244HK-1B	SA 1093°C/1h	K1B-03	air	35	0.90	36.10	3.61	1.20E-11	DCPD	NUREG/CR-4667, Vol 22, Tbl 10, p. 52
NX8244HK-1B	SA 1093°C/1h	K1B-03	air	35	0.85	36.90	5.53	6.90E-11	DCPD	NUREG/CR-4667, Vol 22, Tbl 10, p. 52
NX8244HK-1B	SA 1093°C/1h	K1B-03	air	130	0.60	37.80	15.14	1.58E-09	DCPD	NUREG/CR-4667, Vol 22, Tbl 11, p. 53
NX8244HK-1B	SA 1093°C/1h	K1B-03	air	130	0.70	38.10	11.42	7.06E-10	DCPD	NUREG/CR-4667, Vol 22, Tbl 11, p. 53
NX8244HK-1B	SA 1093°C/1h	K1B-03	air	130	0.80	38.20	7.65	2.39E-10	DCPD	NUREG/CR-4667, Vol 22, Tbl 11, p. 53
NX8244HK-1B	SA 1093°C/1h	K1B-03	air	130	0.90	38.30	3.83	1.70E-11	DCPD	NUREG/CR-4667, Vol 22, Tbl 11, p. 53
NX8244HK-1B	SA 1093°C/1h	K1B-03	air	130	0.50	38.70	19.37	1.99E-09	DCPD	NUREG/CR-4667, Vol 22, Tbl 11, p. 53
NX8244HK-1B	SA 1093°C/1h	K1B-03	air	130	0.40	39.40	23.63	4.32E-09	DCPD	NUREG/CR-4667, Vol 22, Tbl 11, p. 53
NX8244HK-1B	SA 1093°C/1h	K1B-03	air	130	0.30	40.40	28.26	8.29E-09	DCPD	NUREG/CR-4667, Vol 22, Tbl 11, p. 53
NX8244HK-1B	SA 1093°C/1h	K1B-03	air	130	0.20	41.20	32.97	1.34E-08	DCPD	NUREG/CR-4667, Vol 22, Tbl 11, p. 53
NX8244HK-1B	SA 1093°C/1h	K1B-03	air	130	0.85	41.80	6.27	1.72E-10	DCPD	NUREG/CR-4667, Vol 22, Tbl 11, p. 53
NX8662HG-33	MA +TT 715°C/5h	HG-10	air	289	0.20	31.70	25.36	8.39E-09	DCPD	NUREG/CR-4667, Vol 22, Tbl 12, p. 54
NX8662HG-33	MA +TT 715°C/5h	HG-10	air	289	0.80	31.90	6.38	2.74E-10	DCPD	NUREG/CR-4667, Vol 22, Tbl 12, p. 54
NX8662HG-33	MA +TT 715°C/5h	HG-10	air	289	0.40	32.90	19.74	4.68E-09	DCPD	NUREG/CR-4667, Vol 22, Tbl 12, p. 54
NX8662HG-33	MA +TT 715°C/5h	HG-10	air	289	0.90	32.90	3.29	2.00E-12	DCPD	NUREG/CR-4667, Vol 22, Tbl 12, p. 54
NX8662HG-33	MA +TT 715°C/5h	HG-10	air	289	0.60	41.30	16.52	2.85E-09	DCPD	NUREG/CR-4667, Vol 22, Tbl 12, p. 54
NX8662HG-33	MA +TT 715°C/5h	HG-10	air	289	0.40	43.10	25.86	1.07E-08	DCPD	NUREG/CR-4667, Vol 22, Tbl 12, p. 54
NX8662HG-33	MA +TT 715°C/5h	HG-10	air	289	0.20	45.30	36.24	2.81E-08	DCPD	NUREG/CR-4667, Vol 22, Tbl 12, p. 54
NX8662HG-33	MA +TT 715°C/5h	HG-10	air	289	0.90	45.40	4.54	5.50E-11	DCPD	NUREG/CR-4667, Vol 22, Tbl 12, p. 54

Table 18. Contd.

Alloy 690 Heat No.	Heat Treatment Condition	Specimen Number	Test Environment	Temp. (°C)	Load Ratio	K_{max} (MPa·m$^{1/2}$)	ΔK	CGR (m·s^{-1})	Crack Length Measurement	NUREG Report, Table, Page No.
NX8662HG-33	MA +TT 715°C/5h	HG-10	air	289	0.40	53.00	31.80	1.94E-08	DCPD	NUREG/CR-4667, Vol 22, Tbl 12, p. 54
NX8662HG-33	MA +TT 715°C/5h	HG-10	air	289	0.60	55.00	22.00	6.16E-09	DCPD	NUREG/CR-4667, Vol 22, Tbl 12, p. 54
NX8662HG-33	MA +TT 715°C/5h	HG-10	air	289	0.90	55.20	5.52	1.21E-10	DCPD	NUREG/CR-4667, Vol 22, Tbl 12, p. 54
NX8662HG-33	MA +TT 715°C/5h	HG-10	air	289	0.30	67.90	47.53	5.53E-08	DCPD	NUREG/CR-4667, Vol 22, Tbl 12, p. 54
NX8662HG-33	MA +TT 715°C/5h	HG-10	air	289	0.90	68.60	6.86	2.02E-10	DCPD	NUREG/CR-4667, Vol 22, Tbl 12, p. 54
NX8662HG-33	MA +TT 715°C/5h	HG-10	air	289	0.95	68.60	3.43	8.00E-12	DCPD	NUREG/CR-4667, Vol 22, Tbl 12, p. 54
NX8244HK-1A	SA 982°C/1h	K1A-02	air	320	0.20	26.86	21.49	5.07E-09	DCPD	NUREG/CR-4667, Vol 25, Tbl 18, p. 57
NX8244HK-1A	SA 982°C/1h	K1A-02	air	320	0.25	27.55	20.66	5.75E-09	DCPD	NUREG/CR-4667, Vol 25, Tbl 18, p. 57
NX8244HK-1A	SA 982°C/1h	K1A-02	air	320	0.30	28.78	20.15	5.70E-09	DCPD	NUREG/CR-4667, Vol 25, Tbl 18, p. 57
NX8244HK-1A	SA 982°C/1h	K1A-02	air	320	0.35	29.80	19.37	5.58E-09	DCPD	NUREG/CR-4667, Vol 25, Tbl 18, p. 57
NX8244HK-1A	SA 982°C/1h	K1A-02	air	320	0.40	30.54	18.32	5.07E-09	DCPD	NUREG/CR-4667, Vol 25, Tbl 18, p. 57
NX8244HK-1A	SA 982°C/1h	K1A-02	air	320	0.50	30.87	15.44	3.21E-09	DCPD	NUREG/CR-4667, Vol 25, Tbl 18, p. 57
NX8244HK-1A	SA 982°C/1h	K1A-02	air	320	0.60	31.10	12.44	1.69E-09	DCPD	NUREG/CR-4667, Vol 25, Tbl 18, p. 57
NX8244HK-1A	SA 982°C/1h	K1A-02	air	320	0.70	31.47	9.44	8.82E-10	DCPD	NUREG/CR-4667, Vol 25, Tbl 18, p. 57
NX8244HK-1A	SA 982°C/1h	K1A-02	air	320	0.75	31.73	7.93	4.86E-10	DCPD	NUREG/CR-4667, Vol 25, Tbl 18, p. 57
NX8244HK-1A	SA 982°C/1h	K1A-02	air	320	0.80	32.02	6.48	2.93E-10	DCPD	NUREG/CR-4667, Vol 25, Tbl 18, p. 57
NX8244HK-1A	SA 982°C/1h	K1A-02	air	320	0.83	32.18	5.47	8.90E-11	DCPD	NUREG/CR-4667, Vol 25, Tbl 18, p. 57
NX8244HK-1A	SA 982°C/1h	K1A-02	air	320	0.86	32.18	4.50	5.00E-12	DCPD	NUREG/CR-4667, Vol 25, Tbl 18, p. 57
NX8244HK-1A	SA 982°C/1h	K1A-02	air	320	0.90	32.18	3.22	2.00E-12	DCPD	NUREG/CR-4667, Vol 25, Tbl 18, p. 57

4.4.2 Crack Growth Relationships

Because the cyclic stress ratio R has a significant influence on CGRs in association with K_{max} and environmental variables, several correction factors to treat stress ratio effects on CGRs in Eq. 1 were explored; namely, those used by James and Jones,[56] Bamford et al.,[57] Walker,[58,59] Bernard and Slama,[60] and Rabbe and Lieurade[61] for other combinations of alloy composition, temperature, and environment. The correction factors in the CGR relations have various forms, such as (a + bR) for different regions of R < 0.79 and 0.70 < R < 1.0 (James and Jones), $(a - R)^p$ (Bamford et al.), $1/(1 - R)^{n/(1-p)}$ (Walker), $[1/(1 - 0.05 \cdot R^2)]^4$ (Bernard and Slama), and $[1/(1 - R/b)]^p$ (Rabbe and Lieurade). More complex dependencies on R and ΔK have also been used.[62-64] In general, fits to the experimental data in water were less satisfactory with the other simple correction factors than with the R-dependence in Eq. 12. Crack growth data in air were fit to Eq. 13. The last factor in Eq. 12, which accounts for the combined effect of DO in water and R, was deleted in Eq. 13.

$$CGR_{water} = A(1/T_r) \cdot (1 - b \cdot R)^p \cdot (\Delta K)^n \cdot \left[1 + (DO)^m \cdot e^{-15(1-R)}\right] \quad m \cdot s^{-1} \quad (12)$$

$$CGR_{air} = A(1/T_r) \cdot (1 - b \cdot R)^p \cdot (\Delta K)^n \quad m \cdot s^{-1} \quad (13)$$

The best-fit constants in Eqs. 12 and 13 for CGR data for Alloys 600 and 690 in high-purity and simulated PWR water and in air, respectively, are given in Table 16, where T_r is the rise time in seconds of the loading waveform, K is the stress intensity in $MPa \cdot m^{1/2}$, $R = K_{min}/K_{max}$, ΔK is $K_{max}(1 - R)$, and DO is dissolved-oxygen concentration in water in parts per billion (ppb). Equations 12 and 13 and the constants in Table 19 for CGRs in water and air are valid for R values ≤0.95 or ΔK values ≈>2. Thus, extrapolation of the CGRs to higher R values near constant load (i.e., R ≈ 1.0) is not possible because the factor $(1 - b \cdot R)^p$ becomes negative. Furthermore, Eqs. 12 and 13 assume that the CGRs are inversely proportional to T_r in both air and water. Because our tests were conducted at a T_r of 12 s in both environments, these equations can be used directly to compare CGRs in the two environments. However, extrapolation of CGRs based on Eq. 12 to other rise times could lead to incorrect values because CGRs in water often exhibit a power-law dependence on T_r, e.g., $CGR_{water} \approx (1/T_r)^q$, where q is <1. A value of q of ≤0.5 rather than 1.0, for example, would increase the predicted CGR by a factor of 10 for a T_r of 100 s. Because T_r was not varied in the experiments reported here, the variation of CGR with T_r, i.e, a value for q, cannot be determined by statistical analysis of the data using an equation of the form of Eq. 12. An analysis that accounts for the variation of the CGR with T_r will be presented in the next semiannual report.

Table 19. Constants in CGR equations for Alloys 600 and 690 in air and high-purity and simulated PWR water

Alloy	Environment	A (m s^{-1})	b	p	n	m
600	Air[a]	1.644 x 10^{-13}	0.820	-1.739	3.80	-
690	Air[a]	2.227 x 10^{-13}	0.833	-1.507	3.80	-
600 and 690	Air[a]	1.915 x 10^{-13}	0.827	-1.618	3.80	-
600 (Annealed)	HP and PWR water	3.806 x 10^{-13}	1.033	-0.687	3.80	0.474
600 (Low-C)	HP and PWR water	2.244 x 10^{-13}	1.033	-1.456	3.80	0
600 (All heats)	HP and PWR water	2.701 x 10^{-13}	1.033	-1.172	3.80	0.346
690	HP and PWR water	4.321 x 10^{-12}	1.033	-0.170	3.20	0.193

[a]Data from recent tests in air at 320°C were not included in the analysis.

4.4.3 Statistical Analysis of Data

Parameters that indicate the goodness-of-fit of the experimental data to Eqs. 12 and 13 are given in Table 20, namely, the population variance, model variance, and r-square. The population variance σ^2 indicates the spread of the experimental data, the model variance τ^2 is the average-squared deviation of the predicted from the mean of the experimental CGRs, and the coefficient of determination r^2 is a measure of the predictive accuracy or closeness-of-fit of Eqs. 12 and 13 to the data. These parameters were determined for the natural logarithms of the experimental and predicted CGRs given by Eqs. 14-16, respectively:

$$\sigma^2 = \Sigma(Y_i - \mu)^2 / N, \tag{14}$$

$$\tau^2 = \Sigma(\hat{Y}_i - Y_i)^2 / N, \tag{15}$$

and

$$r^2 = 1 - \Sigma(Y_i - \hat{Y}_i)^2 / \Sigma(Y_i - \mu)^2, \tag{16}$$

where Y_i and $\hat{Y}_i$ are $\ln(CGR_{Expt})$ and $\ln(CGR_{Pred})$, respectively, μ is $\Sigma(Y_i)/N$, and N is the number of data points in each set.

Table 20. Number of data points, parameters for goodness-of-fit to Eq. 12, and Weibull distribution constants for Alloys 600 and 690 in water and air environments

Alloy	Environment	Data N	Population Variance	Model Variance	r-Square	Weibull α	Weibull Slope β
600	Air[a]	34	4.035	0.065	0.984	1.1286	4.2036
690	Air[a]	34	4.361	0.089	0.980	1.1501	3.9509
600 and 690	Air[a]	68	4.178	0.086	0.979	1.1473	3.8111
600 (Annealed)	HP and PWR water	46	4.687	0.360	0.923	1.3383	1.8289
600 (Low-C)	HP and PWR water	110	2.068	0.291	0.859	1.2821	1.6728
600 (All heats)	HP and PWR water	156	2.821	0.406	0.856	1.3875	1.5185
690	HP and PWR water	79	3.962	0.148	0.963	1.2125	2.3736

[a]Data from recent tests in air at 320°C were not included in the analysis.

Another quantitative measure of goodness-of-fit of the experimental data to Eqs. 12 and 13 is given by the cumulative distribution of the errors as measured by the exponential of the residuals, i.e.,

$$\exp[\ln(CGR_{Pred}/CGR_{Expt})] = CGR_{Pred}/CGR_{Expt}. \tag{17}$$

The observed cumulative distributions for each data set were compared with log normal and Weibull distributions. The latter exhibited the best fit to the data, although the log normal distribution also gave an acceptable fit. The Weibull probability density function is given by[65]

$$f(x) = \frac{\beta}{\alpha}\left(\frac{x}{\alpha}\right)^{\beta-1} \cdot \exp\left[-\left(\frac{x}{\alpha}\right)^{\beta}\right], x > 0 \tag{18}$$

and the cumulative distribution function is obtained by integrating Eq. 18 from $-\infty$ to x to obtain the area under the density function to the left of the arbitrary point x. The cumulative distribution function is

$$F(x) = 1 - \exp\left[-\left(\frac{x}{\alpha}\right)^{\beta}\right], \quad x > 0, \tag{19}$$

where x is CGR_{Pred}/CGR_{Expt}.

Figures 45-47 show the cumulative probability F(x) from Eq. 19 versus the ratio of the predicted and experimental CGRs for Alloys 600 and 690 in air and water environments. The results in air for Alloys 600 and 690 and the combined data for both alloys in Fig. 45 indicate that the predicted CGRs are within a factor of <2 of the experimental values. Similarly, for Alloys 600 and 690 in aqueous environments (Figs. 46 and 47, respectively), the predicted CGRs are within a factor of <4 of the experimental values.

Equation 19 can be used to obtain the P_{th} percentile of the Weibull distribution, Q_P, for the case where $F(Q_P) = P/100$ and Q_P becomes

$$Q_P = \alpha\left[-\ln\left(1 - \frac{P}{100}\right)\right]^{\frac{1}{\beta}}. \tag{20}$$

The factor Q_P can be applied to Eqs. 12 and 13 to obtain the upper and lower bound (e.g., 95 and 5% percentile) and the mean (50% percentile) values for CGRs based on the constants in Table 18 for the various data sets.

4.4.4 Predicted versus Experimental Crack Growth Rates

The predicted versus experimental CGRs for Alloys 600 and 690 from the combined data for both alloys in air are shown in Figs. 48. Figure 49 shows the residual error $\hat{Y}_i - Y_i$, i.e., ln CGR_{Pred} - ln CGR_{Expt} or $\ln(CGR_{Pred})/(CGR_{Expt})$, for Alloys 600 and 690 in air as a function of load ratio, temperature, and heat and heat-treatment condition. These plots provide a comparison of predicted versus experimental CGRs. For example, a residual value of +1 and -1 indicates that the predicted CGR is higher and lower, respectively, than the experimental CGR by a factor of ≈2.7. Most of the data in the figures fall well within this range of residual values. The rather uniform distribution of residual values for the above variables indicates that their effects have been adequately accounted for in the analysis (load ratio) or that they have a negligible effect on the CGRs (temperature and heat/heat-treatment condition) for the range of conditions in these experiments.

Figures 50 and 51 show the predicted versus experimental CGRs and the residual errors as a function of load ratio, temperature, heat and heat-treatment condition, and DO for Alloy 600 that contains ≈0.06% carbon in high-purity water and simulated PWR environments. The results for three heats of Alloy 600 with ≈0.6% carbon in the annealed condition exhibit somewhat higher variability than the CGR data obtained in air, although the correlations adequately account for the effect of load ratio and DO concentation in high-purity water (1-7500 ppb). The range of the residual values is the same for temperatures of 240, 289, and 320°C, as well as for the three heats of material identified by codes 1-3 in Table 12, which indicates that the CGRs are independent of temperature and any differences in the composition and properties of these heats of Alloy 600.

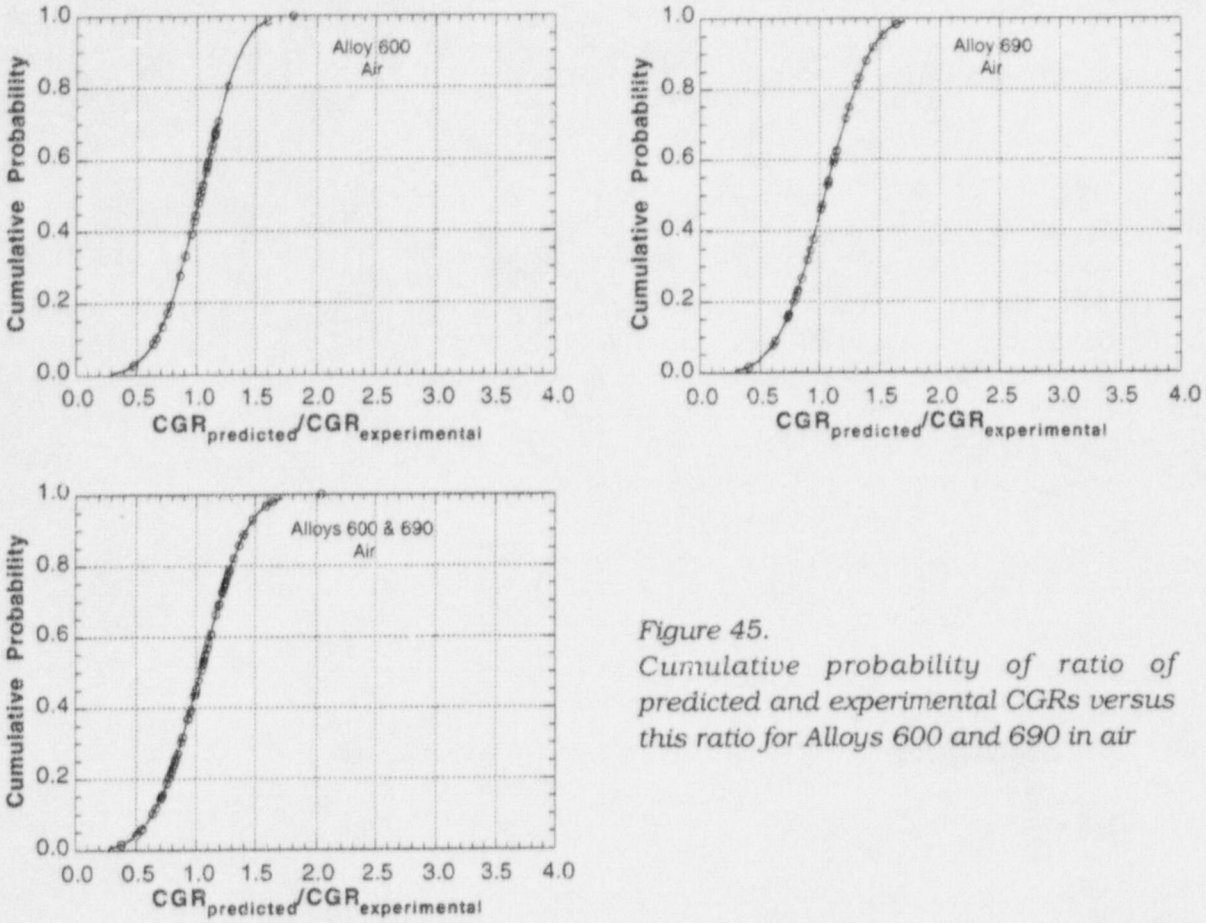

Figure 45.
Cumulative probability of ratio of predicted and experimental CGRs versus this ratio for Alloys 600 and 690 in air

Figures 52 and 53 show similar results for a low-carbon content (≈0.02%) heat of Alloy 600 in simulated BWR and PWR water at 289 and 320°C, respectively, and the combined results for this heat in both environments. The predicted CGRs are consistent with experimental values over the range of $\approx 3 \times 10^{-11}$ to 3×10^{-8} m·s^{-1}. The distribution of residual values in Fig. 53 for CGRs in both environments indicate that the correlations adequately account for the effect of load ratio and that temperature, heat-treatment condition corresponding to identification codes 4-7 in Table 12, and DO concentration have no effect on the rates (exponent m in Eq. 12 for the dependence of the CGR on DO in Table 18 is zero).

Figures 54 and 55 show the combined results for Alloy 600 with ≈0.06 and 0.02% carbon from the sets of parameters given in Table 19. The predicted CGRs for these heats of material from Eq. 12 and the parameters in Table 19 take into account the effects of loading conditions and DO concentration in water; the rates are not dependent on either temperature or heat-treatment condition as indicated by the distribution of residual values of the ratio of the predicted and experimental CGRs in Fig. 55.

Figures 56 and 57 show the predicted versus experimental CGRs and the residual values, i.e., the logarithm of the ratio of the predicted and experimental CGRs, versus load ratio, temperature, heat and heat-treatment condition, and DO for Alloy 690 in high-purity and simulated PWR water. The variability of the CGR data for Alloy 690 in water is less than that for Alloy 600, and is only slightly greater than that in tests on Alloys 600 and 690 in air. As in

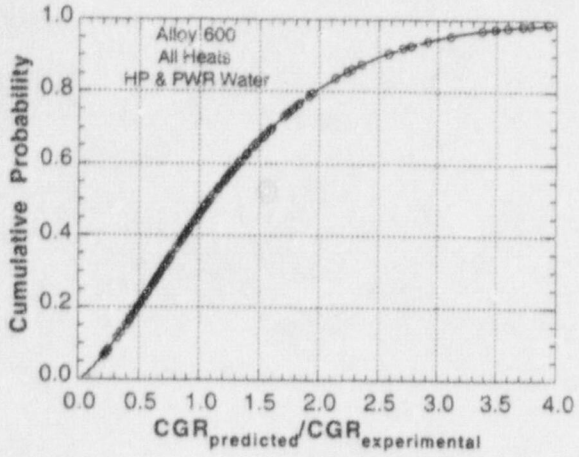

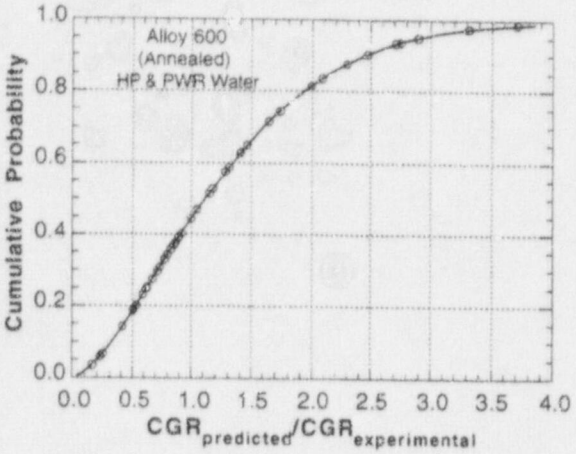

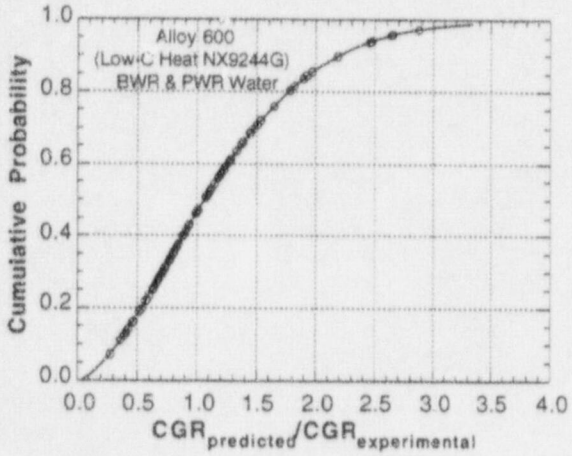

Figure 46.
Cumulative probability of ratio of predicted and experimental CGRs versus this ratio for Alloy 600; combined data for all heats, annealed, and low-carbon content heat in high-purity water and simulated BWR and PWR environments

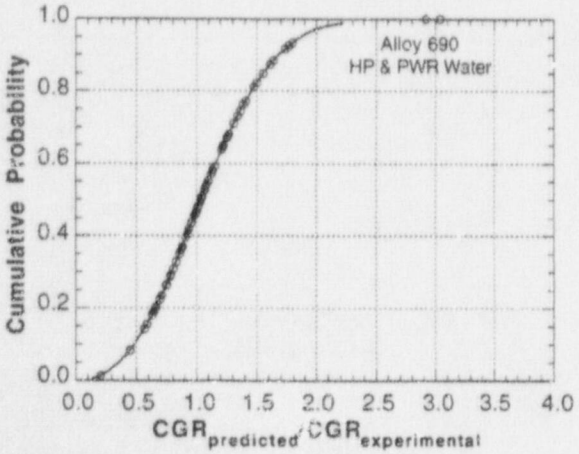

Figure 47.
Cumulative probability of ratio of predicted and experimental CGRs versus this ratio for Alloy 690 in high-purity water and simulated PWR environments

the case for Alloy 600 with ≈0.06% carbon, the CGRs of Alloy 690 depended on DO level and loading parameters (Table 18); temperature and heat and heat-treatment condition (identification codes 8-11 in Table 12) have a minimal effect on the rates as indicated by the distribution of residual values in Fig. 57.

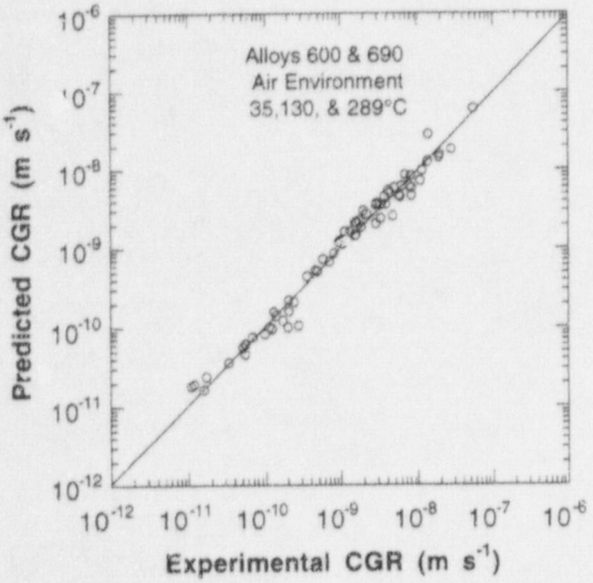

Figure 48.
Predicted versus experimental values of crack growth rate of Alloys 600 and 690 in air

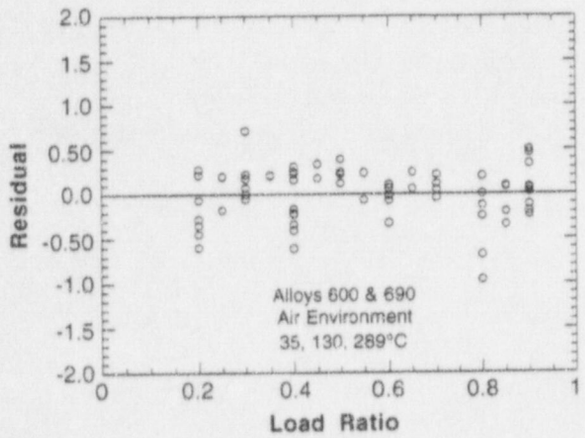

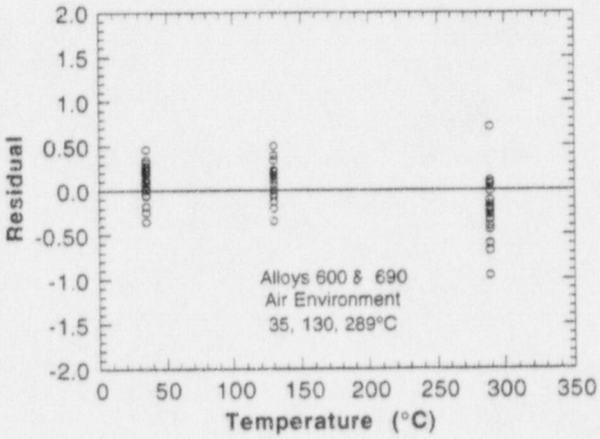

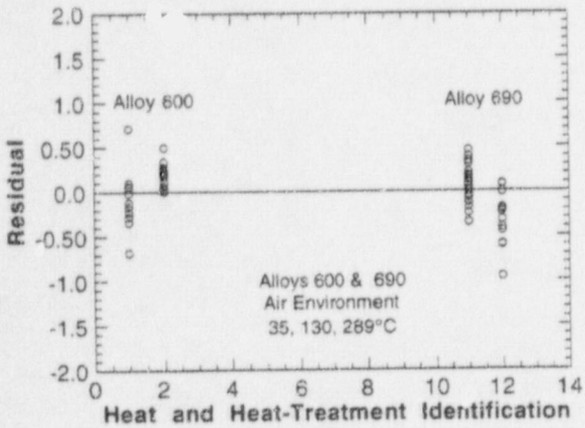

Figure 49.
Residual error for Alloys 600 and 690 in air as function of load ratio, temperature, and heat and heat-treatment condition. Residual is positive when predicted value is greater than experimental value.

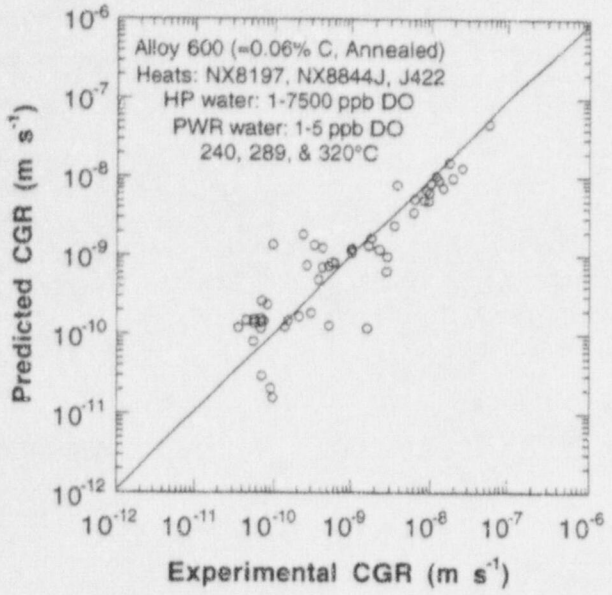

Figure 50.
Predicted versus experimental values of crack growth rate of Alloy 600 in high-purity water and simulated PWR environments

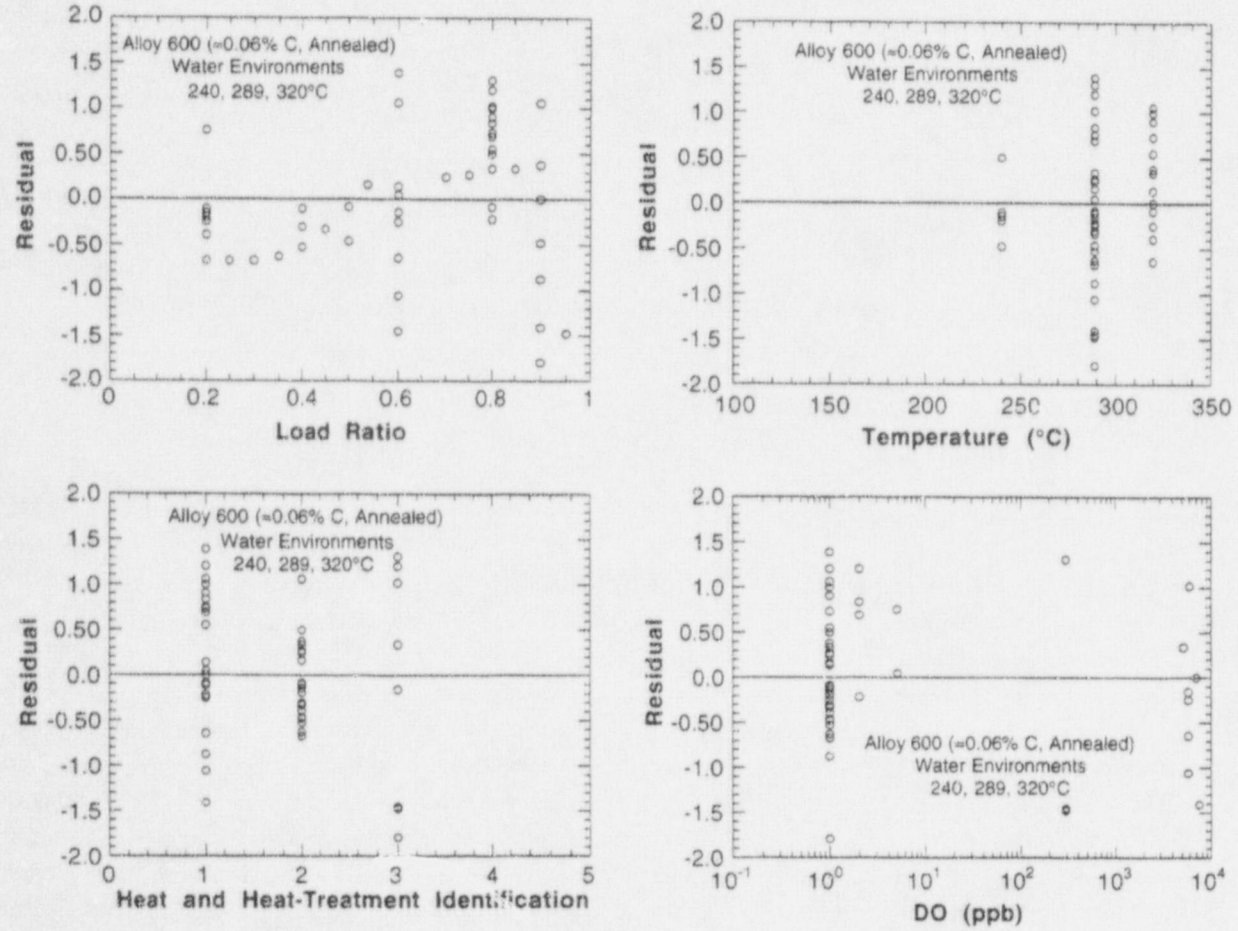

Figure 51. Residual error for annealed Alloy 600 with ≈0.06 % carbon as function of load ratio, temperature, heat and heat-treatment condition, and dissolved oxygen. Residual is positive when predicted value is greater than experimental value.

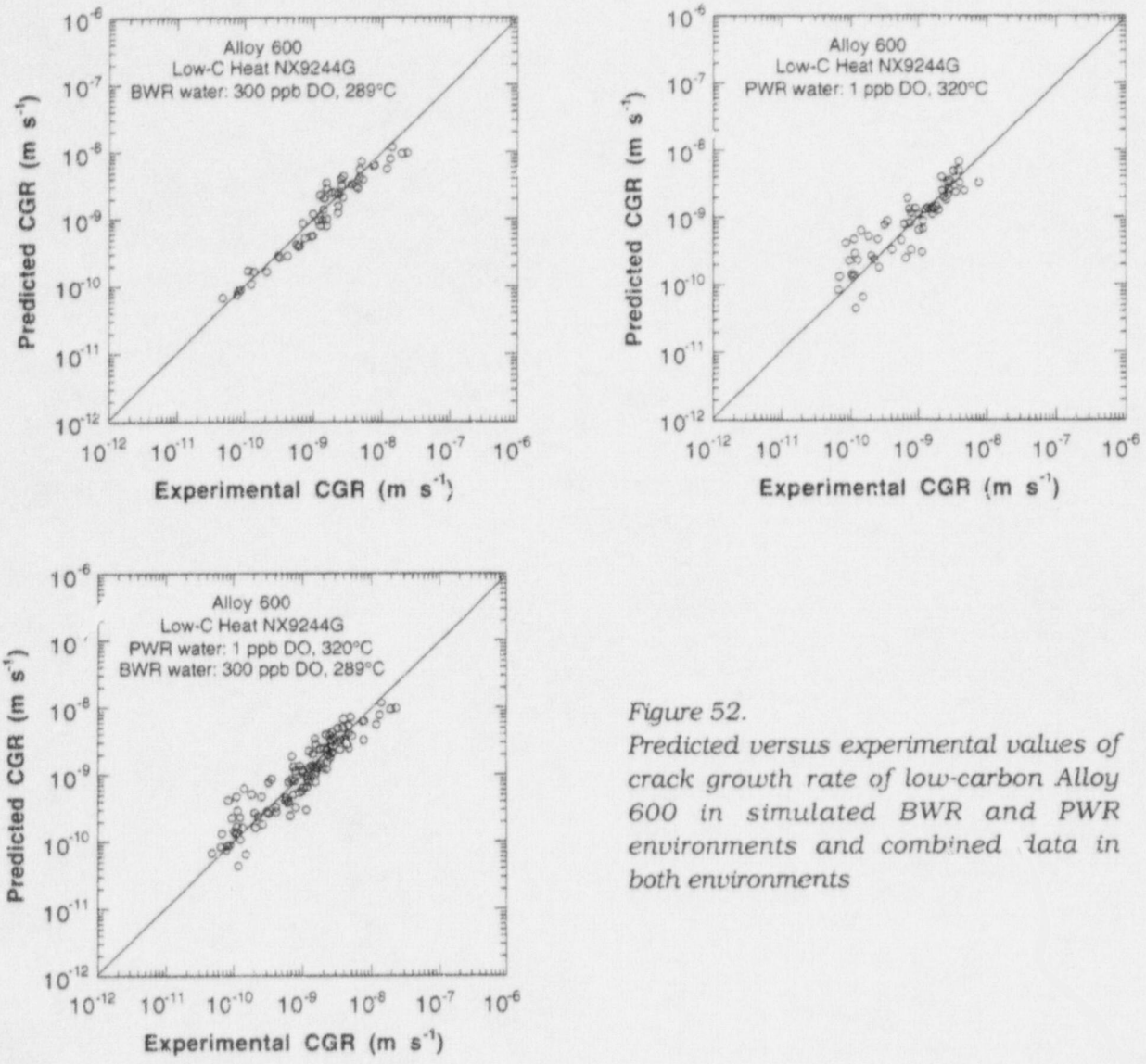

Figure 52.
Predicted versus experimental values of crack growth rate of low-carbon Alloy 600 in simulated BWR and PWR environments and combined data in both environments

Figure 58 shows experimental crack growth data for Alloys 600 and 690 in air, along with calculated curves based on Eq. 13 and the parameters in Table 19 together with Eq. 20 and the Weibull parameters in Table 20 for confidence levels, P, of 5, 50 (best fit), and 95%. The calculated curves correspond to a rise time of 12 s and an average K_{max} of 39 MPa·m$^{1/2}$, both of which were used in these experiments. Experimental crack growth data for Alloy 690 in high-purity and simulated PWR water that contains 1 ppb DO and calculated curves based on Eq. 12 at this DO level, a 12 s rise time, and an average K_{max} of 45 MPa·m$^{1/2}$ are shown in Fig. 59. Figure 60 shows similar results for solution-annealed Alloy 600 with ≈0.06% carbon at an average K_{max} of 36 MPa·m$^{1/2}$. Figure 61 shows similar comparisons of calculated curves and experimental crack growth data for a low-carbon heat of Alloy 600 (NX9244G) in water that contains 1 and 300 ppb DO at 320 and 289°C, respectively. The combined data from all heats of Alloy 600 are shown in Fig. 62 at DO levels of 1 and 300 ppb. In each of these figures, the calculated curves are obtained with a rise time of 12 s, the average K_{max} for the data set, and appropriate constants in Tables 19 and 20.

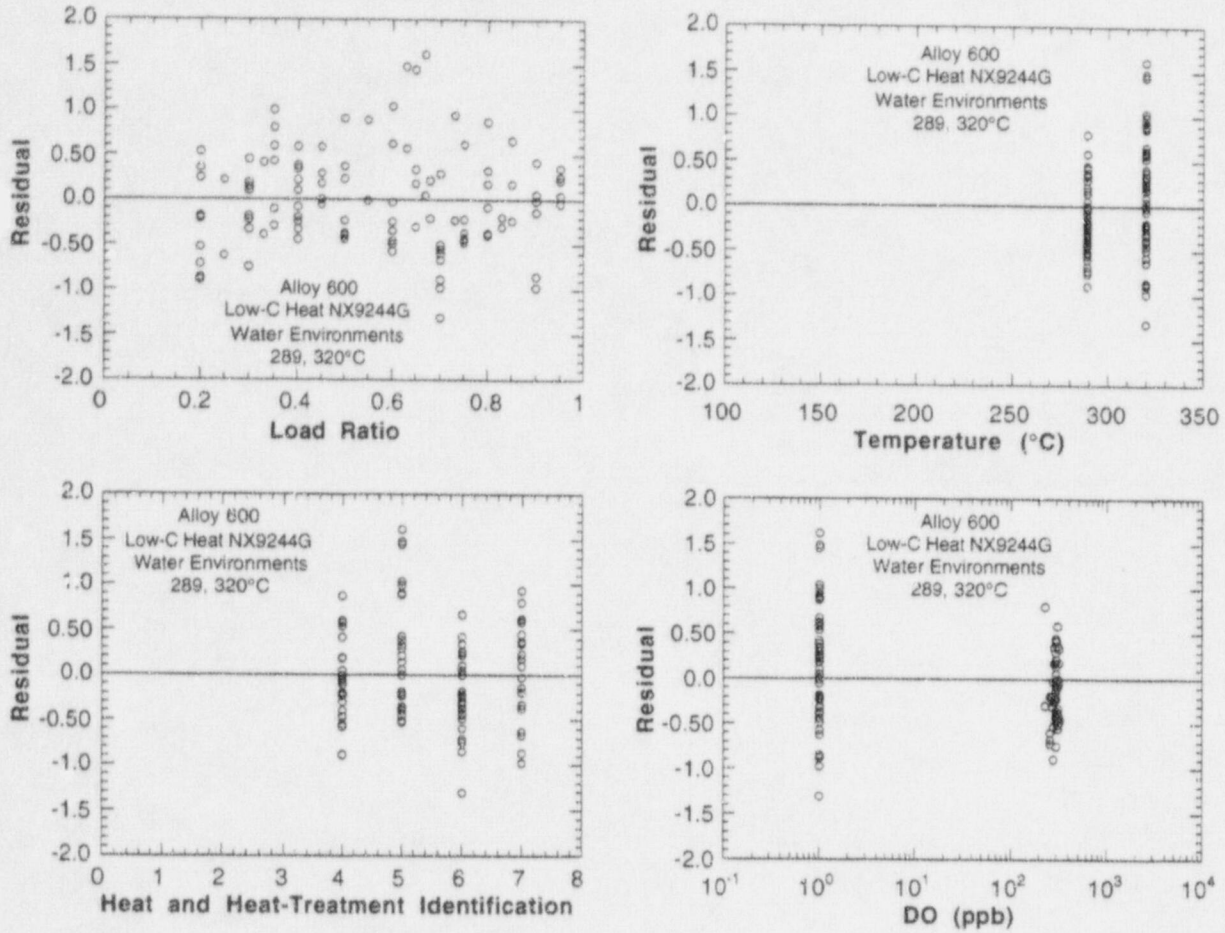

Figure 53. Residual error for low-carbon Alloy 600 as function of load ratio, temperature, heat and heat-treatment condition, and dissolved oxygen. Residual is positive when predicted value is greater than experimental value.

4.4.5 Comparison of Crack Growth Rates of Alloys 600 and 690 in Water and Air

Equation 12 and the constants from best-fit solutions for each data set in Tables 19 and 20 can be used to compare the CGRs of Alloys 600 and 690 in air and water environments under the same loading conditions. Such a comparison must be made at the same rise time, load ratio, and maximum stress intensity because the power-law exponents, p for the load ratio correction factor and n for stress intensity ΔK, where $\Delta K = K_{max}(1 - R)$, differ somewhat for Alloys 600 and 690 and for each data set for Alloy 600. Also, the CGRs in water at load ratios >0.8 exhibit a relatively small but differing dependence on DO through the power-law exponent m. In addition, such comparisons should consider the variability of the CGR data, which is somewhat lower for tests conducted in air (Fig. 45) than in water (Figs. 46 and 47). Figures 63 and 64 show the dependence of CGRs at the 50 and 95% confidence levels of Alloys 600 and 690 in water that contains 1 ppb DO and in air at a K_{max} of 30 MPa·m$^{1/2}$ and a rise time of 12 s, which was used in all of the experiments. Figures 65 and 66 show similar comparisons of the CGRs of Alloy 600 with ≈0.02 and 0.06% carbon, and Alloys 600 (all heats) and 690, respectively, under the same water chemistry and loading conditions. The dependence of the CGR of Alloy 600 on ΔK in air is included in Fig. 66.

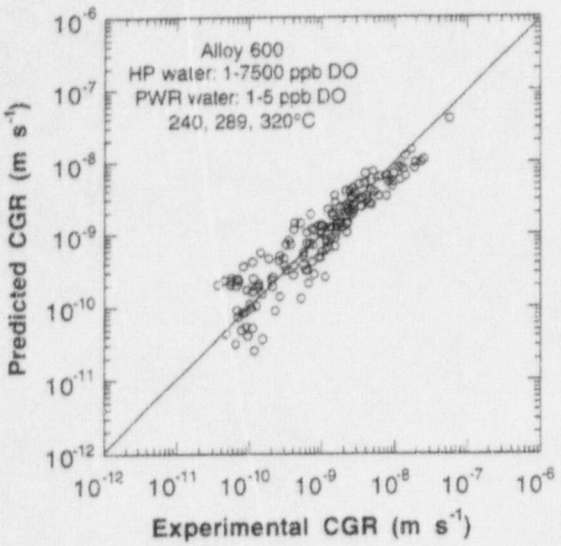

Figure 54.
Predicted versus experimental values of crack growth rate of all heats of Alloy 600 in high-purity water and simulated PWR environments

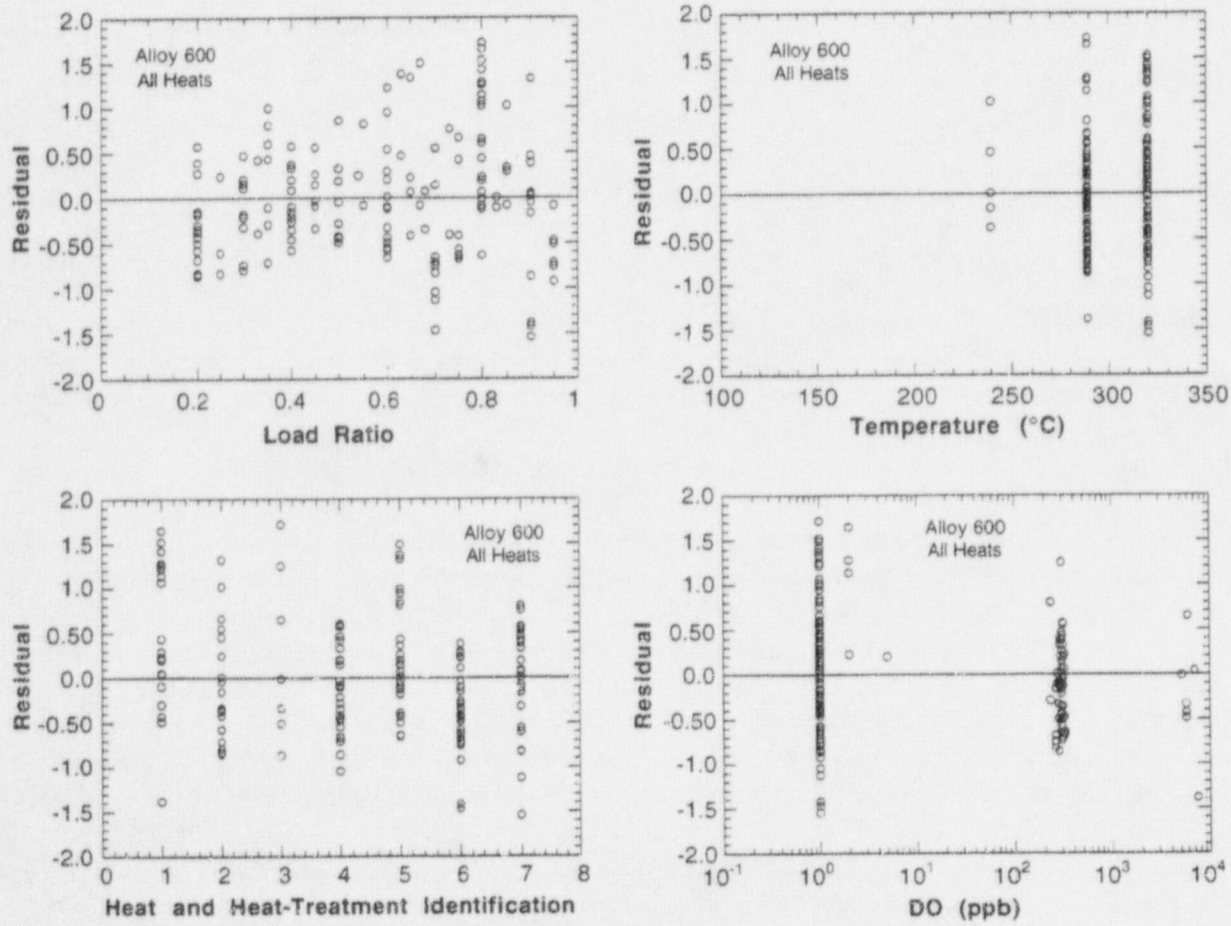

Figure 55. Residual error for CGRs of all heats of Alloy 600 as function of load ratio, temperature, heat and heat-treatment condition, and dissolved oxygen in simulated high-purity water and PWR environments. Residual is positive when predicted value is greater than experimental value.

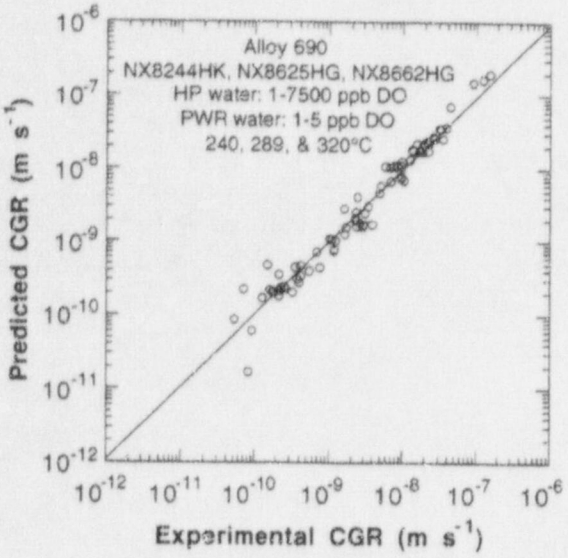

Figure 56.
Predicted versus experimental values of crack growth rate of Alloy 690 in simulated high-purity water and simulated PWR environments

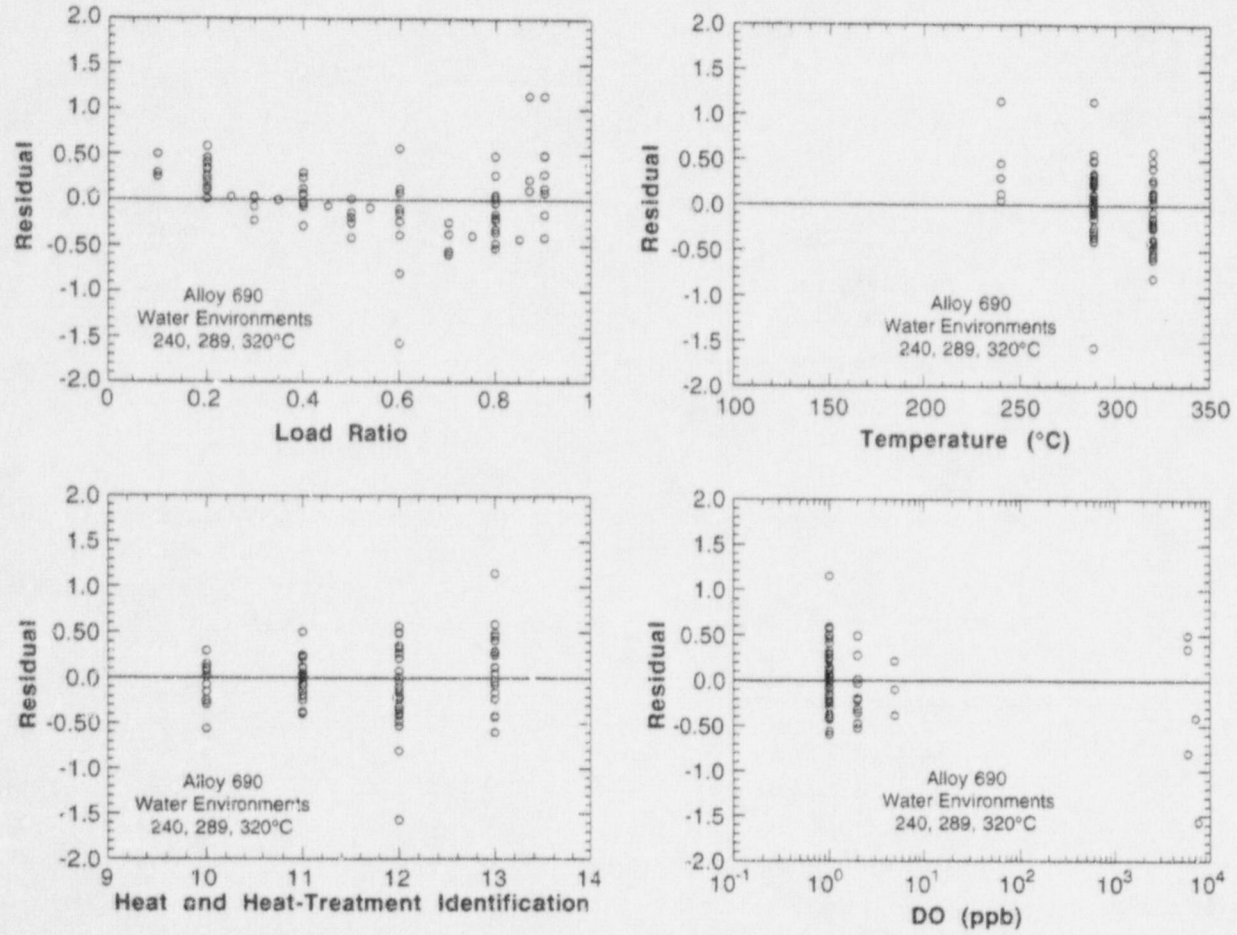

Figure 57. Residual error for Alloy 690 as function of load ratio, temperature, heat and heat-treatment condition, and dissolved oxygen. Residual is positive when predicted value is greater than experimental value.

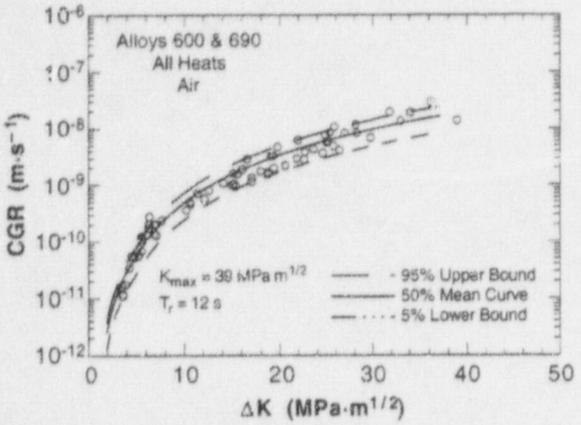

Figure 58.
Experimental crack growth data for Alloys 600 and 690 in air, and calculated CGRs at 5, 50, and 95% confidence levels as function of ΔK

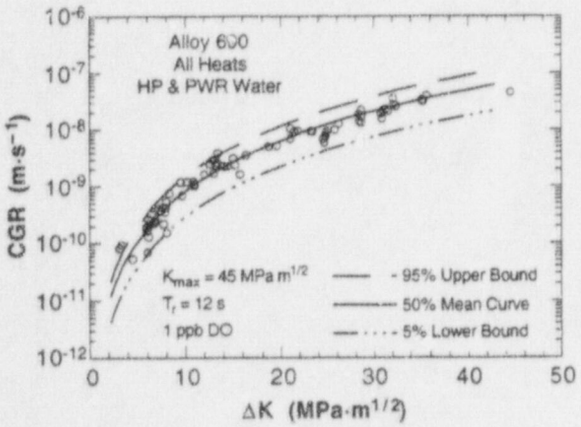

Figure 59.
Experimental crack growth data for Alloy 690 in water that contains 1 ppb DO, and calculated CGRs at 5, 50, and 95% confidence levels as function of ΔK

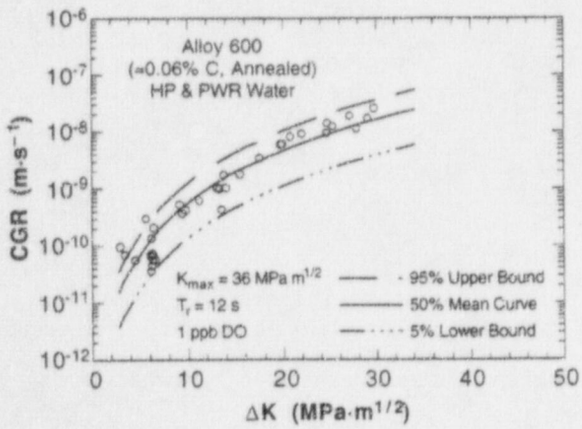

Figure 60.
Experimental crack growth data for Alloy 600 in water that contains 1 ppb DO, and calculated CGRs at 5, 50, and 95% confidence levels as function of ΔK

The predicted CGRs of Alloys 600 and 690 in water (1 ppb DO) are higher by a factor of ≈2 than in air based on best-fit curves (50% confidence level) in Figs. 63 and 64. At the 95% confidence level, the predicted CGRs in water are somewhat higher than those in air because the variability of the CGR data in water is higher than in air. In Fig. 65, the predicted CGRs of low-carbon (≈0.02%) Alloy 600 in water that contains ≈1 ppb DO are higher than for Alloy 600 with a typical carbon content of ≈0.06% for ΔK values of ≤16 MPa·m$^{1/2}$, but the CGRs for these materials are virtually the same at higher values of ΔK. The CGR-versus-ΔK curves

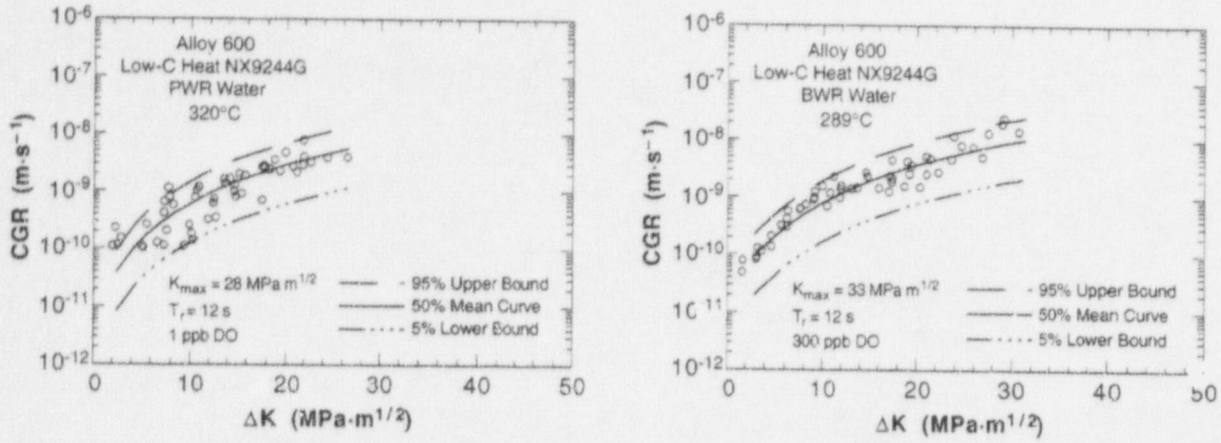

Figure 61. Experimental crack growth data for low-carbon Alloy 600 in simulated PWR and BWR water that contains 1 and 300 ppb DO at 320 and 289°C, respectively, and calculated CGRs at 5, 50, and 95% confidence levels as function of ΔK

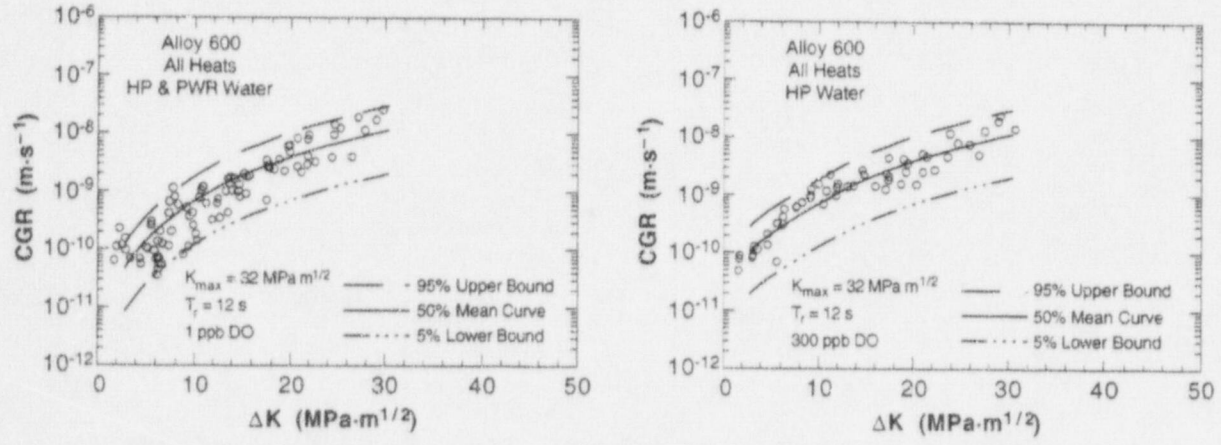

Figure 62. Experimental crack growth data for all heats of Alloy 600 in high-purity water that contains 1 and 300 ppb DO and in simulated PWR environments with 1 ppb DO and calculated CGRs at 5, 50, and 95% confidence levels as function of ΔK

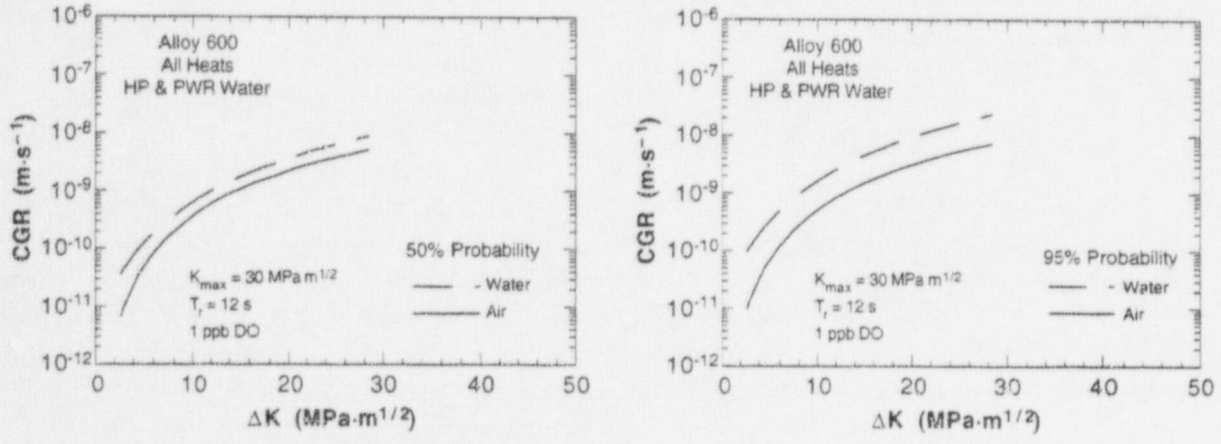

Figure 63. Predicted dependence on ΔK of CGRs of Alloy 600 (all heats) at 50 and 95% confidence levels at K_{max} of 30 MPa·m$^{1/2}$ and rise time of 12 s in high-purity and simulated PWR water that contains 1 ppb DO

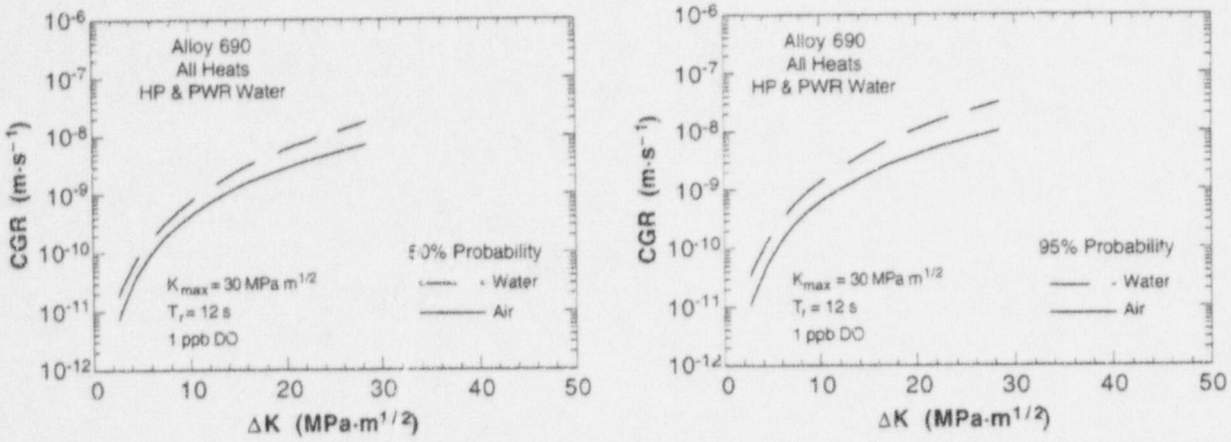

Figure 64. Predicted dependence on ΔK of CGRs of Alloy 690 (all heats) at 50 and 95% confidence levels at K_{max} of 30 MPa·m$^{1/2}$ and rise time of 12 s in high-purity and simulated PWR water that contains 1 ppb DO

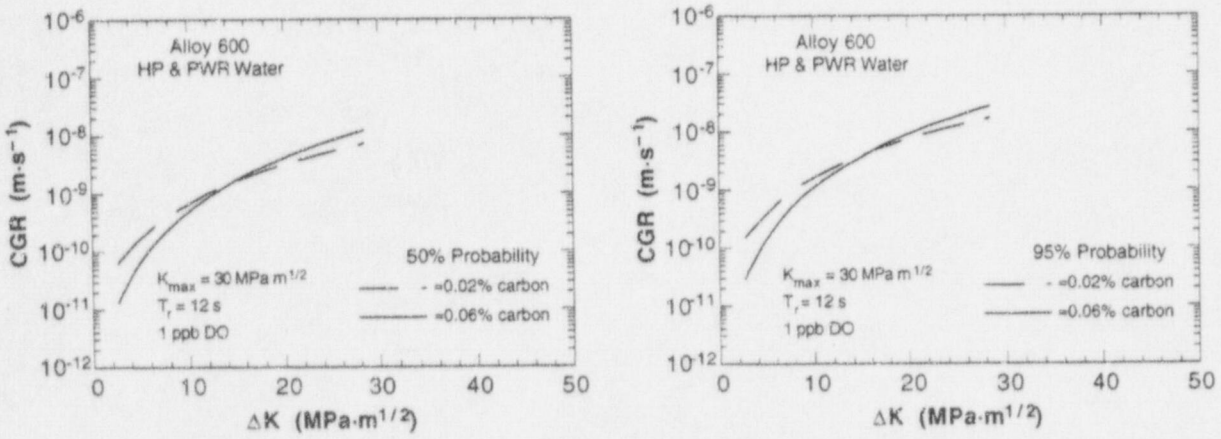

Figure 65. Predicted dependence on ΔK of CGRs of Alloy 600 with ≈0.02 and 0.06% carbon at 50 and 95% confidence levels at K_{max} of 30 MPa·m$^{1/2}$ and rise time of 12 s in high-purity and simulated PWR water that contains 1 ppb DO

for Alloys 690 and 600 in low-DO water in Fig. 66 are higher than the curve for Alloy 600 in air over the entire range of ΔK. At the 50 and 95% confidence levels, the CGRs of Alloy 690 are lower than those of Alloy 600 (all heats) at ΔK values of <≈6 MPa·m$^{1/2}$.

The ratio of CGRs of Alloys 600 and 690 in water and in air from the best fit of the experimental data to Eqs. 12 and 13 can also be used to assess the effect of environment and loading conditions on crack propagation in materials with differing composition and heat treatment. The dependence on ΔK of the ratio of the CGRs of Alloy 600 with ≈0.02 and 0.06% carbon and the combined data for all heats of this alloy in water that contains 1 and 300 ppb DO to that in air is shown in Fig. 67 for a rise time of 12 s and a K_{max} of 30 MPa·m$^{1/2}$. The curves represent the best fit (50% confidence level) to the experimental data. Similar results for Alloy 690 are shown in Fig. 68. These figures also show enhancement of the CGRs in water relative to those in air at ΔK values <6 MPa·m$^{1/2}$. At higher ΔK values, CGRs in water

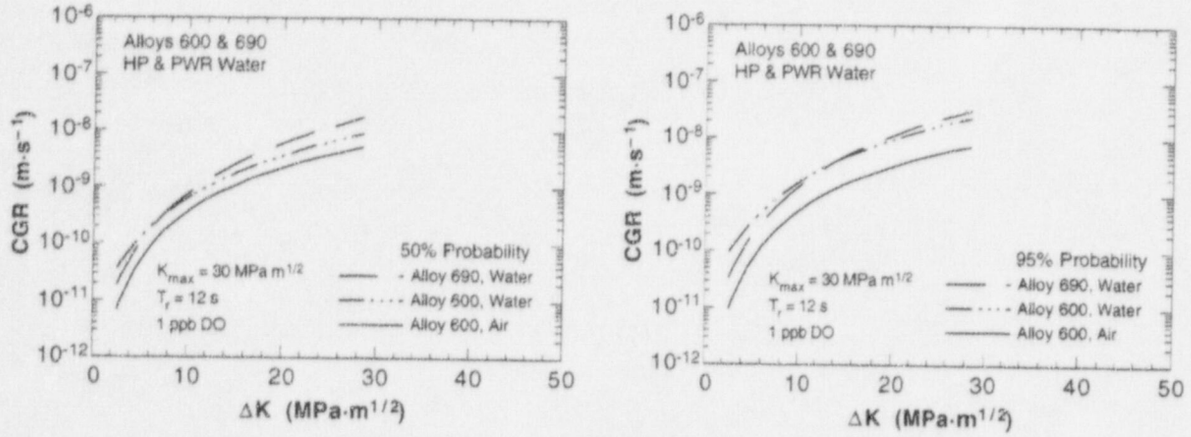

Figure 66. Predicted dependence on ΔK of CGRs of Alloys 600 and 690 (all heats) at 50 and 95% confidence levels at K_{max} of 30 MPa·m$^{1/2}$ and rise time of 12 s in high-purity and simulated PWR water that contains 1 ppb DO

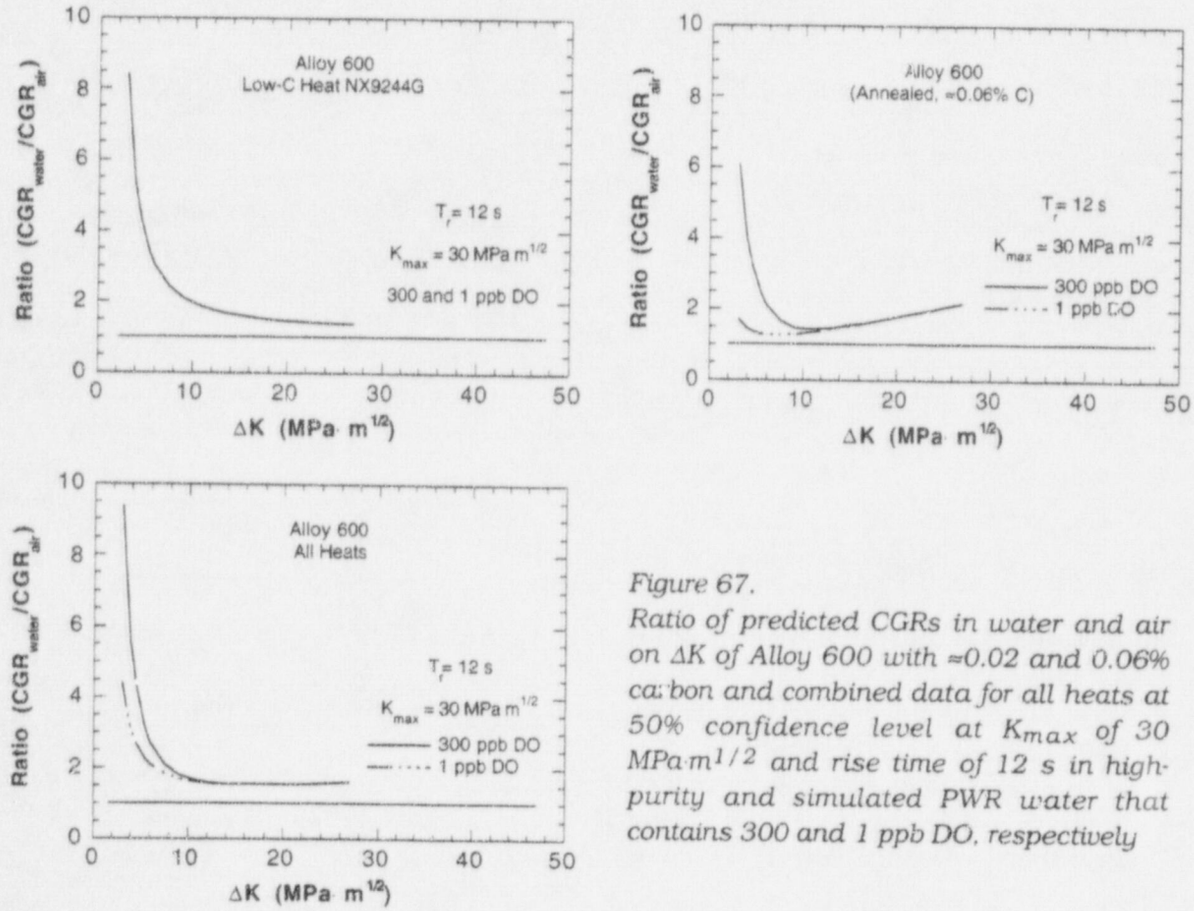

Figure 67.
Ratio of predicted CGRs in water and air on ΔK of Alloy 600 with ≈0.02 and 0.06% carbon and combined data for all heats at 50% confidence level at K_{max} of 30 MPa·m$^{1/2}$ and rise time of 12 s in high-purity and simulated PWR water that contains 300 and 1 ppb DO, respectively

are higher by a factor of ≈2 than in air. The slight minimum in the ratio for annealed Alloy 600 with ≈0.06% carbon is an artifact in the fit of the data to Eqs. 12 and 13, which manifests itself in ratio of the CGRs in water and air. Because there is no effect of DO on the CGRs of the low-carbon heat of Alloy 600, the curves for 1 and 300 ppb superimpose, although the rates in water are higher than in air by a factor of 6-8 at a ΔK of ≈4 MPa·m$^{1/2}$. This variation

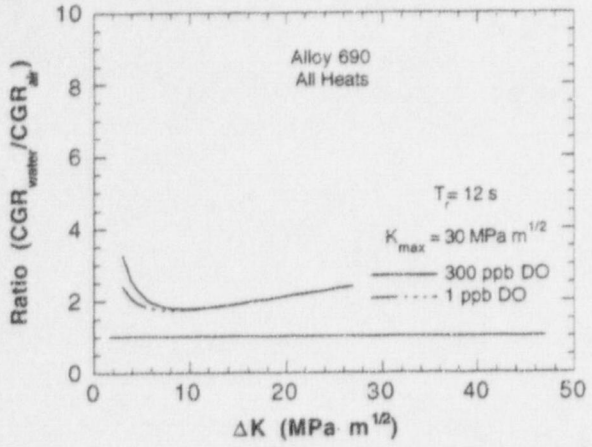

Figure 68.
Ratio of predicted CGRs in water and air on ΔK of Alloy 690 at 50% confidence level at K_{max} of 30 MPa·m$^{1/2}$ and rise time of 12 s in high-purity and simulated PWR water that contains 300 and 1 ppb DO, respectively

occurs because of the different power-dependence p of the load-ratio-correction factor rather than from water chemistry, i.e., the DO level.

Crack growth rates of annealed Alloy 600 with ≈0.06% carbon are also higher in water than in air, but mainly in water with ≈300 ppb DO. The effect of DO on CGRs from the combined data of all heats of Alloy 600 in water is also evident in Fig. 67. At low values of ΔK, the ratios of the CGRs in water relative to those in air are ≈4 and 8 for DO levels of ≈1 and 300 ppb; however, the differing dependence of the CGRs in water and in air on load ratio via the load-ratio-correction factor accounts for a significant portion of the enhancement of the rates in water at low values of ΔK. In contrast, the results in Fig. 68 for Alloy 690 indicate that the rates in water are higher than in air by a factor of ≈2 for both DO levels over the entire range of ΔK. A phenomenological explanation for the dependence on DO, R, and ΔK of the CGRs of Alloys 600 and 690 cannot be obtained from statistical fits of the experimental data to various crack growth relationships that incorporate well-controlled loading and environmental parameters in the experiments. Nevertheless, the correlations provide a means to predict CGRs of these alloys over a wide range of conditions (except for constant load, R = 1) with various levels of confidence.

5 Summary of Results

5.1 Environmental Effects on Fatigue S–N Behavior of Austenitic Stainless Steels

The existing fatigue S–N data for austenitic stainless steels in air and water environments have been evaluated to establish the effects on the fatigue lives of these steels due to various material and loading variables such as steel type, strain range, strain rate, temperature, and DO level in water. In air, the fatigue lives of austenitic SSs are independent of temperature in the range from room temperature to 450°C. At temperatures ≥250°C, fatigue life decreases with decreasing strain rate. Also, the fatigue lives of Types 304 and 316 SS are comparable and those of Type 316NG are superior. For all steels, cyclic stresses increase with decreasing strain rate and are 20–30% lower at 288–430°C than at room temperature. The results indicate that the current ASME mean curve is not consistent with the existing fatigue S–N data.

The results in LWR environments indicate a significant decrease in fatigue life in water relative to that in air; the decrease in life depends on strain rate, DO level in water, and temperature. Environmental effects on fatigue life are comparable for all steels. However, unlike those in carbon and low-alloy steels, environmental effects are more pronounced in low-DO than in high-DO water for austenitic SSs. The influence of reactor environments on fatigue crack initiation is discussed.

Statistical models that were developed previously by Argonne National Laboratory for estimating fatigue S–N curves as a function of material, loading, and environmental variables have been updated with a larger fatigue data base. Design fatigue curves have been developed for austenitic SSs in LWR environments. These curves can be used to perform ASME Code fatigue evaluations for components for service in LWR environments.

The effects of LWR coolant environments on fatigue life have also been expressed in terms of a fatigue life correction factor defined as the ratio of the life in air to that in water. To incorporate environmental effects into the ASME Code fatigue evaluations, a fatigue usage for a specific load pair based on the current Code fatigue design curve is multiplied by the correction factor.

5.2 Irradiation-Assisted Stress Corrosion Cracking

Total elongation measured in simulated BWR water on numerous nonirradiated specimens was in the range of 17-59%, and heat-to-heat variation among the same type of steels was significant. A high-oxygen content in one heat of Type 304 SS produced a significant degradation in the SSRT test properties in water, even in the nonirradiated state. This observation appears to be qualitatively consistent with a trend reported previously that a high oxygen concentration in irradiated steels or core shroud welds is conducive to higher susceptibility to IGSCC.

Slow-strain-rate-tensile tests were conducted on model SS alloys that were irradiated at 288°C in helium in the Halden reactor. Tests in simulated BWR water at 288°C were completed for 16 alloys that were irradiated to a fluence of $\approx 0.3 \times 10^{21}$ n·cm^{-2} (E > 1 MeV) and 4 alloys irradiated to a fluence of $\approx 0.9 \times 10^{21}$ n·cm^{-2} (E > 1 MeV). Fractographic analysis by scanning electron microscopy has been completed to determine susceptibilities to intergranular and transgranular stress corrosion cracking (IGSCC and TGSCC). Heat-to-heat variations in susceptibilities to IGSCC and TGSCC were very significant. High-purity heats of Types 304L and 316L SS exhibited less ductility during the SSRT tests and were more susceptible to IGSCC than commercial-purity heats.

Silicon in Types 304 and 304L SS exerts a profound effect on irradiation-induced hardening and irradiation-induced microstructural evolution in the materials. High concentration of silicon is conducive to less irradiation-induced hardening and lower Frank loop density.

Susceptibilities of the 16 alloys to IASCC at 0.3×10^{21} n·cm^{-2} (E > 1 MeV), measured in terms of combined percent IGSCC and TGSCC, could be correlated best in terms of nitrogen and silicon concentrations. All alloys that contain <50 wppm nitrogen and <1.0 wt.% silicon were susceptible to SCC, whereas all alloys that contain >50 wppm nitrogen or >1.0 wt.% silicon were relatively resistant. This result suggests that to reduce the susceptibility to

IASCC, nitrogen and silicon concentrations of the steel should be >100 wppm and >1.0 wt.%, respectively. Because most commercial heats of Types 304 or 304L SS contain >100 wppm nitrogen, alloys with >1 wt.% silicon could delay onset and increase resistance to IASCC. Although IASCC failure in general is characterized by high susceptibility to TGSCC at low fluence, followed by transition from TGSCC to IGSCC as fluence increases, the above finding requires confirmation by tests on higher-fluence specimens.

Initial SSRT tests were conducted on medium-fluence specimens irradiated to ≈0.9 x 10^{21} n·cm^{-2} (E > 1 MeV). Susceptibility to IGSCC of the alloys that contain <50 wppm nitrogen and <1.0 wt.% silicon was significant at this fluence. When fluence increases from ≈0.3 x 10^{21} to ≈0.9 x 10^{21} n cm^{-2} in the low-nitrogen, low-silicon alloys, susceptibility to TGSCC decreases, and at the same time, susceptibility to IGSCC increases at the expense of TGSCC. This trend is consistent with observations on field-cracked components.

A facility for conducting mechanical tests, e.g., fracture toughness J–R curve, fatigue crack growth, and tensile tests, on irradiated austenitic stainless steel specimens in a hot cell has been designed, fabricated, and assembled. Fracture toughness J–R curve and fatigue crack growth tests are being conducted on 1/4–T CT specimens at room temperature and 288°C on nonirradiated specimens to establish the test procedures. The fracture toughness J–R curve and tensile stress versus strain data for 50% cold worked Type 316NG SS at room temperature and 288°C are presented. This steel shows poor toughness at 288°C.

5.3 Environmentally Assisted Cracking of Low-Carbon Alloys 600 and 690 in Simulated LWR Water

Fracture-mechanics CGR tests were conducted on compact–tension specimens of several heats of Alloys 600 and 690 in annealed, and in annealed and thermally treated, conditions in high-purity water with DO levels between 1 and 7500 ppb and in low-DO water that contained boron acid, lithium hydroxide, and low concentrations of dissolved hydrogen at 240, 289, and 320°C. Fracture-mechanics CGR tests were also conducted on compact–tension specimens of several specimens of these alloys in air at temperatures between 35 and 320°C. A data base of the CGR results has been compiled and CGR correlations were developed that are based on relevant loading and environmental parameters in the experiments. A statistical analysis of the results provides a means of predicting CGRs of the materials under cyclic loading conditions in simulated reactor coolant environments at specified confidence levels.

The degree of enhancement of the CGRs in aqueous environments relative to that in air is a function of both loading and environmental conditions (DO level). Crack growth rates for these alloys in high-purity water and simulated PWR water that contained low levels of DO (<5 ppb) were similar, i.e., the presence of boric acid, lithium hydroxide, and dissolved hydrogen in low-DO water has no discernible effect on the rates based on a best fit of the data to the CGR correlations. Temperature and heat and heat-treatment condition have a relatively minor influence on the rates in air and aqueous environments for the materials under the conditions in our investigation.

Crack growth rates of Alloys 600 and 690 are higher in water than in air at ΔK values < 6 MPa·m$^{1/2}$. At higher ΔK values, the CGRs in water are higher by a factor of ≈2 than in air. Dissolved-oxygen concentration in water (≈1 and 300 ppb) has virtually no effect on the CGRs of the low-carbon heat of Alloy 600, although the rates in water are higher than in air by a

factor of 6-8 at a low ΔK of ≈4 MPa·m$^{1/2}$. This variation occurs because of the different power-dependence of the load-ratio-correction factor rather than from water chemistry. Crack growth rates of annealed Alloy 600 with ≈0.06% carbon are also higher in water than in air, but mainly in water with ≈300 ppb DO. In water that contains ≈1 ppb DO, the predicted CGRs at the 50 and 95% confidence levels for Alloy 600 with ≈0.02% carbon are higher than for material with a normal carbon content of ≈0.06% for ΔK values of <16 MPa·m$^{1/2}$. Crack growth rates for Alloy 690 in water are higher than in air by a factor of only ≈2 for both DO levels over the range of ΔK from ≈4 to 28 MPa·m$^{1/2}$. At the 95% confidence level, the rates for Alloy 690 are only slightly lower than for Alloy 600 in low-DO water at ΔK values of <16 MPa·m$^{1/2}$.

The Alloy 600 and 690 specimens exhibited a predominantly transgranular mode of crack propagation because of the strong contribution of mechanical cyclic loading in tests at a load ratios of <0.8 and the relatively small amount of crack propagation in tests for up to ≈1000 h at higher load ratios.

References

1. K. Iida, *A Review of Fatigue Failures in LWR Plants in Japan*, Nucl. Eng. Des. **138**, 297–312 (1992).

2. D. A. Hale, S. A. Wilson, E. Kiss, and A. J. Gianuzzi, *Low Cycle Fatigue Evaluation of Primary Piping Materials in a BWR Environment*, GEAP-20244, U.S. Nuclear Regulatory Commission (Sept. 1977).

3. S. Ranganath, J. N. Kass, and J. D. Heald, *Fatigue Behavior of Carbon Steel Components in High-Temperature Water Environments*, in BWR Environmental Cracking Margins for Carbon Steel Piping, EPRI NP-2406, Electric Power Research Institute, Palo Alto, CA, Appendix 3 (May 1982).

4. J. B. Terrell, *Effect of Cyclic Frequency on the Fatigue Life of ASME SA-106-B Piping Steel in PWR Environments*, J. Mater. Eng. **10**, 193–203 (1988).

5. N. Nagata, S. Sato, and Y. Katada, *Low-Cycle Fatigue Behavior of Pressure Vessel Steels in High-Temperature Pressurized Water*, ISIJ Intl. **31** (1) 106–114 (1991).

6. M. Higuchi and K. Iida, *Fatigue Strength Correction Factors for Carbon and Low-Alloy Steels in Oxygen-Containing High-Temperature Water*, Nucl. Eng. Des. **129**, 293–306 (1991).

7. M. Higuchi, K. Iida, and Y. Asada, *Effects of Strain Rate Change on Fatigue Life of Carbon Steel in High-Temperature Water*, in Fatigue and Crack Growth: Environmental Effects, Modeling Studies, and Design Considerations, PVP Vol. 306, S. Yukawa, ed., American Society of Mechanical Engineers, New York, pp. 111–116 (1995); also in Proc. Symp. on Effects of the Environment on the Initiation of Crack Growth, ASTM STP 1298, W. A. Van Der Sluys, R. S. Piascik, and R. Zawierucha, eds., American Society for Testing and Materials, Philadelphia, pp. 216–231 (1997).

8. H. Kanasaki, M. Hayashi, K. Iida, and Y. Asada, *Effects of Temperature Change on Fatigue Life of Carbon Steel in High Temperature Water*, in Fatigue and Crack Growth: Environmental Effects, Modeling Studies, and Design Considerations, PVP Vol. 306, S. Yukawa, ed., American Society of Mechanical Engineers, New York, pp. 117–122 (1995).

9. G. Nakao, H. Kanasaki, M. Higuchi, K. Iida, and Y. Asada, *Effects of Temperature and Dissolved Oxygen Content on Fatigue Life of Carbon and Low-Alloy Steels in LWR Water Environment*, in Fatigue and Crack Growth: Environmental Effects, Modeling Studies, and Design Considerations, PVP Vol. 306, S. Yukawa, ed., American Society of Mechanical Engineers, New York, pp. 123–128 (1995).

10. O. K. Chopra and W. J. Shack, *Effects of LWR Environments on Fatigue Life of Carbon and Low-Alloy Steels*, in Fatigue and Crack Growth: Environmental Effects, Modeling Studies, and Design Considerations, PVP Vol. 306, S. Yukawa, ed., American Society of Mechanical Engineers, New York, pp. 95–109 (1995).

11. O. K. Chopra and W. J. Shack, *Effects of Material and Loading Variables on Fatigue Life of Carbon and Low-Alloy Steels in LWR Environments*, in Transactions of 13th Int. Conf. on Structural Mechanics in Reactor Technology (SMiRT 13), Vol. II, M. M. Rocha and J. D. Riera, eds., Escola de Engenharia – Universidade Federal do Rio Grande do Sul, Porto Alegre, Brazil, pp. 551–562 (1995).

12. O. K. Chopra and W. J. Shack, *Evaluation of Effects of LWR Coolant Environments on Fatigue Life of Carbon and Low-Alloy Steels*, in Proc. Symp. on Effects of the Environment on the Initiation of Crack Growth, ASTM STP 1298, W. A. Van Der Sluys, R. S. Piascik, and R. Zawierucha, eds., American Society for Testing and Materials, Philadelphia, pp. 247–266 (1997).

13. O. K. Chopra and W. J. Shack, *Environmental Effects on Fatigue Stress-versus-Strain (S-N) Behavior of Primary Pressure Boundary Materials*, in Environmentally Assisted Cracking in Light Water Reactors, Semiannual Report, January 1997-June 1997, NUREG/CR-4667 Vol. 24, ANL-98/6, pp. 2-32 (April 1998).

14. O. K. Chopra and W. J. Shack, *Effects of LWR Coolant Environments on Fatigue Design Curves of Carbon and Low-Alloy Steels*, NUREG/CR-6583, ANL-97/18.

15. M. Fujiwara, T. Endo, and H. Kanasaki, *Strain Rate Effects on the Low Cycle Fatigue Strength of 304 Stainless Steel in High Temperature Water Environment, Fatigue Life: Analysis and Prediction*, in Proc. Int. Conf. and Exposition on Fatigue, Corrosion Cracking, Fracture Mechanics, and Failure Analysis, ASM, Metals Park, OH, pp. 309–313 (1986).

16. W. J. Shack and W. F. Burke, *Fatigue of Type 316NG SS*, in Environmentally Assisted Cracking in Light Water Reactors, Semiannual Report, October 1989–March 1990, NUREG/CR-4667 Vol. 10, ANL-91/5, pp. 3–19 (March 1991).

17. H. Mimaki, H. Kanasaki, I. Suzuki, M. Koyama, M. Akiyama, T. Okubo, and Y. Mishima, *Material Aging Research Program for PWR Plants*, in Aging Management Through Maintenance Management, PVP Vol. 332, I. T. Kisisel, ed., American Society of Mechanical Engineers, New York, pp. 97–105 (1996).

18. M. Higuchi and K. Iida, *Reduction in Low-Cycle Fatigue Life of Austenitic Stainless Steels in High-Temperature Water*, in Pressure Vessel and Piping Codes and Standards, PVP Vol. 353, D. P. Jones, B. R. Newton, W. J. O'Donnell, R. Vecchio, G. A. Antaki, D. Bhavani, N. G. Cofie, and G. L. Hollinger, eds., American Society of Mechanical Engineers, New York, pp. 79–86 (1997).

19. O. K. Chopra and D. J. Gavenda, *Effects of LWR Coolant Environments on Fatigue Lives of Austenitic Stainless Steels*, in Pressure Vessel and Piping Codes and Standards, PVP Vol. 353, D. P. Jones, B. R. Newton, W. J. O'Donnell, R. Vecchio, G. A. Antaki, D. Bhavani, N. G. Cofie, and G. L. Hollinger, eds., American Society of Mechanical Engineers, New York, pp. 87–97 (1997); also in J. Pressure Vessel Technol. **120**, pp. 116–121 (1998).

20. S. Majumdar, O. K. Chopra, and W. J. Shack, *Interim Fatigue Design Curves for Carbon, Low-Alloy, and Austenitic Stainless Steels in LWR Environments*, NUREG/CR-5999, ANL-93/3 (April 1993).

21. J. Keisler, O. K. Chopra, and W. J. Shack, *Fatigue Strain-Life Behavior of Carbon and Low-Alloy Steels, Austenitic Stainless Steels, and Alloy 600 in LWR Environments*, NUREG/CR-6335, ANL-95/15 (Aug. 1995).

22. J. Keisler, O. K. Chopra, and W. J. Shack, *Statistical Models for Estimating Fatigue Strain-Life Behavior of Pressure Boundary Materials in Light Water Reactor Environments*, Nucl. Eng. Des. **167**, 129-154 (1996).

23. D. D. Macdonald, A. C. Scott, and P. Wentrcek, *External Reference Electrodes for Use in High Temperature Aqueous Systems*, J. Electrochem. Soc. **126**, 908-911 (1979).

24. C. E. Jaske and W. J. O'Donnell, *Fatigue Design Criteria for Pressure Vessel Alloys*, Trans. ASME J. Pressure Vessel Technology **99**, 584-592 (1977).

25. J. B. Conway, R. H. Stentz, and J. T. Berling, *Fatigue, Tensile, and Relaxation Behavior of Stainless Steels*, TID-26135, U.S. Atomic Energy Commission, Washington, DC (1975).

26. D. L. Keller, *Progress on LMFBR Cladding, Structural, and Component Materials Studies During July, 1971 through June, 1972, Final Report, Task 32*, Battelle-Columbus Laboratories, BMI-1928 (1977).

27. Slama, G., Petrequin, P., and Mager, T., 1983, *Effect of Aging on Mechanical Properties of Austenitic Stainless Steel Castings and Welds*, in Assuring Structural Integrity of Steel Reactor Pressure Boundary Components, SMiRT Post Conference Seminar 6, Monterey, CA.

28. O. K. Chopra, *Effect of Thermal Aging on Mechanical Properties of Cast Stainless Steels*, in Proc. of the 2nd Int. Conf. on Heat-Resistant Materials, K. Natesan, P. Ganesan, and G. Lai, eds., ASM International, Materials Park, OH, pp. 479-485 (1995).

29. K. J. Miller, *Damage in Fatigue: A New Outlook*, in Pressure Vessels and Piping Codes and Standard: Volume 1 - Current Applications, PVP Vol. 313-1, K. R. Rao and Y. Asada, eds., American Society of Mechanical Engineers, New York, pp. 191-192 (1995).

30. K. Tokaji, T. Ogawa, and S. Osako, *The Growth of Microstructurally Small Fatigue Cracks in a Ferritic-Pearlitic Steel*, Fatigue Fract. Engng. Mater. Struct. **11**, 331-342 (1988).

31. D. J. Gavenda, P. R. Luebbers, and O. K. Chopra, *Crack Initiation and Crack Growth Behavior of Carbon and Low-Alloy Steels*, in Fatigue and Fracture 1, PVP Vol. 350, S. Rahman, K. K. Yoon, S. Bhandari, R. Wark, and J. M. Bloom, eds., American Society of Mechanical Engineers, New York, pp. 243-255 (1997).

32. F. P. Ford, F. P., *Overview of Collaborative Research into the Mechanisms of Environmentally Controlled Cracking in the Low Alloy Pressure Vessel Steel/Water System*, in Proc. 2nd Int. Atomic Energy Agency Specialists' Meeting on Subcritical Crack Growth, NUREG/CP-0067, MEA-2090, Vol. 2, pp. 3-71 (1986).

33. H. Hänninen, K. Törrönen, W. H. and Cullen, *Comparison of Proposed Cyclic Crack Growth Mechanisms of Low Alloy Steels in LWR Environments*," in Proc. 2nd Int. Atomic Energy Agency Specialists' Meeting on Subcritical Crack Growth, NUREG/CP-0067, MEA-2090, Vol. 2, pp. 73-97 (1986).

34. B. F. Langer, *Design of Pressure Vessels for Low-Cycle Fatigue*, ASME J. of Basic Engineering **84**, 389-402 (1962).

35. American Society of Mechanical Engineers, *Criteria of the ASME Boiler and Pressure Vessel Code for Design by Analysis in Sections III and VIII, Division 2*, ASME, New York (1969).

36. H. S. Mehta and S. R. Gosselin, *An Environmental Factor Approach to Account for Reactor Water Effects in Light Water Reactor Pressure Vessel and Piping Fatigue Evaluations*, EPRI Report TR-105759 (Dec. 1995).

37. H. S. Mehta and S. R. Gosselin, *An Environmental Factor Approach to Account for Reactor Water Effects in Light Water Reactor Pressure Vessel and Piping Fatigue Evaluations*, in Fatigue and Fracture Vol. 1, PVP Vol. 323, H. S. Mehta, ed., American Society of Mechanical Engineers, New York, pp. 171-185 (1996).

38. H. M. Chung, W. E. Ruther, J. E. Sanecki, A. G. Hins, N. J. Zaluzec, and T. F. Kassner, *Irradiation-Assisted Stress Corrosion Cracking of Austenitic Stainless Steels: Recent Progress and New Approaches*, J. Nucl. Mater. **239**, 61-79 (1996).

39. J. M. Cookson, G. S. Was, and P. L. Andresen, *Oxide-Induced Initiation of Stress Corrosion Cracking in Irradiated Stainless Steel*, Corrosion **54**, 299- 312 (1998).

40. H. M. Chung, J. H. Park, W. E. Ruther, J. E. Sanecki, R. V. Strain, and N. J. Zaluzec, *Fabrication-Related Impurity Contamination and Stress Corrosion Cracking of Austenitic Stainless Steel Core-Internal Components*, in Proc. of the 8th Int. Symp. on Environmental Degradation of Materials in Nuclear Power Systems - Water Reactors, ed., S. M. Bruemmer, American Nuclear Society, LaGrange Park, IL, pp. 846-856 (1997).

41. Y. Miwa, T. Tsukada, S. Jitsukawa, S. Kita, S. Hamada, Y. Matsui, and M. Shindo, *Effect of Minor Elements on Irradiation Assisted Stress Corrosion Cracking of Model Austenitic Stainless Steels*, J. Nucl. Mater. **233-237**, 1393-1396 (1996).

42. T. Tsukada, Y. Miwa, and H. Nakajima, *Stress Corrosion Cracking of Neutron-Irradiated Type 304 Stainless Steels*, in Proc. of the 7th Int. Symp. on Environmental Degradation of Materials in Nuclear Power Systems - Water Reactors, eds., G. Airey, et al., American Nuclear Society, LaGrange Park, IL, pp. 1009-1020 (1997).

43. W. F. Michaud, P. T. Toben, W. K. Soppet, and O. K. Chopra, *Tensile-Property Characterization of Thermally Aged Cast Stainless Steels*, NUREG/CR-6142, ANL-93/35 (Feb. 1994).

44. W. E. Ruther, W. K. Soppet, and T. F. Kassner, *Corrosion Fatigue of Alloys 600 and 690 in Simulated LWR Environments*, NUREG/CR-6383, ANL-95/37 (April 1996).

45. W. E. Ruther, W. K. Soppet, D. J. Gavenda, and T. F. Kassner, *Environmentally Assisted Cracking of Alloys 600 and 690 in Simulated LWR Water*, in Environmentally Assisted Cracking in Light Water Reactors, Semiannual Report, October 1994-March 1995, NUREG/CR-4667 Vol. 20, ANL-95/41, pp. 20–30 (Jan. 1996).

46. W. E. Ruther, W. K. Soppet, and T. F. Kassner, *Environmentally Assisted Cracking of Alloys 600 and 690 in Simulated LWR Water*, in Environmentally Assisted Cracking in Light Water Reactors, Semiannual Report, July 1996-December 1996, NUREG/CR-4667 Vol. 23, ANL-97/10, pp. 52–67 (Oct. 1997).

47 W. E. Ruther, W. K. Soppet, and T. F. Kassner, *Environmentally Assisted Cracking of Alloys 600 and 690 in Simulated LWR Water*, in Environmentally Assisted Cracking in Light Water Reactors, Semiannual Report, January 1997-June 1997, NUREG/CR-4667 Vol. 24, ANL-98/6, pp. 65–81 (April 1998).

48. G. L. Webb and M. G. Burke, *Stress Corrosion Cracking Behavior of Alloy 600 in High Temperature Water*, Proc. 7th Int. Symp. on Environmental Degradation of Materials in Nuclear Power Systems – Water Reactors, G. Aiery et al., eds., NACE International, Houston, TX, pp. 41–55 (1995).

49. D. A. Mertz, P. T. Duda, P. N. Pica, and G. L. Spahr, *Role of Microstructure in Caustic Stress Corrosion Cracking of Alloy 690*, Proc. 7th Int. Symp. on Environmental Degradation of Materials in Nuclear Power Systems – Water Reactors, G. Aiery et al., eds., NACE International, Houston, TX, pp. 477–493 (1995).

50. T. M. Angeliu and G. S. Was, *Grain Boundary Chemistry and Precipitation in Controlled Purity Alloy 690*, Proc. 4th Int. Symp. on Environmental Degradation of Materials in Nuclear Power Systems – Water Reactors, D. Cubicciotti, ed., NACE, Houston, TX, pp. 5–64 to 5–77 (1990).

51. J. M. Sarver, J. R. Crum, and W. L. Mankins, *Carbide Precipitation and the Effect of Thermal Treatments on the SCC Behavior of Inconel Alloy 690*, Proc. 3rd Int. on Symp. Environmental Degradation of Materials in Nuclear Power Systems – Water Reactors, G. J. Theus and J. R. Weeks, eds., The Metallurgical Society, Warrendale, PA, pp. 581–586 (1988).

52. A. Saxena and S. J. Hudak, *Review and Extension of Compliance Information for Common Crack Growth Specimens*, Int. J. Fracture **14**, 453-468 (1978).

53. W. E. Ruther, W. K. Soppet, and T. F. Kassner, *Environmentally Assisted Cracking of Alloys 600 and 690 in Simulated LWR Water*, in Environmentally Assisted Cracking in Light Water Reactors, Semiannual Report, April 1995-December 1995, NUREG/CR-4667 Vol. 21, ANL-96/1, pp. 27–43 (July 1996).

54. W. E. Ruther, W. K. Soppet, and T. F. Kassner, *Environmentally Assisted Cracking of Alloys 600 and 690 in Simulated LWR Water*, in Environmentally Assisted Cracking in Light Water Reactors, Semiannual Report, January 1996-June 1996, NUREG/CR-4667 Vol. 22, ANL-97/9, pp. 49–68 (June 1997).

55. P. Paris and F. Erdogan, *A Critical Analysis of Crack Propagation Laws*, Trans. ASME J. Basic Eng., **85**, 528-534 (1963).

56. L. A. James and D. P. Jones, *Fatigue Crack Growth Rates for Austenitic Stainless Steels in Air*, in Predictive Capabilities in Environmentally Assisted Cracking, PVP Vol. 99, The American Society of Mechanical Engineers, pp. 363-414 (1985).

57. W. H. Bamford, P. K. Liaw, and E. D. Eason, *A Review of Corrosion Fatigue Crack Growth Behavior for Pressure Vessel Steels in Light Water Environments*, PVP Vol. 195, MPC Vol. 30, The American Society of Mechanical Engineers, pp. 1-12 (1990).

58. E. K. Walker, *The Effect of Stress Ratio during Crack Propagation and Fatigue for 2024-T3 and 7075-T6*, in The Effects of Environment and Complex Load History on Fatigue Life, STP 462, ASTM, Philadelphia, pp. 1-14 (1970).

59. E. K. Walker, *An Effective Strain Concept for Crack Propagation and Fatigue Life with Specific Applications to Biaxial Stress Fatigue*, Proc. Air Force Conf. on Fatigue and Fracture of Aircraft Structures and Materials, H. A. Wood, et al., eds., pp. 25-233, Report AAFFDL-TR-70-144, Air Force Flight Dynamics Laboratory, Sept. 1970.

60. J. L. Bernard and G. S. Slama, *Fatigue Crack Growth in Air Environment at 300°C for Stainless Steels*, Nucl. Technol., **59**(1), 136-147 (1982).

61. P. Rabbe and H. P. Lieurade, *Etude a l'Aide de la Mecanique de la Rupture de la Vitesse Fissuration en Fatigue d'une Gamme Etendue d'Aciers*, Memoires Scientificiques Revue Metallurgie, **69**(9), 606-621 (1972).

62. R. G. Forman, V. E. Kearney, and R. M. Engle, *Numerical Analysis of Crack Propagation in Cyclic Loaded Structures*, J. Basic Eng., ASME Vol. **89**, Series D, pp. 459-464 (1967).

63. D. W. Hoeppner and W. E. Krupp, *Prediction of Component Life by Application of Fatigue Crack Growth Knowledge*. Eng. Fract. Mech., **6**, 47-70 (1974).

64. M. S. Miller and J. P. Gallagher, *An Analysis of Several Fatigue Crack Growth Rate (FCGR) Descriptions*, in Fatigue Crack Growth Measurement and Data Analysis, STP 738, ASTM, Philadelphia, pp. 205-251 (1981).

65. S. W. Rust and R. C. Rice, *Statistical Distributions*, in Metals Handbook Ninth Ed., Vol. 8, Mechanical Testing, American Society for Metals, Metals Park, OH, pp. 628-638 (1985).

44. W. E. Ruther, W. K. Soppet, and T. F. Kassner, *Corrosion Fatigue of Alloys 600 and 690 in Simulated LWR Environments*, NUREG/CR-6383, ANL-95/37 (April 1996).

45. W. E. Ruther, W. K. Soppet, D. J. Gavenda, and T. F. Kassner, *Environmentally Assisted Cracking of Alloys 600 and 690 in Simulated LWR Water*, in Environmentally Assisted Cracking in Light Water Reactors, Semiannual Report, October 1994-March 1995, NUREG/CR-4667 Vol. 20, ANL-95/41, pp. 20-30 (Jan. 1996).

46. W. E. Ruther, W. K. Soppet, and T. F. Kassner, *Environmentally Assisted Cracking of Alloys 600 and 690 in Simulated LWR Water*, in Environmentally Assisted Cracking in Light Water Reactors, Semiannual Report, July 1996-December 1996, NUREG/CR-4667 Vol. 23, ANL-97/10, pp. 52-67 (Oct. 1997).

47. W. E. Ruther, W. K. Soppet, and T. F. Kassner, *Environmentally Assisted Cracking of Alloys 600 and 690 in Simulated LWR Water*, in Environmentally Assisted Cracking in Light Water Reactors, Semiannual Report, January 1997-June 1997, NUREG/CR-4667 Vol. 24, ANL-98/6, pp. 65-81 (April 1998).

48. G. L. Webb and M. G. Burke, *Stress Corrosion Cracking Behavior of Alloy 600 in High Temperature Water*, Proc. 7th Int. Symp. on Environmental Degradation of Materials in Nuclear Power Systems - Water Reactors, G. Aiery et al., eds., NACE International, Houston, TX, pp. 41-55 (1995).

49. D. A. Mertz, P. T. Duda, P. N. Pica, and G. L. Spahr, *Role of Microstructure in Caustic Stress Corrosion Cracking of Alloy 690*, Proc. 7th Int. Symp. on Environmental Degradation of Materials in Nuclear Power Systems - Water Reactors, G. Aiery et al., eds., NACE International, Houston, TX, pp. 477-493 (1995).

50. T. M. Angeliu and G. S. Was, *Grain Boundary Chemistry and Precipitation in Controlled Purity Alloy 690*, Proc. 4th Int. Symp. on Environmental Degradation of Materials in Nuclear Power Systems - Water Reactors, D. Cubicciotti, ed., NACE, Houston, TX, pp. 5-64 to 5-77 (1990).

51. J. M. Sarver, J. R. Crum, and W. L. Mankins, *Carbide Precipitation and the Effect of Thermal Treatments on the SCC Behavior of Inconel Alloy 690*, Proc. 3rd Int. on Symp. Environmental Degradation of Materials in Nuclear Power Systems - Water Reactors, G. J. Theus and J. R. Weeks, eds., The Metallurgical Society, Warrendale, PA, pp. 581-586 (1988).

52. A. Saxena and S. J. Hudak, *Review and Extension of Compliance Information for Common Crack Growth Specimens*, Int. J. Fracture **14**, 453-468 (1978).

53. W. E. Ruther, W. K. Soppet, and T. F. Kassner, *Environmentally Assisted Cracking of Alloys 600 and 690 in Simulated LWR Water*, in Environmentally Assisted Cracking in Light Water Reactors, Semiannual Report, April 1995-December 1995, NUREG/CR-4667 Vol. 21, ANL-96/1, pp. 27-43 (July 1996).

54. W. E. Ruther, W. K. Soppet, and T. F. Kassner, *Environmentally Assisted Cracking of Alloys 600 and 690 in Simulated LWR Water*, in Environmentally Assisted Cracking in Light Water Reactors, Semiannual Report, January 1996-June 1996, NUREG/CR-4667 Vol. 22, ANL-97/9, pp. 49-68 (June 1997).

55. P. Paris and F. Erdogan, *A Critical Analysis of Crack Propagation Laws*, Trans. ASME J. Basic Eng., **85**, 528-534 (1963).

56. L. A. James and D. P. Jones, *Fatigue Crack Growth Rates for Austenitic Stainless Steels in Air*, in Predictive Capabilities in Environmentally Assisted Cracking, PVP Vol. 99, The American Society of Mechanical Engineers, pp. 363-414 (1985).

57. W. H. Bamford, P. K. Liaw, and E. D. Eason, *A Review of Corrosion Fatigue Crack Growth Behavior for Pressure Vessel Steels in Light Water Environments*, PVP Vol. 195, MPC Vol. 30, The American Society of Mechanical Engineers, pp. 1-12 (1990).

58. E. K. Walker, *The Effect of Stress Ratio during Crack Propagation and Fatigue for 2024-T3 and 7075-T6*, in The Effects of Environment and Complex Load History on Fatigue Life, STP 462, ASTM, Philadelphia, pp. 1-14 (1970).

59. E. K. Walker, *An Effective Strain Concept for Crack Propagation and Fatigue Life with Specific Applications to Biaxial Stress Fatigue*, Proc. Air Force Conf. on Fatigue and Fracture of Aircraft Structures and Materials, H. A. Wood, et al., eds., pp. 25-233, Report AAFFDL-TR-70-144, Air Force Flight Dynamics Laboratory, Sept. 1970.

60. J. L. Bernard and G. S. Slama, *Fatigue Crack Growth in Air Environment at 300°C for Stainless Steels*, Nucl. Technol., **59**(1), 136-147 (1982).

61. P. Rabbe and H. P. Lieurade, *Etude a l'Aide de la Mecanique de la Rupture de la Vitesse Fissuration en Fatigue d'une Gamme Etendue d'Aciers*, Memoires Scientificiques Revue Metallurgie, **69**(9), 606-621 (1972).

62. R. G. Forman, V. E. Kearney, and R. M. Engle, *Numerical Analysis of Crack Propagation in Cyclic Loaded Structures*, J. Basic Eng., ASME Vol. **89**, Series D, pp. 459-464 (1967).

63. D. W. Hoeppner and W. E. Krupp, *Prediction of Component Life by Application of Fatigue Crack Growth Knowledge*, Eng. Fract. Mech., **6**, 47-70 (1974).

64. M. S. Miller and J. P. Gallagher, *An Analysis of Several Fatigue Crack Growth Rate (FCGR) Descriptions*, in Fatigue Crack Growth Measurement and Data Analysis, STP 738, ASTM, Philadelphia, pp. 205-251 (1981).

65. S. W. Rust and R. C. Rice, *Statistical Distributions*, in Metals Handbook Ninth Ed., Vol. 8, Mechanical Testing, American Society for Metals, Metals Park, OH, pp. 628-638 (1985).

NRC FORM 335 (2–89) NRCM 1102, 3201, 3202

U. S. NUCLEAR REGULATORY COMMISSION

BIBLIOGRAPHIC DATA SHEET

(See instructions on the reverse)

1. REPORT NUMBER *(Assigned by NRC. Add Vol., Supp., Rev., and Addendum Numbers, if any.)*
NUREG/CR-4667, Vol. 25
ANL-98/18

2. TITLE AND SUBTITLE
Environmentally Assisted Cracking in Light Water Reactors.
Semiannual Report July 1997—December 1997

3. DATE REPORT PUBLISHED

MONTH	YEAR
September	1998

4. FIN OR GRANT NUMBER
W6610

5. AUTHOR(S)
O. K. Chopra, H. M. Chung, E. E. Gruber, T. F. Kassner,
W. E. Ruther, W. J. Shack, J. L. Smith,
W. K. Soppet, and R. V. Strain

6. TYPE OF REPORT
Technical; Semiannual

7. PERIOD COVERED *(Inclusive Dates)*
July 1997—December 1997

8. PERFORMING ORGANIZATION – NAME AND ADDRESS *(If NRC, provide Division, Office or Region, U.S. Nuclear Regulatory Commission, and mailing address; if contractor, provide name and mailing address.)*

Argonne National Laboratory
9700 South Cass Avenue
Argonne, IL 60439

9. SPONSORING ORGANIZATION – NAME AND ADDRESS *(If NRC, type "Same as above"; if contractor, provide NRC Division, Office or Region, U.S. Nuclear Regulatory Commission, and mailing address.)*

Division of Engineering Technology
Office of Nuclear Regulatory Research
U.S. Nuclear Regulatory Commission
Washington, DC 20555–0001

10. SUPPLEMENTARY NOTES

M. B. McNeil, NRC Project Manager

11. ABSTRACT (200 words or less)

This report summarizes work performed by Argonne National Laboratory on fatigue and environmentally assisted cracking (EAC) in light water reactors from July 1997 to December 1997. Topics that have been investigated include (a) fatigue of austenitic stainless steels (SSs), (b) irradiation-assisted stress corrosion cracking of austenitic SSs, and (c) EAC of Alloys 600 and 690. Fatigue tests were conducted on austenitic SSs in water that contained various concentrations of dissolved oxygen to determine whether a slow strain rate applied during various portions of a tensile-loading cycle is equally effective in decreasing fatigue life. Slow-strain-rate-tensile tests were conducted in simulated boiling water reactor (BWR) water at 288°C on SS specimens irradiated to a low and medium fluence in the Halden reactor, and the results were compared with similar data from a control-blade sheath and neutron-absorber tubes irradiated in BWRs to the same fluence levels. Crack-growth-rate (CGR) tests were completed on compact-tension specimens from several heats of Alloys 600 and 690 in air, high-purity water, and simulated pressurized water reactor environments. CGR correlations were developed as a functon of loading and environmental parameters.

12. KEY WORDS/DESCRIPTORS *(List words or phrases that will assist researchers in locating this report.)*
Corrosion Fatigue
Crack Growth
Irradiation-Assisted Stress Corrosion Cracking
Radiation-Induced Segregation
Stress Corrosion Cracking
Types 304, 304L, 316, and 316NG Stainless Steel
Alloys 600 and 690

13. AVAILABILITY STATEMENT
Unlimited

14. SECURITY CLASSIFICATION
(This Page)
Unclassified
(This Report)
Unclassified

15. NUMBER OF PAGES

16. PRICE

NRC FORM 335 (2–89)

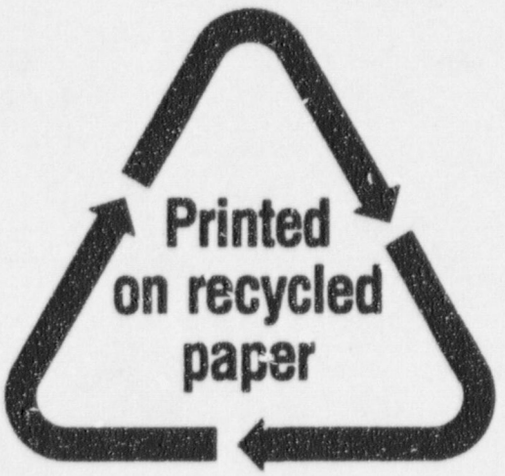

Federal Recycling Program

UNITED STATES
NUCLEAR REGULATORY COMMISSION
WASHINGTON, DC 20555-0001

OFFICIAL BUSINESS
PENALTY FOR PRIVATE USE, $300

SPECIAL STANDARD MAIL
POSTAGE AND FEES PAID
USNRC
PERMIT NO. G-67

120555154486 1 1AN1R5
US NRC-OCIO
DIV-INFORMATION MANAGEMENT
TPS-PDR-NUREG
2WFN-6E7
WASHINGTON DC 20555